Backscattering by Nonspherical Ice Particles at Millimeter Wavelengths: A Theoretical Study

By
Timothy L. Schneider and Graeme L. Stephens

Department of Atmospheric Science
Colorado State University
Fort Collins, Colorado

Research supported by Department of Energy contract #DE-FG03-94ER61748 and National Science Foundation grant # ATM-9100795.
PI: G. Stephens

Colorado State University

Department of Atmospheric Science

Paper No. 546

BACKSCATTERING BY NONSPHERICAL ICE PARTICLES AT MILLIMETER WAVELENGTHS: A THEORETICAL STUDY

Timothy L. Schneider and Graeme L. Stephens

Research supported by the Department of Energy Contract #DE-FG03-94ER61748 and the National Science Foundation Grant #ATM-9100795.

Principal Investigator: Graeme L. Stephens

Department of Atmospheric Science
Colorado State University
Fort Collins, CO 80523

February, 1994

Atmospheric Science Paper No. 546

ABSTRACT

The role of ice clouds in the hydrological cycle is uncertain. As a direct consequence, we do not fully understand the role of ice clouds in the atmospheric energy balance. It is therefore necessary to quantify the existence of ice clouds to understand their role in the upper tropospheric hydrologic cycle. This is primarily achieved with the aid of remote sensors. To extract information from remotely sensed data, it is necessary to understand how electromagnetic radiation interacts with cirrus ice particles. The work presented herein attempted to understand how ice particles of an arbitrary shape backscatter electromagnetic radiation at cloud radar wavelengths.

The discrete dipole approximation (DDA) was applied to the backscattering of millimeter wave radiation by nonspherical ice particles. A simple analytical model of the DDA was developed to demonstrate the underlying physical principles and to understand the directional sensitivity of scattering. Backscattering by single particles was studied to test the use and validity of spheroidal models to model nonspheroidal hydrometeors which are characteristic of cirrus. Limitations of the Rayleigh approximation at millimeter wavelengths were also explored. It was found that for wavelengths on the order of or greater than 3 mm, spheroidal shapes adequately represent hexagonal columns and plates. The Rayleigh approximation for spheroids begins to break down for wavelengths below 8 mm if the particles have major dimensions which are typical of cirrus ice crystals.

The sensitivity of backscattered radiation to variations in microphysical properties were examined, based on DDA calculations for ensembles of ice particles. The most important factor was found to be the median diameter of the third moment (D_m) of the ice crystal size distribution. In particular, if D_m was relatively large, the contribution of small crystals (*i.e.* crystals whose major dimension was on the order of, or less than 100 μm) was masked by the signal of the larger crystals which possessed major dimensions of greater than approximately 400 μm. Simulations of effective radar reflectivity factor-ice water content relations ($Z_e - IWC$) were also presented. Comparison with available empirical relations indicate a functional dependence of the IWC on the number of large crystals (*i.e.* D_m) and also suggest a set of reasonable limits for the parameter D_m. Implications for the remote sensing of ice clouds at millimeter wavelengths were discussed.

ACKNOWLEDGEMENTS

We would like to thank K. F. Evans for supplying the discrete dipole code and much of his insight. Science would cease with out the aid of secretaries; thanks to Sue Lini and Heather Jensen for making life easier. We have benefitted from the many useful discussions we have had with Sergey Matrosov of the Wave Propagation Laboratory, NOAA in Boulder. Ken Lini has graciously provided to us the use of his work stations to do many of the calculations. This work was supported by the Department of Energy Contract #DE-FG03-94ER61748 and the National Science Foundation Grant #ATM-9100795.

CONTENTS

LIST OF FIGURES

LIST OF TABLES

Chapter 1

INTRODUCTION

In a recent paper, Dyson (1993) observes that scientific revolutions are not only driven by new concepts but are in fact more frequently driven by new tools. As examples of tool driven revolutions he cites the invention of Green's functions in 1828 and the much later advent of electronic computers. The role of Green's functions in atmospheric science has undoubtedly been more sublime than the revolutionary role played by computers. Nevertheless the Green's function is at the core of this research in that it allows us to tackle a problem which has long avoided solution; scattering by irregular particles. The exact role of the Greens function will be elucidated in Chapter 2. Although Dyson's paper focuses on George Green's legacy in physics (the class of functions which bare the name of this independent thinker), his observation regarding tool driven revolutions in science is particularly relevant to atmospheric science and the study of this report.

1.1 MOTIVATION

Humanity has long sought to modify the weather to its advantage. There is now a growing realization that we may have indeed succeeded in changing the weather, although it may not be to our advantage or under our control. Humankind has always maintained a keen interest in the weather; only modern convenience permitted by the industrial and technological revolutions has allowed us the luxury of contemplating the climate. And now fears of anthropogenically-induced climate change have induced a societal awareness of climate providing an impetus to improve our understanding of atmospheric processes. Subsequently, since the middle of this century humanity's understanding of the climate system has advanced considerably.

Furthermore these advances in our understanding of the atmosphere are intimately linked to advances in technology. Remote sensors have given us the ability to probe the atmosphere from above and below. With the early satellites we obtained the first global perspective of our weather. This tool has the potential to measure all of the important atmospheric parameters, globally. We have already begun to realize some of these aspirations; measurements of the Earth's radiation budget, the tracking of weather systems, and cloud climatologies are some outstanding examples. Ground based sensors such as radars, lidars, and radiometers permit us to observe the atmosphere on a regional scale and at a higher resolution.

Computers allow us to store and process the enormous quantities of data which have been collected by our instruments. With the aid of computers, we are able to explore the sensitivity of the Earth's climate and weather systems to various components. And finally, computers have allowed us to predict and model the weather with a speed and efficiency which have far surpassed the dreams of L. F. Richardson (1922) when he mused about having 64,000 *human* computers in a room, coordinated by colored lights.

These tools have given us an unprecedented ability to see and understand the climatic system of the Earth. From our perspective thus gained, we have been reminded of the fundamental importance of the hydrologic cycle to the Earth's climate. The hydrology of the atmosphere is intimately intertwined with the radiation and heat budgets of the Earth (e.g. see Stephens and Greenwald, 1991). These components interact through a variety of complex feedback mechanisms involving clouds, precipitation, water vapor, and transport. Manabe and Wetherald (1967) have demonstrated the sensitivity of the radiative convective equilibrium to the vertical profile of water vapor. We are only just beginning to understand the atmospheric hydrologic cycle, but one particular element of the cycle is conspicuous for our lack of understanding of it; namely the hydrology of the upper troposphere (Lindzen, 1990a; Lindzen, 1990b; Sun and Lindzen, 1993). In the upper troposphere ice clouds predominate (i.e. cirrus) and the mechanisms by which the ice clouds hydrate/dehydrate this region are not clearly understood (Danielsen, 1993). In a review of cirrus (Liou, 1986), it was noted that cirrus clouds are ubiquitous, important to the energetics of the atmosphere, and poorly understood. As a first step in clarifying the role of ice clouds in the hydrology of the upper troposphere and in understanding their effect on the water vapor profile, we must be able to measure their properties. Due to their relative inaccessibility we must attempt to quantify them remotely.

To this end a relatively new class of high frequency radars are being exploited. They are often referred to as cloud radars and they operate at millimeter wavelengths. Although the higher frequencies are subject to greater attenuation, cloud radars characteristically possess intrinsic qualities such as higher spatial resolution and greater sensitivity to small scale cloud processes. The attenuation in and of itself may be exploited as a source of information.

Whereas there is presently not a preponderance of cloud radars, the list is beginning to grow. The National Oceanic and Atmospheric Administration (NOAA), Wave Propagation Laboratory (WPL) operates a fully polarized 35-GHz radar (Kropfli et al., 1990). The Microwave Remote Sensing Laboratory (MRSL) at the University of Massachusetts (Pazmany et al., 1993) has developed an airborne, polarized, 95-GHz radar and is presently developing a dual wavelength, fully polarized radar which will operate at 35 and 95 GHz (McIntosh et al., 1991). The MRSL (Mead et al., 1989) also has an operational 215 GHz radar. Lhermitte (1987); Lhermitte (1988) has developed a 94 GHz radar for use in cloud studies. A group at Pennsylvania State University has developed

Group	Wavelength		Comments
NOAA-WPL	8.7 mm	(35 GHz)	Elliptical and linear polarization, Doppler, 100 kW peak power.
RABELAIS (France)	8.6 mm	(35 GHz)	Linear and circular polarization, Doppler, 70 kW peak power.
UMass MRSL	3.2 mm	(95 GHz)	Linear polarization, Doppler, airborne, 1.2 kW peak power.
Lhermitte	3.2 mm	(94 GHz)	Doppler, 1 kW peak power.
Penn. State U.	3.2 mm	(94 GHz)	Doppler, 1.4 kW peak power.
UMass, MRSL	1.4 mm	(215 GHz)	Incoherent, 60 W peak power

Table 1.1: Operational cloud radars.

a 94 GHz radar (Peters et al., 1992). There is another 34.8 GHz radar at Laboratoire d'Aerologie (RABELAIS) in France (see Table 3.1 in Bringi and Hendry, 1990). Some of the characteristics of these radars are summarized in Table 1.1. Furthermore, technological advances have made it possible to include high frequency radars on satellites. A precipitation radar (13.8-GHz) is a part of the TRMM-I package (Meneghini and Kozu, 1990) and a millimeter-wave radar is being considered for inclusion on the TRMM-II package (personal communication; Graeme Stephens, 1993).

The hydrometeors which comprise the upper tropospheric clouds are primarily ice crystals of a highly nonspherical nature. In order to interpret and understand the radar signals returned by these clouds, it is essential to understand the backscattering properties of ice-phase hydrometeors. The work contained in this report has grown out of this need to understand how ice particles of complex nonspherical shapes backscatter polarized microwave energy.

1.2 METHOD

Historically, nonspherical hydrometeors have been theoretically modeled at radar frequencies in one of two ways: either as equal volume spheres or as equal volume spheroids. In the former case one may employ the Lorenz-Mie formulation of scattering by spheres. However, for many meteorological radars it is reasonable to assume that the hydrometeors (excluding large hail) are optically small. Then one may employ what has come to be known as Rayleigh theory, in which a simple analytical expression can be obtained for both spheres and spheroids (i.e. prolate and oblate spheroids). Several other numerical methods have been developed to solve spheroidal scattering problems. For a brief survey of these methods and their applications see Section 2.1.

We know that hydrometeors in cirrus clouds consist of highly aspherical ice particles which posses major dimensions (a) typically ranging in size from approximately 50 microns to 2000 microns. It has been demonstrated that for cirrus ice particles of order $a \simeq 1000\mu m$, scattering in the K_a band (about 35 GHz) is within the Rayleigh regime

(Yeh et al., 1982). As one progresses beyond this to higher frequencies however, the assumption of optically small particles becomes suspect. Therefore, we must conclude that to some degree the "standard" models are inadequate to study the scattering of millimeter-wavelength radiation by cirrus ice particles due to both size and shape considerations. Spheres grossly misrepresent the true shape of cirrus ice particles and although oblate and prolate spheroids do a *better* job at representing the true shape of cirrus ice particles, the fundamental assumption of optically small particles becomes suspect for frequencies greater than approximately 35 GHz.

The issues of shape and optical size were examined through the use of a relatively new numerical modeling technique known as the discrete dipole approximation (DDA). The DDA can model particles of arbitrary shape and size although in practice computer memory and CPU time limits the optical sizes which can be modeled. Because the wavelengths and particle sizes of interest here are ideally suited to the application of the DDA, many of these outstanding issues can be explored. A comparison of DDA-spheroids and Rayleigh-spheroids at 35 and 96 GHz over many particle sizes indicates the range of validity of the Rayleigh approximation. Using the DDA, comparisons between various geometrical models were also performed; spheroidal models were verified against models of shapes which have been observed in cirrus which, for the purposes of this report, were referred to as true or observed shapes (equivalently). The calculations were performed with both the DDA (observed and spheroidal shapes) and a Rayleigh model (spheroidal shapes only) at 13.8, 35, 94 and 220 GHz and for several radar elevation angles. In each case the full Mueller matrix was computed from which various polarimetric radar parameters were derived. The ice particles were assumed to fall with their major dimension in the horizontal plane and to be randomly oriented in this plane.

Simulations of backscattering by various ensembles of ice particles were also performed to represent cirrus clouds. The DDA was used to compute the backscattering of observed ice particle shapes over observationally determined size distributions and polarimetric radar parameters were computed at 35 and 94 GHz for a distribution of sizes. Sensitivities to both bulk and microphysical parameters were examined.

1.3 OUTLINE AND OBJECTIVES

In Chapter 2 the details of the DDA scattering model used in this research are discussed. The physical principles upon which it is based are outlined and some details of the implementation is given. To place these models in context, a review of scattering models which have been used to study scattering by nonspherical hydrometeors at radar frequencies is provided. Calculations are presented to demonstrate the requirements of azimuthal averaging to approximate particles which are randomly oriented with their major dimensions in the horizontal plane. In Chapter 3, issues of shape and size are examined in

the context of Rayleigh scattering. The principles of the Rayleigh model are outlined in the first section of this chapter, followed by a discussion of the optical size limitations of the Rayleigh approximation. Geometrical considerations render the notion of optical size ambiguous for nonspherical particles. Alternative definitions of optical size for nonspherical particles are compared to ascertain which one is most representative of the optical properties of these particles. The ability of spheroidal particles to represent the observed (true) cirrus ice particles is also examined in detail.

In Chapter 4 the focus shifts to simulations of cirrus clouds. The microphysical properties of cirrus clouds are reviewed to form the basis for subsequent calculations. Calculations of the effective radar reflectivity factor for ensembles of ice crystals are presented. Sensitivities to bulk properties of cirrus clouds such as ice water content and number distributions are examined. We also explore the effects of particle shape on the reflectivity. The results are used to understand the dependencies of radar parameters to the aforementioned issues. A tentative retrieval of an important parameter in the ice crystal size distribution is proposed.

In Chapter 5 the prerequisite summary and examination of inherent deficiencies are supplied. Accordingly, future directions of research are suggested to build upon this work. Appendix A defines the relation between the Mueller scattering matrix (which is the output of the scattering models) and radar observables. Emphasis is placed on the physical interpretation of radar polarization parameters.

Chapter 2

SCATTERING MODELS FOR IRREGULAR PARTICLES

In this chapter an overview of models used to study scattering by nonspherical particles is provided. There are numerous models available, all of which vary in their sophistication and range of applicability. At the frequencies of interest, the models employed to study scattering have historically fallen into two categories; spheres and spheroids. Although it is generally accepted that spheres are poor geometrical representatives of nonspherical particles in the context of scattering, scattering by spheres continues to be widely relied upon by many researchers, especially as a first order approximation. Beyond spheres, the high degree of symmetry afforded by ellipsoids has provided for a veritable potpourri of methods. Some of these methods will be reviewed in Section 2.1. Since real ice particles are not generally spheroidal in nature but rather possess corners and flat faces, one must ask the question how well do spheroids represent real ice particles with respect to scattering. Of these methods, perhaps one of the most widely applied models for scattering by ice particles at the frequencies of interest is the Rayleigh approximation for ellipsoids (e.g.Atlas et al., 1953; Seliga and Bringi, 1976; Matrosov, 1991a; Matrosov, 1991b). As technology and interest drives the frequencies of meteorological research radars to higher values, it is probable that the Rayleigh assumption of optically small particles will be violated by some ice particles found in atmospheric conditions.

The discrete dipole model can be used to test these hypotheses because it can be applied to particles of arbitrary shape and size. The work in this report will utilize the Rayleigh approximation for ellipsoids and the DDA. The Rayleigh model for ellipsoids will be discussed in Section 3.1. The underlying physical principles of the DDA as well as some specifics of the implementation employed will be provided in Section 2.2. A simple model of two dipoles is exploited in this section to provide insight into the discrete dipole method as well as to assess the directional sensitivity of scattering. An assumption made throughout this work is that the ice particles are randomly oriented in a plane normal to the local vertical. To simulate this randomness, the particles are averaged azimuthally. Results which indicate the appropriate number of angles to average azimuthally to achieve a sense of randomness are presented in Section 2.3.

2.1 A POTPOURRI OF MODELS

An overview of the various models available for studying scattering by non spherical particles is now given. Emphasis is placed on methods which have been used to study nonspherical meteorological targets at radar wavelengths. Furthermore, the focus is primarily on monostatic applications as opposed to bistatic applications: *i.e.* backscattering. This is done to limit the scope as a comprehensive review of scattering would be truly voluminous. The review is intended to provide a starting point such that the interested reader may find her/his way into the literature, to provide the reader with a notion of what scattering models are available, and to place the models employed in this research in context. The intention is to achieve breadth as opposed to depth and no effort is made to give each method equitable treatment.

As with any discussion of scattering methods one must be careful with the terminology. Consequently, reference will be given to the original work wherever possible. A concise description of each method has been provided accompanied by a discussion of some of the meteorological problems to which it has been applied. The results of this survey are summarized in Table 2.1.

Holt (1982) notes that until the early 1970's, the only models available for computing scattering amplitudes were Rayleigh and Lorenz-Mie for spheres and for nonspheres Rayleigh or Rayleigh-Gans. Since then, however, there has been a profusion of methods available. In 1982 the state of the art according to Holt included the point matching technique, the T-matrix method, the unimoment method, and the Fredholm integral equation method. The the list has since grown. An up to date accounting of methods available to compute scattering by nonspherical particles adds the discrete dipole approximation (DDA) and the finite difference-time domain (FDTD) method.

2.1.1 Approximations For Small Sizes

There are two models available for particles which fall into the category of being optically small; Rayleigh and Rayleigh-Gans. In both cases solutions can be readily obtained for oblate and prolate spheroids. Because both Rayleigh and Gans made considerable contributions to scattering by small particles a large amount of confusion exists in the nomenclature. Van de Hulst (1981) however, seems to provide the cleanest delineation of terminology and his conventions are adopted throughout.

Rayleigh

The details and limitations of this method are given in Section 3.1. Two recent studies exemplify the application of the Rayleigh approximation and have particular relevance: Matrosov (1991a) and Matrosov (1991b). A theoretical study of the radar polarization parameters of cirrus is the subject of Matrosov (1991b). Plates, needles and columns

Small Size Approximations

Paper	Technique	Application
Atlas et al. (1953)	Gans	Water and ice, oblate and prolate spheroids; $\lambda = 1, 3, 10$ *cm.*
Seliga and Bringi (1976)	Gans	Used oblate spheroids to study droplet scattering; X, S bands.
Matrosov (1991b)	Rayleigh	Used prolate and oblate spheroids to study effect of cirrus particles on elliptic polarization; 35 GHz.
Matrosov (1991a)	Rayleigh	Used prolate and oblate spheroids to study scattering by cirrus; 35 GHz.
Matrosov (1992)	Rayleigh-Gans	Used ice spheres to model scattering by snow; X, K_a bands.

Integral Methods

Paper	Technique	Application
Barber and Yeh (1975)	T-matrix	Various dielectric properties, spheres spheroids, and modified cylinders; various optical sizes.
Seliga and Bringi (1978)	T-matrix	Oblate rain and hail particles; 10 *cm.*
Shepard et al. (1981)	FIM	Small spheroidal ice particles; 20 GHz
Yeh et al. (1982)	T-matrix	Oblate and prolate spheroids are used to study ice crystals; 30 GHz.
Vivekanandan et al. (1991)	T-matrix	Used prolate and oblate spheroids to study scattering by hail at various orientations; primarily at 8 *mm.*

Discrete Methods

Paper	Technique	Application
O'Brien and Goedecke (1988)	DDA	Comparison of ice phase hexagonal columns and stellates with cylinders, spheroids and disks; 1 *cm.*
Evans and Vivekanandan (1990)	DDA	Hexagonal plates and cylinders are used to simulate ice particles. Radar; S, C, X, and K_a bands. Radiative transfer; 37, 85, and 157 GHz
Vivekanandan and Adams (1993)	DDA	Hexagonal plates and columns, ice (wavelength not reported).
Dungey and Bohren (1993)	DDA	Hexagonal plates and columns are used to model ice particles; 94 GHz.
Aydin and Tang (1993)	FDTD	Hexagonal plates, columns and stellates (ice phase); 94 and 220 GHz.

Point Matching Techniques

Paper	Technique	Application
Oguchi (1975) Morrison and Cross (1979)	Point Matching	Deformed, spheroidal rain drops.

Table 2.1: A summary of scattering models for nonspherical particles and their applications.

are modelled as oblate and prolate spheroids of varying aspect ratios. The calculations are done at a wavelength of 8.66 *mm* and for various radar elevation angles and canting angles. Results are presented for particles with a major dimension of 0.2 *mm* because he notes that polarization parameters vary by an insignificant amount over the range 0.08 *mm* to 1.0 *mm*; the signals at the smallest wavelengths are masked by the larger particles and particles greater than 1.0 *mm* are thought to precipitate out of the cloud. Overall, circular polarization tends to be more sensitive in the orthogonal channel than linear polarization. Particle orientation effects are significant although the circular depolarization ratio (CDR) is less sensitive to particle orientation than is the linear depolarization ratio (LDR). Radar elevation effects allow one to distinguish between plate-like and columnar particles. Tentative estimates of an average aspect ratio and particle size can be made if assumptions are made about the equivalent cloud water content and the particle size distribution for a given scattering volume. Matrosov (1991b) also estimates the effects of propagation in ice clouds and reports them to be negligible.

In a subsequent paper Matrosov (1991a) uses the Rayleigh model in the same manner to examine the use of elliptically polarized radar signals to measure properties of ice clouds. The most general state of polarization can be described as an ellipse of unit amplitude which is characterized in part by its ellipse polarization angle. If this angle is 0° the result is linear polarization, whereas for an ellipse polarization angle of 45° the result is circular polarization. Any other angle results in elliptical polarization. Matrosov (1991a) shows that for the proper choice of elliptical polarization the backscattered radiation in the cross-polar channel is enhanced yielding a greater sensitivity to radar polarization parameters. If the two complementary elliptical polarization angles of $\pm 22.5°$ are employed, it may be possible to separate the effects of shape and orientation providing an estimate of the mean canting angle and the aspect ratio if assumptions regarding the complex refractive index are made.

To provide depth to this discussion we note that this theory has been applied by researchers for a considerable time (e.g. Atlas et al., 1953; Seliga and Bringi, 1976), although these researchers call it the Gans approximation. Atlas et al. (1953) examines scattering by water and ice hydrometeors at 1, 3 and 10 *cm*. Among other things they suggest that particle shape under both oriented and un-oriented cases is an important factor in explaining the bright band. They also conclude that spheres may be used to model low density ice (especially snow) primarily because of the very low refractive index. In their day, a single radar was not capable of testing these suppositions because radars were not sophisticated enough in terms of polarization capabilities. By the time of the work of Seliga and Bringi (1976) such measurements were feasible and they applied Gans (*i.e.* Rayleigh) theory to the scattering of oblate raindrops in an attempt to ascertain raindrop distribution parameters.

Rayleigh-Gans

The approximation known as Rayleigh-Gans (or sometimes Rayleigh-Gans-Debye) can be applied to "soft" particles; i.e. those particles whose dielectric constants are close to the surrounding medium. One makes the assumptions that the internal electromagnetic field of a particle can be approximated by the applied field and that each subvolume of the particle behaves as an independent Rayleigh scatterer. The total scattered field is determined by the integration over all of the subvolumes.

Matrosov (1992) applies this theory to backscattered returns by snowfall by modelling dry snowflakes as spheres with the complex refractive index adjusted with a mixing rule to account for its low density. He compares Rayleigh, Rayleigh-Gans, and Lorenz-Mie theories and demonstrates a significant discrepancy between the Rayleigh and Lorenz-Mie theories when the optical size $\chi = 2\pi r/\lambda$ exceeds approximately 0.3, whereas Rayleigh-Gans shows reasonable agreement throughout the range of optical size examined ($\chi \sim 4$). Measurements at X- and K_a-bands in snowfall generally confirm the modelling results, lending confidence to the earlier conclusion of Atlas et al. (1953), that spheres should be sufficient to model snow. Another significant result from Matrosov (1992) is that it may be possible to utilize dual-wavelength radar measurements in snowfall to ascertain size distributions and characteristic sizes.

2.1.2 Integral Methods

T-matrix

T-matrix (for transition matrix) method, which is also known as the extended boundary condition method (EBCM) or even the extended integral equation technique, was initially developed by Waterman (1965) for conducting bodies and then later adapted to homogeneous dielectrics by Waterman (1969). The basic concept is to expand the vector Helmholtz equation in terms of spherical wave functions. Barber and Yeh (1975) provide an alternate derivation of the method which seems to be more physically intuitive. Barber and Yeh (1975) apply an equivalence theorem which allows them to cast the scattered field in terms of currents over the dielectric's surface. Vector spherical wave functions are then used to evaluate the scattered field numerically. The resulting integral equations can then be formulated as an exact matrix problem. The transition (T) matrix relates the unknown coefficients of the scattered field to the known coefficients which are associated with the incident wave. Geometrical considerations prove to be the limiting factor; exploitation of symmetry greatly increases the efficiency of the calculations.

Barber and Yeh (1975) compute scattering diagrams (scattering cross section vs. scattering angle) of spheres, oblate and prolate spheroids, and modified cylinders. The results for spheres are qualitatively "correct" (quantitatively the sphere results are validated with

Lorenz-Mie theory). They present results for a variety of optical sizes and dielectric properties, but we will mention only two of their observations. Firstly, they note a distinct difference in the behavior of the differential scattering as a function of scattered angle, between the major and minor dimensions of the particle. That is, if the incident wave is along the major dimension the scattered field is significantly different from the result if the incident wave is in the plane of the minor dimension of the particle. Secondly they observe that cylinders and prolate spheroids of equivalent optical size (well within the resonance region at $\chi \sim 10$) exhibit noticeably different differential scattering characteristics.

Seliga and Bringi (1978) utilize the T-matrix method to validate their earlier calculations of differential reflectivity (Seliga and Bringi, 1976) and to extend their results to include differential phase shift. Their calculations are for raindrops distributed exponentially (a Marshall-Palmer type distribution) and for monodisperse distributions of large hail stones. The rain and hail particles are assumed to be oblate spheroids of a specified aspect ratio and the wavelength considered is 10 *cm*. Their results indicate that the Gans theory and T-matrix method are in excellent agreement for equal volume sphere diameters of up to 6 *mm* in both vertical and horizontal polarizations. They also conclude that measurements of the differential reflectivity and either the absolute reflectivity or the differential phase shift may be used to identify large dry hail stones.

Yeh et al. (1982) utilize the work of Barber and Yeh (1975) to study scattering by single ice needles (prolate spheroids) and plates (oblate spheroids) at 30 *GHz*. Special emphasis is given to canting angle and cross polarization. They find attenuation by ice to be much smaller than in rain primarily due to the small imaginary part of the complex refractive index. They also note that ice plates can induce a stronger cross polarization than ice needles. Induced, cross-polarized fields are only observed for zenith angles other than 0°. Perhaps the most interesting observation is that nonspherical ice particles induce stronger cross-polarized fields than do nonspherical water particles.

The paper of Vivekanandan et al. (1991) furthers the work by modelling polarimetric radar quantities for monodisperse ice hydrometeors at wavelengths of 8 *mm* and 10 *cm*. The ice particles are modelled as prolate and oblate spheroids. They utilize a coordinate system transformation which allows them to compute the T-matrix once for a given particle as defined by its physical and optical properties and then compute the scattered field for a variety of particle orientations. This allows them to examine the sensitivity of monodisperse hydrometeors to variations in compound canting angle. The conclusion of import which can be drawn from this paper in terms of the present work is the sensitivity of the scattering to the canting angle. Their calculations show a marked sensitivity to deviations in the particle's preferred orientation. The degree of this sensitivity depends on how the the canting angle is modelled. For deviations on the order of 20° or less, their work suggests that differential reflectivity (Z_{DR}), specific differential phase (K_{DP}), and backscatter differential phase (δ) are relatively insensitive to canting angle whereas the LDR seems to be most sensitive to such fluctuations.

Fredholm integral equation

The Fredholm integral equation method (FIM) differs from the T-matrix method in that the incident field is related to the scattered field via an integral over the target volume rather than as a surface integral; the internal field as opposed to the surface currents. The development Fredholm integral equation method for ellipsoids has been driven primarily by A. R. Holt (Holt et al., 1978; Holt, 1980). The method has been applied by Shepard et al. (1981) to study scattering by small ice particles at 20 GHz ($\chi \leq 1$, where $\chi = 2\pi a/\lambda$ and a is the major dimension of the particle). They report good agreement between experimentally determined scattering coefficients from discs and needles and values from the FIM. They also report little difference between Rayleigh spheroids and FIM discs and needles in terms of vertical and horizontal scattering amplitudes. The exception is in the backward direction in which shape effects become important even at these small optical sizes.

2.1.3 Discrete Methods

There are two methods which involve the discretization of the scatterer: the finite difference-time domain method (FDTD) and the discrete dipole approximation (DDA). Although these methods were proposed a relatively long time ago, the early seventies for DDA and the early eighties for FDTD), they have only recently become reasonable from a computational standpoint.

FDTD

The FDTD method was originally proposed by Umashankar and Taflove (1982). This method has seen recent application in the work of Aydin and Tang (1993), who apply it to the scattering of linearly polarized radiation by hexagonal ice columns, plates and stellates. They consider frequencies of 94 and 220 GHz. The backscatter cross section is approximately 12 to 15 dB higher for 220 GHz. Also noteworthy is the resonance-like behavior of the horizontal backscatter cross-section of plates and stellates at 220 GHz for particles which are larger than approximately 600 μm at side incidence. This behavior is much more subdued at for normal incidence and is virtually nonexistent for columns. For columns they report an increase of approximately 0.7 to 1.8 in the depolarization ratio from 94 to 220 GHz for the larger crystals ($\geq$ 400 μm) at vertical incidence.

DDA

The physical principles underlying the DDA are detailed in Section 2.2, we will mention only some of the applications. O'Brien and Goedecke (1988) use the DDA to examine the sensitivity of differential and total cross sections to variations in mixing rule and geometrical shape at a wavelength of 1 cm in the resonance region. Mixing rules

are used to adjust the complex refractive index of ice to account for the inclusion of air. They examine the ability of homogeneous circular disks and inscribed and circumscribed oblate spheroids to represent a stellar snow crystal where the mixing rules are used to adjust the complex refractive index based on the relative volumes. A similar procedure is employed for a hexagonal column where a circular cylinder and prolate spheroid are used for comparison. They provide the following tentative recommendations, tentative in that they suggest further calculations should be performed before they be regarded as sound. The modelled geometry should have the same overall linear dimensions as the particle. Secondly the modelled shape should match the distributed mass as accurately as possible as one would intuit. Finally, the Bruggeman mixing rule was the most reliable.

Evans and Vivekanandan (1990) employ the DDA to examine issues of multiparameter radar scattering by randomly oriented (in the plane) hexagonal plates and cylindrical columns and needles which are distributed according to a power law. They report results which indicate that reflectivity changes with bulk density cannot be explained via the standard spherical polarizability term. The differential reflectivity, Z_{DR}, depends on shape primarily as a result of the aspect ratio of the the scatterer. The linear depolarization ratio is sensitive to gross particle shape such that it may be used to distinguish between plate-like and columnar crystals. They also observe that the differential phase shift and the reflectivity may be used to quantify the degree to which the particles are oriented since K_{DP} is sensitive to particle orientation whereas the reflectivity responds to oriented and unoriented particles alike.

The issue of habit discrimination is further explored in Vivekanandan and Adams (1993). The crystal shapes modeled are the same as Evans and Vivekanandan (1990), except the columns were now modeled as hexagonal columns as opposed to cylindrical columns. They employ both monodisperse and modified gamma distributions and experiment with various ice water contents. Their monodisperse results again suggest the ability to discriminate between columns and plates via multiparameter radar measurables. The modified gamma distribution tends to dampen the variations in reflectivity for a given habit. They indicate that either of the following combinations appear to be most useful to discriminate between plates, needles and columnar crystals: horizontal reflectivity (Z_{HH}) and differential phase shift (K_{DP}) or differential reflectivity (Z_{DR}) and correlation ($\rho(h,v)$). They do not indicate which wavelength is used. They also mention that the relationship connecting reflectivity-factor and IWC seems to be only nominally dependent upon parameters of the distribution.

Dungey and Bohren (1993) use the DDA (which they call the coupled dipole method) to examine backscattering by hexagonal columns and plates at 94 GHz. They emphasize that backscattering is the most severe test for any scattering model as is discussed elsewhere (see Section 2.2.3 and Bohren and Singham, 1991). They focus on the sensitivity of backscattering to unpolarized as well as horizontal and vertical polarizations at

several zenith angles as a function of the size parameter. In general, as the size parameter (based on the diameter of an equal volume sphere in this case) increases from $\sim$ 1.0 to $\sim$ 2.4 the backscattered intensity displays a local maximum, then a local minimum, and then proceeds to grow to an even greater undetermined value (results were truncated at this point). They observe the first scattering minimum which they suggest as being important in a possible retrieval scheme involving the Doppler velocity of the particles. Generally, the first maxima and minima are better defined and more pronounced for the columns than the plates. There is a strong dependence of these minima on zenith angle. This dependence is expected to disappear if the ice particles lose their orientation which could provide information regarding the turbulent nature in a cloud if the habits can be determined independently.

2.1.4 Point Matching Techniques

Point matching techniques are physically exact methods in the same sense in which the integral methods are exact; exact in a mathematical sense. They are all inexact in a computational and geometrical sense although these problems can be dealt with.

The concept of the point matching technique is to employ regular vector spherical harmonics to express the internal and external fields. The external field is the superposition of the incident and scattered field. The boundary conditions at the particles surface are applied to "match" the internal and external fields - hence the name of the method. There are two variants of the point matching technique. The approach of Oguchi (1973) is a straight forward collocation of these fields at the boundary of the particle. The second variant employs least squares fitting to match the fields at the boundary as is done in Morrison and Cross (1979) and Oguchi and Hosoya (1974). Their results are used to study scattering by deformed rain drops. We will not discuss their results further as they have been applied primarily to hydrometeors in the water phase and we are interested in ice. There is no reason why this method can not be applied to ice, however.

One final comment pertaining to these papers. Morrison and Cross (1979), Oguchi (1973) and Oguchi (1975) discuss perturbation methods which assume that the scatterer is a slightly deformed sphere. These methods are not detailed here as they are only applicable to slightly deformed particles.

2.1.5 Some Remarks

There are a number of reviews in the literature pertaining to the subject of this section, we conclude by mentioning three of them. Holt (1982) primarily focusses on the implementational aspects of the point matching technique, the T-matrix method, the unimoment method, and the Fredholm integral equation method, and an inter-comparison amongst these methods. He also discusses approximations which may be obtained by special considerations of size, orientation and frequency. Mon (1982) reviews methods

for both spheres and nonspheres as well as various approximations. His list is nearly identical to Holt (1982) although he omits the unimoment method which we have done in this review as well. Mon (1982) also explores issues pertaining to scattering by oriented clouds of ice particles distributed exponentially. Bohren and Singham (1991) review several of the methods above and add the DDA. They emphasize the special nature of scattering in the backward direction and address statistical issues which may shed some light on scattering by ensembles of nonspherical particles.

Of course one may always use equivolume spheres with the Lorenz-Mie theory or Rayleigh approximation to model scattering by nonspherical hydrometeors. We have omitted theories for spheres from the list since we are exclusively interested in theories for nonspherical particles. The scattering theory of spheres is well known and documented (e.g., Van de Hulst, 1981; Bohren and Huffman, 1983) and the reader who is unfamiliar with scattering theory in general is encouraged to consult the two works just cited. One may speculate that spheres could prove useful under some circumstances, such as spacial dendrites which tumble. When considering a statistical sampling of such scatterers which would present approximately spherical geometrical cross sections, it is feasible that one may apply ice spheres with the appropriate mixing rule. Such a study has been done in Pazmany et al. (1993). In this study Lorenz-Mie theory is used in conjunction with it in situ ice particle measurements to simulate the 95 GHz radar measurements. The Lorenz-Mie theory performed well (once the appropriate mixing rule was used) for some cases but very poorly for others. One may further speculate, based on their reported results of microphysical measurements, that the above speculation regarding tumbling crystals is correct.

As can be seen from the dates of these papers the T-matrix approach has seen extensive application for nearly two decades and should continue to remain useful. It appears however, that the Fredholm integral equation method has grown out of favor at least within the community of researchers working on scattering problems for hydrometeors. Also somewhat out of favor is unimoment and point matching techniques. This list is not complete as it ignores methods (such as Fuller, 1993) which have not yet been applied to microwave problems.

2.2 THE DISCRETE DIPOLE APPROXIMATION

An efficient method to compute the scattering and absorption properties of dielectric particles of arbitrary shape has long been sought. One such method was devised by Purcell and Pennypacker (1973) and although it may not entirely meet the efficiency criteria it is entirely general. Their method has come to be known by many names, but we will refer to it here as the discrete dipole approximation (DDA). In this section we will discuss the basic concept underlying the DDA, the specific implementation used in this study and then provide a simple illustrative example of dipole scattering.

2.2.1 The Physics

Although it can be computationally expensive or even prohibitive in many circumstances, the method of Purcell and Pennypacker is a physically intuitive solution to scattering by arbitrarily shaped dielectric particles. Purcell and Pennypacker posed the problem not as a boundary value problem but as a finite element problem. They envisaged a particle comprised of many "polarizable atoms" which exist in a vacuum. They take it as understood that the "atoms" are of point-like nature. These "atoms" are arranged on a cubic lattice and are each assigned a complex polarizability $\alpha(\omega)$ to reproduce the bulk dielectric constant of the material.

The instantaneous electromagnetic field at any given lattice site is determined by the sum of the incident electromagnetic field and the electromagnetic field caused by all of the other dipoles. When excited by an external source of radiation (i.e. an incident plane wave of frequency ω), each "atom" behaves as a dipole, absorbing and scattering radiation according to its polarizability tensor. The far-field scattered radiation can then be obtained by linear superposition of the radiation emitted by each dipole. It should be noted that, implicit in this formulation is the omission of self terms; the radiation reaction of a given dipole on itself. Later implementations such as those of Draine (1988) and Goedecke and O'Brien (1988) incorporate these self terms.

This is the essence of the discrete dipole approximation, it is a physically and mathematically straight forward approach to scattering. At the heart of the DDA is dipole radiation, a very basic concept in physics. It is a very complex book-keeping exercise, however, and in many senses it is in the implementation where the difficulties arise. To reiterate, it is an approximate method yet it is entirely general.

2.2.2 The Implementation

Sufficient algorithmic variations fall under the rubric of the discrete dipole approximation (which is also known under other aliases such as the coupled-dipole method and the scattering-orders approach as in Bohren and Singham (1991)) to merit a detailed discussion of the specific variant used here. The algorithm of Goedecke and O'Brien (1988) forms the basis of the model used in this research. The FORTRAN code was written by K. F. Evans and first appears in the literature in Evans and Vivekanandan (1990). From this point on this particular model will be referred to as the implementation of Evans.

The task is to find the scattered electromagnetic field $\mathbf{E}(\mathbf{r})$ at all points in space due to the interaction of an incident electromagnetic wave $\mathbf{E}^{\mathbf{in}}(\mathbf{r})$ and an arbitrary dielectric particle. The particle is defined by its optical properties and by the arrangement of cubic dipolar cells of size d on a uniform rectangular Cartesian grid. Note that often times d is referred to as the dipole size, however this is somewhat of a misnomer since dipoles are to be thought of as having a point-like nature. It is perhaps better to think of d as an

inter-dipole separation. The geometrical center of the particle is placed at the origin of the coordinate system and the Cartesian grid is arranged such that the dipolar cells fit across each dimension in an integral fashion; i.e. the origin lies either between two cells or at the center of a cell accordingly. The maximal dimensions of the Cartesian lattice are determined and then each cell on the Cartesian lattice is polled to determine if it is a part of the particle according to standard geometrical formulae; e.g. spheres, ellipsoids, hexagonal plates and columns, cylinders, etc. More complex shapes can be neatly handled in an approximate fashion by the methods of Wang (1987). If a cell is not a part of the particle it is rendered optically inert by setting its susceptibility to zero. It is the complex susceptibility χ which determines the optical properties and is related to the complex refractive index m by $\chi = (1/4\pi)\left[m^2 - 1\right]$. Each cell is further subdivided to facilitate determination of the volume fraction V_f of each cell which lies on the edge of the particle. This allows better resolution of the fine features of the particle's edges. Cells which have volume fractions less than one have their susceptibility reduced (χ_{eff}) according to the Lorentz-Lorenz mixing rule:

$$\frac{\chi_{eff}}{4\pi\chi_{eff} + 3} = V_f \frac{\chi}{4\pi + 3}. \tag{2.1}$$

The cell size is restricted by the criteria $|m|kd \ll 1$, which states that the amplitude and phase of the internal field must be virtually constant across the cell, $k = 2\pi/\lambda$ is the wave number for free-space wavelength λ. In practice, Goedecke and O'Brien have shown that $|m|kd < 1$ is adequate. In our studies, the criteria $|m|kd < \frac{1}{3}$ was employed for higher accuracy.

Since the nature of the problem is to find harmonic solutions to a wave equation, we may apply the method of Green's functions. Beginning with Maxwell's equations, Goedecke and O'Brien show that the electric field at all points $\mathbf{r}$ in space can be described in terms of the dyadic Green's function G by

$$\mathbf{E}(\mathbf{r})\left[1 + (4\pi/3)\chi(\mathbf{r})\right] = \mathbf{E}^{\mathbf{in}}(\mathbf{r}) + \int d^3r' G(\mathbf{r} - \mathbf{r}') \cdot \mathbf{p}(\mathbf{r}) \tag{2.2}$$

where $\mathbf{p}(\mathbf{r}) = \chi(\mathbf{r})\mathbf{E}(\mathbf{r})$ is the dielectric polarization. Equation (2.2) is discretized into (with some rearrangement):

$$E^{in}_{\alpha,\mathrm{i}} = \left[\chi_\alpha^{-1} + 4\pi/3\,(1 - \Gamma)\right] p_{\alpha,\mathrm{i}} - d^3 \sum_{\beta \neq \alpha} \sum_{\mathrm{j}} G_{\mathrm{i,j}}(r_\alpha - r_\beta)\, p_{\beta,\mathrm{i}} \tag{2.3}$$

where $p_{\alpha,\mathrm{i}} = \chi_\alpha E_{\alpha,\mathrm{i}}$. The system of linear equations represented by (2.3) can be compactly expressed in matrix form as

$$\tilde{\mathbf{A}}\vec{\mathbf{p}} = \vec{\mathbf{E}}^{in}, \tag{2.4}$$

where $\tilde{\mathbf{A}}$ is a $3N \times 3N$ complex matrix which contains the information pertaining to dipole-dipole interactions in the off-diagonal elements and the self-interaction terms as

well as the susceptibilities along the diagonal. Note that in transgressing from equation (2.2) to (2.3) an additional term Γ appears. Γ represents the small contribution to the integral in (2.2) of the self-reaction of the dipole. Γ has been extracted out of the integral and is treated separately, thus in discretizing the integral we omit the cases where $\beta = \alpha$. Goedecke and O'Brien model the self-term as

$$\Gamma = (3/4\pi)^{\frac{2}{3}} \left(kd^2\right) - i\left(kd\right)^3/2\pi. \tag{2.5}$$

Here i is the imaginary number, $i = \sqrt{-1}$. In this section the Roman characters 'i', 'j', and 'k' will be used to denote indices, k is the wavenumber, and $\hat{\mathbf{k}}$ is the propagation vector. To ensure agreement with the optical theorem[1], Goedecke and O'Brien show that the imaginary part of (2.5) must be retained. This is crucial for the implementation of Evans as the optical theorem is used as a consistency check.

Equation (2.3) is comprised of two parts on the right hand side: the first component is the incident field plus the self-term and the second component accounts for the interaction between the dipoles thus revealing the nature of the Green's function. We see that the Green's function $G(\mathbf{R})$ relates electric field at position α due to the electric field of another dipole at position β and is dependent only upon the dipole separation $\mathbf{R} = \mathbf{r}_\alpha - \mathbf{r}_\beta$:

$$G(\mathbf{R}) = \frac{1}{R}\exp\left(-ikR\right)\left[k^2\left(\delta_{\mathrm{i,j}} - \hat{R}_\mathrm{i}\hat{R}_\mathrm{j}\right) - \left(\delta_{\mathrm{i,j}} - 3\hat{R}_\mathrm{i}\hat{R}_\mathrm{j}\right)\left(\frac{1}{R^2} + \frac{ik}{R}\right)\right]. \tag{2.6}$$

The incident plane wave at dipole α with position $\mathbf{r}_\alpha$ is modeled as

$$\vec{\mathbf{E}}_\alpha^{in}\left(\hat{\mathbf{k}}'\right) = \mathbf{E_o}\exp\left(-ik\hat{\mathbf{k}}'\cdot\mathbf{r}_\alpha\right), \tag{2.7}$$

where the incident direction is indicated by $\hat{\mathbf{k}}'$. $\mathbf{E_o}$ has unit amplitude, $|\mathbf{E_o}| = \mathbf{1}$, and is either vertically or horizontally polarized. The vertical and horizontal polarization are denoted respectively by the unit vectors $\hat{\mathbf{V}}$ and $\hat{\mathbf{H}}$ and are defined such that $\hat{\mathbf{V}} \times \hat{\mathbf{H}} = \hat{\mathbf{k}}$, where $\hat{\mathbf{k}}$ is the direction of propagation. The geometry can be understood with the aid of a sphere. Imagine a sphere with $\hat{\mathbf{k}}$ originating at the center of a sphere and passing through the equator. $\hat{\mathbf{V}}$ is the unit vector beginning at the center of the sphere and pointing at the pole with a positive vertical 'z' component. Then by default $\hat{\mathbf{H}}$ lies in the equatorial plane perpendicular to $\hat{\mathbf{k}}$ and $\hat{\mathbf{V}}$. The coordinate system for the scattering calculations is defined by $\hat{\mathbf{k}}$ and the local vertical axis (z).

In the implementation of Evans, there are two methods available to obtain the desired dipole polarizations $\vec{\mathbf{p}}$; direct inversion and conjugate gradient minimization. Direct

---

[1] In Goedecke and O'Brien (1988), the optical theorem is defined in terms of the extinction, scattering and absorption cross sections (σ_e, σ_s, and σ_a respectively) by the two equations: $\sigma_e = 4\pi k^{-2}\Re[\mathbf{E_o^*}\cdot\mathbf{F}(\hat{k})]$ and $\sigma_e = \sigma_s + \sigma_a$. See text for definitions.

inversion approaches the problem in the form of Equation (2.4). The dipole polarizations $\vec{\mathbf{p}}$ are solved for by inverting $\tilde{\mathbf{A}}$. This method has the advantage that once $\tilde{\mathbf{A}}$ is inverted then many incident and outgoing angles can be solved for with little expense. Memory usage for the matrix inversion technique, however, requires the storage of $(3N)^2$ complex elements, while CPU usage scales as $(3N)^3$. In practice it is the memory limitations which renders this method impractical for many of the applications in this study. As an example consider a particle composed of 2000 dipoles (some of the particles modeled in Chapter 3 consist of approximately 14000 dipoles): such a particle would require about 275 megabytes of memory! Thus the workhorse for the calculations presented in this research was the conjugate gradient-FFT method.

The basic notion of the conjugate gradient method is to iterate $\vec{\mathbf{p}}$ until the residuals of (2.3) are at or below some acceptable value. Conjugate gradient minimization employs FFT's to execute the convolution sum of the Green's function and the dipole polarizations. The Green's function transform is precomputed once. Then for each convolution the polarization vector is transformed, multiplied by the precomputed transform of the Green's function and then an inverse FFT. This technique is very fast even for very great numbers of dipoles because the FFT convolution process scales as order $N \log_2 N$. The number of floating point operations for this method scales as $C\ N \log_2 N$ where C is some large prefactor which depends on the number of iterations, the fact that the FFT arrays are 8 times as large as N, and some constants due to geometry and the FFT itself.

Once $\vec{\mathbf{p}}$ is determined the scattered far field $\mathbf{E}_s(\hat{\mathbf{k}})$ can be related to the incident electric field $\mathbf{E}_i(\hat{\mathbf{k}}')$ via the scattering amplitude matrix

$$\begin{bmatrix} \mathbf{E}_{v,s} \\ \mathbf{E}_{h,s} \end{bmatrix} = \frac{\exp(-ikr)}{ikr} \begin{pmatrix} \mathbf{F}_{vv} & \mathbf{F}_{vh} \\ \mathbf{F}_{hv} & \mathbf{F}_{hh} \end{pmatrix} \begin{bmatrix} \mathbf{E}_{v,i} \\ \mathbf{E}_{h,i} \end{bmatrix}. \tag{2.8}$$

The subscripts v and h indicate vertical and horizontal polarization. Note that each pair of subscripts indicate the incident and scattered polarizations, respectively. The elements of the scattering amplitude matrix are determined from $\vec{\mathbf{p}}$ for each combination of incident $\hat{\mathbf{k}}'$, and outgoing $\hat{\mathbf{k}}$ directions:

$$\mathbf{F}_{\mathrm{i}}\left(\hat{\mathbf{k}}\right) = \sum_{\mathrm{j}} \left(\delta_{\mathrm{ij}} - \hat{k}_{\mathrm{i}}\hat{k}_{\mathrm{j}}\right) i\,(kd)^3 \sum_{\alpha} \exp\left(ik\hat{\mathbf{k}}\cdot\mathbf{r}_{\alpha}\right) \mathbf{p}_{\alpha \mathrm{j}}. \tag{2.9}$$

The scattering amplitudes are derived from the far field limit ($R \to \infty$) of (2.6). The Cartesian components i,j of (2.9) are projected onto the polarization vectors $\hat{\mathbf{V}}$ and $\hat{\mathbf{H}}$ in (2.8). It follows that the scattering (Mueller) matrix is given by (e.g., Ulaby and Elachi, 1990; Van de Hulst, 1981; van Zyl, 1989):

$$\mathbf{S} = \sum_{l} n_l \begin{pmatrix} \left(|F_{vv}|^2 + |F_{vh}|^2 + |F_{hv}|^2 + |F_{hh}|^2\right)/2 & \left(|F_{vv}|^2 - |F_{vh}|^2 + |F_{hv}|^2 - |F_{hh}|^2\right)/2 \\ \left(|F_{vv}|^2 + |F_{vh}|^2 - |F_{hv}|^2 - |F_{hh}|^2\right)/2 & \left(|F_{vv}|^2 - |F_{vh}|^2 - |F_{hv}|^2 + |F_{hh}|^2\right)/2 \\ Re\left(F_{vv}F_{hv}^* + F_{vh}F_{hh}^*\right) & Re\left(F_{vv}F_{hv}^* - F_{vh}F_{hh}^*\right) \\ Im\left(F_{vv}F_{hv}^* + F_{vh}F_{hh}^*\right) & Im\left(F_{vv}F_{hv}^* - F_{vh}F_{hh}^*\right) \end{pmatrix}$$

$$\begin{pmatrix} Re\left(F_{vv}F_{vh}^{*}+F_{hv}F_{hh}^{*}\right) & -Im\left(F_{vv}F_{vh}^{*}+F_{hv}F_{hh}^{*}\right) \\ Re\left(F_{vv}F_{vh}^{*}-F_{hv}F_{hh}^{*}\right) & -Im\left(F_{vv}F_{vh}^{*}-F_{hv}F_{hh}^{*}\right) \\ Re\left(F_{vv}F_{hh}^{*}+F_{vh}F_{hv}^{*}\right) & -Im\left(F_{vv}F_{hh}^{*}-F_{vh}F_{hv}^{*}\right) \\ Im\left(F_{vv}F_{hh}^{*}+F_{vh}F_{hv}^{*}\right) & Re\left(F_{vv}F_{hh}^{*}-F_{vh}F_{hv}^{*}\right) \end{pmatrix} \tag{2.10}$$

where n_l is the number concentration of the particles and $\mathbf{S}$ has units of inverse length. The subscripts indicate the incident and outgoing polarizations respectively. Equation (2.10) represents an incoherent average over an ensemble of particles at various orientations (when orientation averaging is invoked). In general, the Mueller matrix elements are computed for each combination of incident and scattered angles. In monostatic radar applications, however, $\hat{\mathbf{k}}$ is taken to be in the direction of backscattering in (2.9), and the Mueller matrix is expressed in terms of backscattering. As discussed in Section 2.3, azimuthal averaging is performed to simulate randomly oriented particles in the plane.

The appropriate extinction matrix in terms of the forward scattering elements is

$$\mathbf{K} = \begin{pmatrix} Re\left(M_{vv}+M_{hh}\right) & Re\left(M_{vv}-M_{hh}\right) & Re\left(M_{vh}+M_{hv}\right) & Im\left(M_{vh}-M_{hv}\right) \\ Re\left(M_{vv}-M_{hh}\right) & Re\left(M_{vv}+M_{hh}\right) & Re\left(M_{vh}-M_{hv}\right) & Im\left(M_{vh}+M_{hv}\right) \\ Re\left(M_{hv}+M_{vh}\right) & Re\left(M_{hv}-M_{vh}\right) & Re\left(M_{vv}+M_{hh}\right) & Re\left(M_{vv}-M_{hh}\right) \\ Im\left(M_{hv}-M_{vh}\right) & -Im\left(M_{vh}+M_{hv}\right) & Re\left(M_{vv}-M_{hh}\right) & Re\left(M_{vv}+M_{hh}\right) \end{pmatrix} \tag{2.11}$$

where the individual elements are given in terms of the forward scattering amplitudes $F_{\mathrm{ij}}\left(\hat{k}\right)$ by

$$M_{\mathrm{ij}} = \sum_{l} n_l \frac{2\pi i}{k} F_{l,\mathrm{ij}}\left(\hat{k}\right). \tag{2.12}$$

The Mueller matrix contains all of the scattering information and can be used to derive the more familiar radar parameters as discussed in Appendix A.2.

A final comment regarding the implementation of Evans is in order before we conclude this discussion. Although absorption has not been discussed, the DDA model of Evans does indeed compute the absorption. We have omitted any discussion of absorption as it is not utilized in this work.

2.2.3 Sensitivity to Backscattering and an Illustration of Dipole Scattering

As was discussed above the underlying premise of the DDA is that the scattered electromagnetic wave can be obtained by summing over the contributions of numerous dipolar units. An angular dependence of the scattered intensity results from the phase differences between individual scattered waves. The phase difference between any two given dipoles depends upon the relative position of the dipoles and the direction of the scattered waves. A small scale version of the discrete dipole approximation can be used to illustrate the sensitivity of backscattering to particle shape and as a means of insight into the DDA method. We shall begin by revisiting the analysis of Bohren and Singham (1991).

Consider an electromagnetic wave impinging upon two dipoles. The waves propagation vector lies in a plane defined by the two dipoles. For the moment the dipoles are assumed to be non-interacting and polarization will be ignored. We will relax these conditions later in our numerics. Under these conditions the phase difference between the scattered waves of the two dipoles is given by

$$\varphi = k\left[\mathbf{r}\cdot(\hat{\mathbf{e}}_{in} - \hat{\mathbf{e}}_s)\right] \tag{2.13}$$

where k is the wave number, $\mathbf{r}$ is the relative position of the two dipoles, and $\hat{\mathbf{e}}_{in}, \hat{\mathbf{e}}_s$ are unit vectors specifying the direction of the incident and scattered waves, respectively. To simplify matters Bohren and Singham let $\mathbf{r}\cdot\hat{\mathbf{e}}_{in} = r$, that is, the direction of propagation of the incident wave is *parallel* to the dipole direction vector in which case

$$\varphi = kr\,(1 - \cos\theta)$$

for scattering angle θ where $\mathbf{r}\cdot\hat{\mathbf{e}}_s$ reduces to $r\cos\theta$. Differentiating with respect to the dipole separation r one finds that

$$\frac{\partial\varphi}{\partial r} = k\,(1 - \cos\theta)\,.$$

Thus, the scattering is least sensitive to changes in dipole separation in the forward direction ($\theta = 0$) and most sensitive in the backward direction ($\theta = \pi$). In their analysis Bohren and Singham argue on physical grounds that this result holds for an arbitrary number of dipoles (which is just the principle of linear superposition) and for the inclusion of dipole interactions. The latter argument is supported via calculations which suggest that dipole interactions actually increase the sensitivity for backscattering.

In this simple example it is evident that changing the dipole separation is equivalent to changing the particle shape for a given wavelength. Thus the conclusion that scattering is most sensitive in the backward direction to changes in dipole separation suggests that scattering is most sensitive in the backward direction for changes in particle shape. With the aid of Mathematica (software for symbolic and numeric manipulations) to alleviate the tedium of symbolic matrix manipulation, it is possible to analytically solve the coupled dipole problem for small numbers of dipoles. This exercise is useful as it illustrates how the discrete dipole method works, and can test some of the above assertions.

Flatau et al. (1990) formulate the discrete dipole approximation in a convenient form for the small dipole problem. The basic idea is to compute the dipole moment of the particle (in this case composed of two dipoles [2]) from which the scattered intensity can

---

[2]This represents the solution to problem 5.6 of Stephens (1994)

be obtained. For a given incident wave $\vec{E}_{inc_j}$ at the j^{th} dipole, one can obtain the dipole moment $\vec{\mathbf{p}}$ from

$$\sum_{k=1}^{N} \mathbf{A}_{j,k}\vec{\mathbf{p}} = \vec{\mathbf{E}}_{inc_j} \qquad (j = 1, 2, \ldots N).$$

Here $\mathbf{A}_{j,k}$ is the $3N \times 3N$ dipole interaction matrix for dipole k acting on dipole j and N is the number of dipoles. For the $N = 2$ case, the dipole interaction matrix is given by

$$\mathbf{A}_{1,2} = \mathbf{A}_{2,1} = -\frac{k^2 e^{ikr}}{r}\begin{pmatrix} 1 & 0 & 0 \\ 0 & 0 & 0 \\ 0 & 0 & 1 \end{pmatrix} + \frac{(1-ikr)\,e^{ikr}}{r^3}\begin{pmatrix} 1 & 0 & 0 \\ 0 & -2 & 0 \\ 0 & 0 & 1 \end{pmatrix}, \qquad j \neq k$$

and

$$\mathbf{A}_{1,1} = A_{2,2} = \frac{1}{\alpha}\begin{pmatrix} 1 & 0 & 0 \\ 0 & 1 & 0 \\ 0 & 0 & 1 \end{pmatrix}, \qquad j = k.$$

As before $k = \frac{2\pi}{\lambda}$ is the wavenumber for wavelength λ, and α is the polarizability. In this formulation all dipole-dipole interactions are included, including the self term (radiative reaction; *i.e.* the $A_{i,i}$) through the polarizability (Draine, 1988):

$$\alpha = \alpha_o \left[1 - i\frac{2\,(ka_{eq})^3}{3N} \cdot \frac{m^2 - 1}{m^2 + 2}\right]^{-1}$$

where

$$\alpha_o = \frac{3}{4\pi n} \cdot \frac{m^2 - 1}{m^2 + 2},$$

n is number density of dipoles, $a_{eq} = (3N/4\pi n)^{1/3}$, and m is the refractive index. The problem was solved for an incident plane wave travelling along the x-axis in the x-y plane with horizontal and vertical polarization. The dipoles were also in the x-y plane, oriented along the y-axis corresponding to the second case discussed above. Solutions were obtained for $N = 1$ (simple Rayleigh scattering by a sphere), $N = 2$, and $N = 4$ dipoles. The interaction matrix for $N = 4$ dipoles is not presented due to its similarity to the solution above and its cumbersome nature. Results are presented as a function of scattering angle θ. The results are normalized to the maximum value (corresponding to $N = 4$ dipoles at $\theta = 0, \pi$), and the dipole separations, r, were adjusted to preserve volume. The data are presented in Figure 2.1.

From Figure 2.1, since the particle volume remains the same in all three cases, it can be concluded that it is the shape (or relative dipole separations) which is causing the variation in scattered intensities. As one further test, the differential reflectivities (Z_{DR} is based on both the horizontally and vertically backscattered intensities as defined in A.2) were computed for the $N = 2$ and $N = 4$ cases and were found to be significantly different: $Z_{DR,N=2} = 1.24$ and $Z_{DR,N=4} = 2.11\ dBZ$.

The backward-forward asymmetry is not visible in Figure 2.1 because we are only looking at one orientation. To see the backward-forward assymetry and to demonstrate

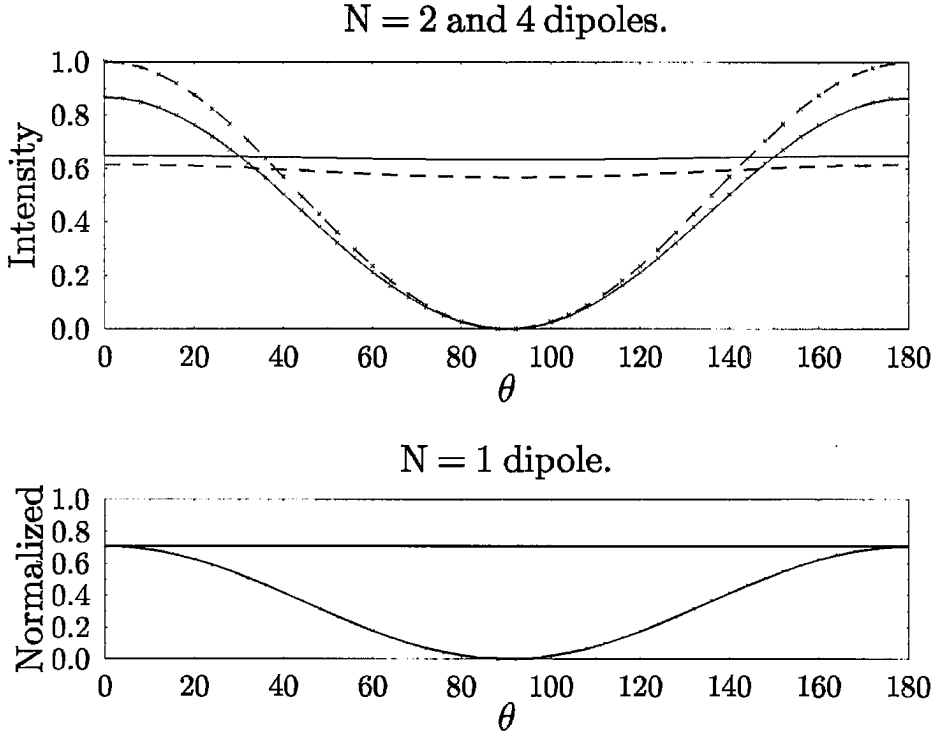

Figure 2.1: Scattering by N=1, 2, and 4 dipoles, oriented along the y-axis for an incident wave propagating along the x-axis. Note: $\lambda = 0.70\mu m$, and $m = 1.31$.

the sensitivity in the backward direction, calculations were done for a pair of dipoles average over 12 planar orientations. The incident radiation was unpolarized and had a wavelength of 0.7 μm and $m = 1.31$. There were three different sets of dipole seperations (in triplets): $d = 0.17 \pm .01$, $d = 0.35 \pm .01$, and $d = 0.70 \pm .01$. The results are presented in Figure 2.2. The backward-forward assymmetry develops as the dipole separation increases transgressing from a Rayleigh-like pattern for $d = 0.17$ to a highly asymetric pattern for $d = 0.70$. In looking at Figure 2.2, it is apparent that small changes in dipole separation lead to sensitivities in the near forward and near backward directions. The sensitivity seems to shift towards the backward direction for $d = 0.70$ although this cannot be ascertained with any degree of confidence. Note that the intensity is proportional to the magnitude of the electromagnetic field and that phase difference appears in the electric field as the argument of the complex exponential function. This might be described as a highly nonlinear system, and although Bohren and Singham's phase difference argument is instructional it cannot be entirely generalized. An additional complicating factor which cannot be accounted for in such a simple argument is the interaction of dipoles. In summary, it is quite remarkable that such a simple scattering system can exhibit such complex behaviour.

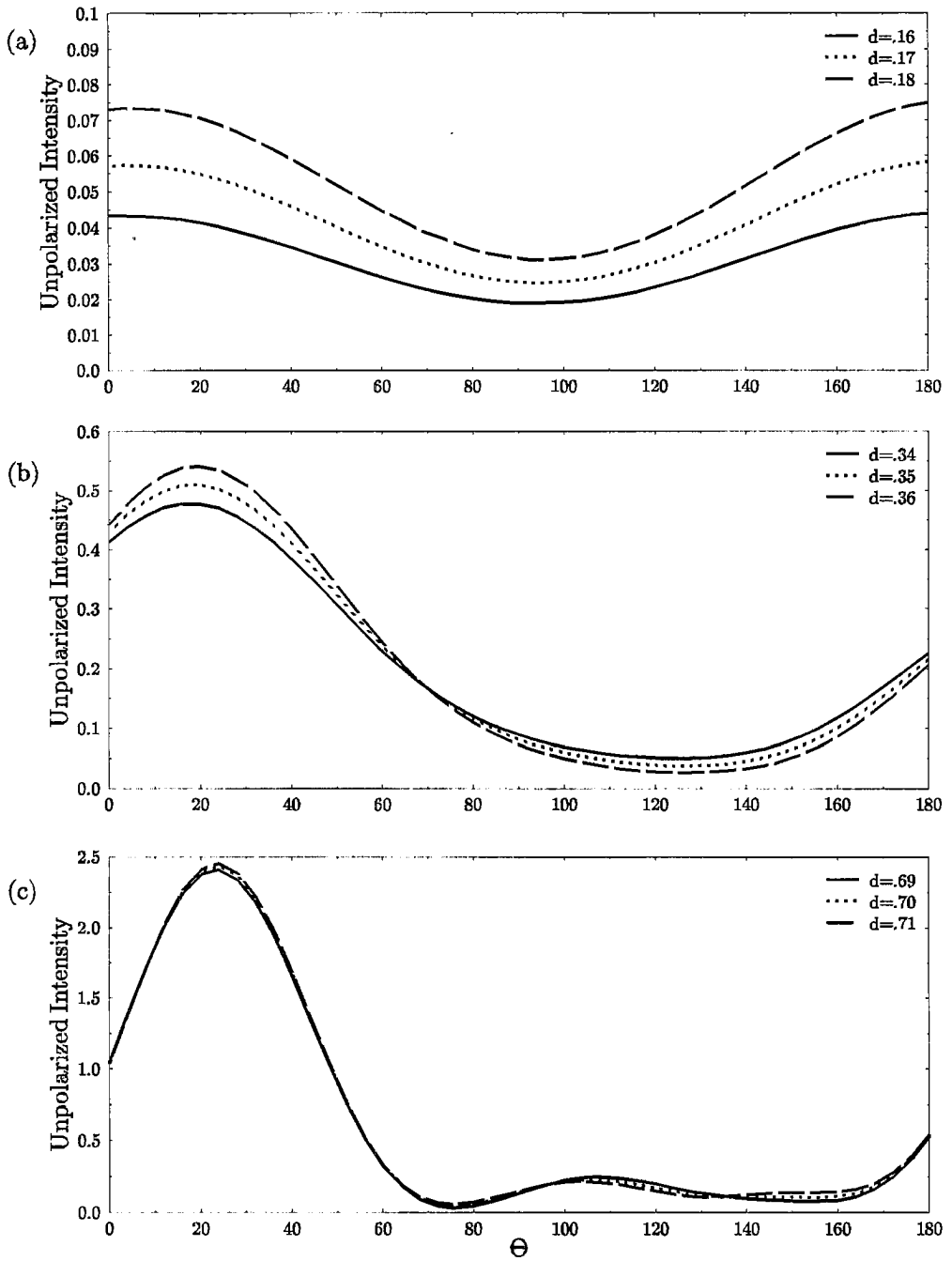

Figure 2.2: Normalized scattering intensity for two dipoles averaged over 12 dipole orientations. Dipole separations are indicated in the key. Note: $\lambda = 0.70\mu m$, and $m = 1.31$.

2.3 AN ASSUMPTION: RANDOM ORIENTATION

As discussed in Section 4.1, naturally occurring ice particles of the size and habit with which we are concerned tend to fall with their major dimension oriented horizontally. (There are exceptions to this rule, such as short columns which possess relatively large aspect ratios, where the aspect ratio is defined as the ratio of the minor to the major dimension. These particles will exhibit a more complex behaviour as they fall). Given a large distribution of such particles it is reasonable to assume that the particles will be randomly-oriented in this plane. Thus the major dimension of any particular ice particle will lie horizontally and each azimuthal orientation will occur with equal probability. In reality the hydrometeor's horizontal inclination is likely to deviate from this horizontal mode in some distributed fashion. This deviation is known as the canting angle, and will be neglected in this study. To simulate this random orientation azimuthal averaging is performed over several incident directions. This section seeks to determine how many angles are required to be averaged to ensure a satisfactory representation of randomly oriented particles.

It should be noted that the number of solutions in the DDA model is directly proportional to the number of azimuth angles averaged. Because the DDA can be computationally expensive, even a small difference in the number of azimuth angles can be significant. The methodology of this section is relatively straight forward. For several different morphologies, the discrete dipole model was run with an ever increasing number of azimuthally averaged angles. The particle is determined to be randomly oriented when the output ceases to vary significantly relative to a reference case of 12 azimuthally averaged angles. The calculations were performed at a wavelength of 3.16 mm. The number of dipoles were fixed across the minor dimension; 4 dipoles for plates and six dipoles for the other morphologies. Results can be extended to other wavelengths by consideration of the dependance of azimuthal averaging on optical size. The data are presented in Tables 2.2 and 2.3 in the form of fractional differences [%]. The fractional difference is defined to be

$$F = 100 \left(\frac{|F_{N_{az}=12,pol}|^2 - |F_{N_{az},pol}|^2}{|F_{N_{az}=12,pol}|^2} \right) \quad [\%].$$

The polarization, denoted by the subscript pol, is either HH or VV.

As is evident from Tables 2.2 and 2.3, azimuthal averaging is sensitive to shape, optical size, polarization and radar elevation angle. The differences between polarizations are relatively small in comparison to the effects of shape, optical size and elevation. Any value $\leq 1\%$ is deemed acceptable. This value offers an appropriate compromise between accuracy and expediency and was determined subjectively by inspection of Tables 2.2 and 2.3. The most severe test of averaging is for edge on incidence ($\theta = 0°$). The number of azimuthal angles to be averaged which were used in Chapter 4 are summarized in Table 2.4.

Polarization HH

Crystal	$N_{az}=2$	$N_{az}=3$	$N_{az}=4$	$N_{az}=5$	$N_{az}=6$	$N_{az}=8$
(a) $\Theta = 90°$						
Hex. Plate (*1mm*)	0.0006	0.0001	0.0000	0.0000	0.0000	0.0000
Hex. Plate (*2mm*)	0.0000	0.0001	0.0009	0.0000	0.0000	0.0000
Cylinder (*1mm*)	3.1172	0.0008	0.0007	0.0004	0.0000	0.0000
Cylinder (*2mm*)	4.6825	0.0005	0.0010	0.0001	0.0005	0.0005
Rosette-3 (*1mm*)	0.0003	0.0002	0.0000	0.0001	0.0000	0.0003
Rosette-3 (*2mm*)	0.0004	0.0001	0.0000	0.0002	0.0000	0.0000
Rosette-4 (*1mm*)	0.0000	0.0000	0.0000	0.0000	0.0000	0.0000
Rosette-4 (*2mm*)	0.0004	0.0000	0.0004	0.0000	0.0000	0.0004
(b) $\Theta = 60°$						
Hex. Plate (*1mm*)	0.0580	0.0068	0.0000	0.0001	0.0000	0.0000
Hex. Plate (*2mm*)	0.2744	0.1700	0.0003	0.0001	0.0001	0.0001
Cylinder (*1mm*)	6.1621	0.1890	0.0021	0.0003	0.0003	0.0004
Cylinder (*2mm*)	23.7574	2.5857	0.1563	0.0059	0.0006	0.0001
Rosette-3 (*1mm*)	0.0710	0.1909	0.0034	0.0019	0.0011	0.0006
Rosette-3 (*2mm*)	0.2697	2.2944	0.0011	0.0011	0.0015	0.0005
Rosette-4 (*1mm*)	1.6893	0.0000	0.0034	0.0000	0.0000	0.0000
Rosette-4 (*2mm*)	11.6761	0.0000	0.1689	0.0000	0.0000	0.0000
(c) $\Theta = 30°$						
Hex. Plate (*1mm*)	0.1880	0.0745	0.0002	0.0000	0.0001	0.0002
Hex. Plate (*2mm*)	1.3820	4.4352	0.0225	0.0250	0.0417	0.0000
Cylinder (*1mm*)	14.5183	1.0665	0.0399	0.0007	0.0000	0.0001
Cylinder (*2mm*)	77.7790	20.2846	3.2924	0.3383	0.0231	0.0001
Rosette-3 (*1mm*)	0.1314	1.0962	0.0046	0.0040	0.0026	0.0012
Rosette-3 (*2mm*)	4.9425	25.2320	0.8129	0.4681	0.2946	0.1267
Rosette-4 (*1mm*)	6.8258	0.0000	0.0580	0.0000	0.0000	0.0000
Rosette-4 (*2mm*)	75.6236	0.0311	6.6508	0.0001	0.0311	0.0000
(d) $\Theta = 0°$						
Hex. Plate (*1mm*)	0.2630	0.1496	0.0001	0.0000	0.0000	0.0001
Hex. Plate (*2mm*)	0.6381	3.0087	0.1580	0.1717	0.5461	0.0003
Cylinder (*1mm*)	19.7399	1.8268	0.0894	0.0024	0.0000	0.0000
Cylinder (*2mm*)	102.0246	33.5480	7.1871	0.9838	0.0902	0.0004
Rosette-3 (*1mm*)	0.1482	1.9124	0.0113	0.0093	0.0060	0.0024
Rosette-3 (*2mm*)	7.5980	42.2109	1.2253	0.6563	0.3962	0.1889
Rosette-4 (*1mm*)	10.4234	0.0000	0.1344	0.0000	0.0001	0.0000
Rosette-4 (*2mm*)	126.4119	0.1675	18.7309	0.0000	0.1678	0.0003

Table 2.2: Azimuthal orientation averaging results, where N_{az} is the number of orientations averaged. The fractional difference is based on $N_{az} = 12$. For horizontal polarization and $\lambda = 3.16\ mm$.

Polarization VV

Crystal	$N_{az}=2$	$N_{az}=3$	$N_{az}=4$	$N_{az}=5$	$N_{az}=6$	$N_{az}=8$
(a) $\Theta = 90°$						
Hex. Plate (*1mm*)	0.0006	0.0001	0.0000	0.0000	0.0000	0.0000
Hex. Plate (*2mm*)	0.0000	0.0001	0.0009	0.0000	0.0000	0.0000
Cylinder (*1mm*)	3.1172	0.0008	0.0007	0.0004	0.0000	0.0000
Cylinder (*2mm*)	4.6825	0.0010	0.0010	0.0001	0.0005	0.0005
Rosette-3 (*1mm*)	0.0003	0.0002	0.0000	0.0001	0.0000	0.0003
Rosette-3 (*2mm*)	0.0004	0.0001	0.0000	0.0002	0.0000	0.0000
Rosette-4 (*1mm*)	0.0000	0.0000	0.0000	0.0000	0.0000	0.0000
Rosette-4 (*2mm*)	0.0004	0.0000	0.0004	0.0000	0.0000	0.0004
(b) $\Theta = 60°$						
Hex. Plate (*1mm*)	0.0505	0.0050	0.0000	0.0001	0.0000	0.0000
Hex. Plate (*2mm*)	0.2358	0.1053	0.0000	0.0001	0.0001	0.0001
Cylinder (*1mm*)	0.2712	0.0447	0.0001	0.0005	0.0005	0.0005
Cylinder (*2mm*)	3.1579	0.1694	0.0083	0.0013	0.0002	0.0001
Rosette-3 (*1mm*)	0.0821	0.0840	0.0076	0.0044	0.0027	0.0008
Rosette-3 (*2mm*)	2.3784	0.8047	0.3042	0.1746	0.1075	0.0440
Rosette-4 (*1mm*)	1.0454	0.0000	0.0011	0.0000	0.0000	0.0000
Rosette-4 (*2mm*)	3.7516	0.0000	0.0178	0.0000	0.0000	0.0000
(c) $\Theta = 30°$						
Hex. Plate (*1mm*)	0.0835	0.0194	0.0000	0.0000	0.0002	0.0000
Hex. Plate (*2mm*)	0.7327	0.2459	0.0017	0.0017	0.0004	0.0000
Cylinder (*1mm*)	1.5168	0.0332	0.0002	0.0004	0.0003	0.0002
Cylinder (*2mm*)	59.2071	10.9057	1.1719	0.0809	0.0027	0.0005
Rosette-3 (*1mm*)	0.2105	0.0780	0.0198	0.0116	0.0071	0.0027
Rosette-3 (*2mm*)	12.5159	20.9171	1.6083	0.8938	0.5475	0.2261
Rosette-4 (*1mm*)	0.5434	0.0000	0.0004	0.0000	0.0000	0.0001
Rosette-4 (*2mm*)	54.6303	0.0213	3.6776	0.0005	0.0213	0.0000
(d) $\Theta = 0°$						
Hex. Plate (*1mm*)	0.0047	0.0355	0.0009	0.0000	0.0000	0.0009
Hex. Plate (*2mm*)	2.9995	27.3941	0.4240	0.0707	1.3229	0.0000
Cylinder (*1mm*)	8.2794	0.5347	0.0202	0.0002	0.0000	0.0000
Cylinder (*2mm*)	101.9605	31.3288	5.8609	0.7028	0.0590	0.0012
Rosette-3 (*1mm*)	0.1746	0.5426	0.0215	0.0129	0.0076	0.0032
Rosette-3 (*2mm*)	10.5191	61.3371	1.5393	0.7980	0.4411	0.2098
Rosette-4 (*1mm*)	4.7846	0.0000	0.0287	0.0000	0.0001	0.0000
Rosette-4 (*2mm*)	177.8930	0.4410	40.7844	0.0000	0.4437	0.0027

Table 2.3: Azimuthal orientation averaging results, where N_{az} is the number of orientations averaged. The fractional difference is based on $N_{az} = 12$. For vertical polarization and $\lambda = 3.16\ mm$.

Wavelength	Hexagonal Plates	Cylinders	Rosette-3	Rosette-4
$\lambda = 3.16mm$	$a \leq 1000\mu m : 3$, $a > 1000\mu m : 4$	$a \leq 1000\mu m : 4$, $a > 1000\mu m : 5$	$a \leq 1000\mu m : 4$, $a > 1000\mu m : 5$	3
$\lambda = 8.66mm$	3	4	4	3

Table 2.4: Number of azimuthal angles averaged which were used for the ensemble calculations of Chapter 4. Note: 'a' is the major dimension of the ice particle.

The calculations presented above apply for highly deformed particles. It should be noted that for particles with a larger aspect ratio (defined as the ratio of the minor to major dimension) less averaging is required; this result was expected because in some sense these particles can be regarded as being more spherical. These calculations are not presented in this report as they are not directly relevant.

Chapter 3

BACKSCATTERING BY RAYLEIGH SPHEROIDS

This section examines the backscattering properties of single, non-spherical ice particles at millimeter wavelengths. Many studies of this nature have been presented in the literature however little work has been presented which can validate the assumptions commonly used in modeling non-spherical particles. Namely, the assumptions of Rayleigh scattering are often sighted but rarely demonstrated. Additionally, many of the studies were concerned with water drops which are typically larger than the ice particles of concern in this study and at much lower frequencies (e.g. X- and S-band radars). For example, water drops with an equivalent spherical diameter of approximately 2 mm have an aspect ratio of approximately 0.9 (Pruppacher and Klett, 1978) which may still be considered nearly spherical. Water droplets may reach 6-mm in diameter in rainfall with a corresponding increase in deformation. In contrast the ice particles studied herein have a maximum dimension of approximately 2 mm and aspect ratios on the order of ≤ 0.1 to 0.3.

As is evident in Section 2.1, the preferred approach by many researchers is to model the ice particles as spheroids, whose symmetry allows one to solve scattering problems efficiently while capturing the salient features of the actual particles. Over much of the frequency domain of meteorological research radars it is possible to treat cirrus particles as spheroidal Rayleigh scatterers. As technology and need increases the frequency of millimetric radars, the limits of the Rayleigh approximation will be exceeded and the backscattered signal will become increasingly sensitive to particle shape. The discrete dipole model is ideally suited to explore the assumptions inherent in Rayleigh modeling as well as issues regarding the shape of the scatterer.

In Section 3.1 of this chapter, the assumptions of the Rayleigh approximation will be given as well as the mathematical details of the Rayleigh model. The discrete dipole approximation will be used to explore two issues: what are the limitations of the Rayleigh approximation and how well do spheroidal shapes represent nonspheroidal particles? Section 3.2 will outline the nature of the calculations and the results of the calculations are given in the two succeeding sections. In Section 3.3 the results of calculations which explore the limits of Rayleigh scattering in terms of particle size and wavelength are presented. The question of how to define optical size (or size parameter) for nonspherical particles arises naturally in this context and this issue will be addressed. In Section 3.4

the backscattering of spheroidal models of ice crystals will be compared with the backscattering by more realistic forms such as hexagonal plates and columns. As the focus of the research is backscattering by cirrus ice particles at cloud radar wavelengths, appropriate ice particle sizes and wavelengths are considered. In both analyses the method is straight forward; the Mueller matrix elements for each particle are computed using the two models and are analyzed in terms of radar measurables.

3.1 THE RAYLEIGH MODEL FOR ELLIPSOIDS

The expression 'Rayleigh scattering' is often used to convey the notion of scattering by particles which are small compared to the wavelength. Scattering by spheres under this condition is proportional to $1/\lambda^4$. The expression is applied in reference to the work of Lord Rayleigh (1871). Based on historical considerations, Bohren and Huffman (1983) note that this may not be altogether the best name for scattering under these conditions as Lord Rayleigh did not consider absorbing particles. The expression is ingrained into the community at large, however, and we will follow Bohren and Huffman, imprecise though it may be, and apply the term in a general sense to imply scattering by all particles which are small compared to the wavelength.

There is one more point which must be belabored, the criteria under which Rayleigh scattering is applicable. As alluded to above, the condition most often cited in the literature is that the particles are optically small. Van de Hulst (1981) notes, however, that there are actually two criteria to be met for Rayleigh scattering:

1. The applied field must be constant across the the particle: $size \ll \lambda/2\pi$ (for a sphere; $\chi \ll 1$).

2. The internal field must remain in phase with the external field, *i.e.* the applied field should penetrate the particle thoroughly and rapidly: $\mid m \mid \cdot size \ll \lambda/2\pi$. (for a sphere; $\mid m \mid \cdot \chi \ll 1$).

The point we wish to make is that the latter condition is often over looked in the literature, yet it is not entirely insignificant. For example at $\lambda = 3.16\ mm$, $\mid m \mid \approx 1.78$ for ice. These issues will be explored at length in this chapter with the aid of the DDA.

3.1.1 Model Specifics

A Rayleigh model for oblate and prolate spheroids was developed to work within the framework of the DDA model to facilitate inter-comparisons. Van de Hulst (1981) provides the formalism from which we begin. For an incident electric field, $\mathbf{E}_o$, which has components projected onto the semi-axes of an ellipse (a, b, and c), the electric field at any point inside of the ellipse (subject to the above criteria) is given by

$$\mathbf{E} = \mathbf{E}_o - L_j \cdot 4\pi \mathbf{P} \tag{3.1}$$

where L_j is a factor which depends upon the ratio of the axes. Using the relations

$$\mathbf{P} = (m^2 - 1)\frac{\mathbf{E}}{4\pi}$$

$$\mathbf{p} = \mathbf{P}V = \alpha_j \mathbf{E}_o$$

in Equation 3.1 yields the following relation for the polarizability tensor

$$\alpha_j = \frac{V}{4\pi}\left(\frac{1}{L_j + \frac{1}{m^2-1}}\right), \qquad j = 1, 2, 3. \tag{3.2}$$

for volume V. We can use the polarizability tensor as defined by (3.2) to compute the induced dipole moment via $\mathbf{p} = \alpha_j \mathbf{E}_o$. If $\mathbf{E}_o$ is given by (2.7) then we can proceed as in Section 2.2.2 to compute the scattering amplitudes by using the dipole moment $\mathbf{p}$ in (2.9). From this point on the formalism for obtaining the desired elements of the Mueller matrix follows Section 2.2.2.

In the context of scattering all of the geometrical information of the particle is determined by L_j and its optical properties are specified by the complex refractive index m. We note that ellipsoids reduce to spheroids for $c = b$ which implies that $L_2 = L_3$ (we also observe that $L_1 = L_2 = L_3 = \frac{1}{3}$ for spheres). Because $L_1 + L_2 + L_3 = 1$, we only need to specify L_1 as is given in van de Hulst (1981, p.71). For prolate spheroids ($a > b$):

$$L_1 = \frac{1-e^2}{e^2}\left(\frac{1}{2e}\ln\left(\frac{1+e}{1-e}\right) - 1\right), \qquad e^2 = 1 - \frac{b^2}{a^2}$$

And for oblate spheroids ($a < b$):

$$L_1 = \frac{1+f^2}{f^2}\left(-1 - \frac{1}{f}\arctan(f)\right), \qquad f^2 = \frac{b^2}{a^2} - 1.$$

The model was validated by comparisons with DDA spheroids and with a similar Rayleigh model of Sergey Matrosov (personal communication, 1993).

3.2 ABOUT THE CALCULATIONS

The discrete dipole approximation (DDA) is ideally suited to serve as a standard for comparison with spheroidal models. It allows one to compute the scattering of polarized electromagnetic radiation by an arbitrarily shaped dielectric particle of virtually any optical size to a specified accuracy, although in practice one is limited by the computational resources at hand. The DDA and Rayleigh models have been outlined in detail above. The dielectric particles are modeled to represent ice particles characteristic of cirrus clouds. Below we briefly outline the characteristics of the particles. Justification for the assumptions regarding the cirrus particles modeled in this section is given in Section 4.1.

$\lambda\ (mm)$	m
1.40	$1.781 - i0.0048$
3.16	$1.782 - i0.0028$
8.66	$1.783 - i0.0014$
22.21	$1.783 - i0.0007$

Table 3.1: Wavelengths (λ) and complex refractive indices (m) used in the single particle scattering calculations.

For the purposes of this analysis, we considered hexagonal plates and columns with major dimensions of 50, 200, 600, 1000, 1400, and 2000 μm as being representative of the class of particles found in cirrus. The aspect ratios of the particles, defined here to be the ratio of the minor dimension to the major dimension, were determined from the work of Auer and Veal (1970). The columnar crystals were relatively straight forward to model with the DDA, however, the plates posed a bit of a problem. In general, the aspect ratios determined by Auer and Veal are significantly less than 0.1 for plate-like crystals. For such particles choosing a sufficient number of dipoles to represent the vertical structure of the particle yielded an enormous number of dipoles in the horizontal dimensions. Thus, for purposes of numerical expediency, the aspect ratios of plate-like particles with major dimensions greater than 200 μm were set to 0.1. For each spheroid, the dipole spacing was chosen such that exactly six dipoles fit across the minor dimension. The dimensions of the corresponding oblate and prolate spheroids were determined by preserving volume and aspect ratio with its hexagonal counterpart. In all cases the ice particles were assumed to be randomly oriented with their major dimension in the horizontal plane. To achieve a sense of random orientation the particles were averaged over three azimuthal angles. This was slightly less than ideal as was discussed in Section 2.3, however, the analysis will accommodate this fact. The wavelengths (λ), together with the respective complex refractive indices (m), were chosen to reflect current operating radars and are presented in Table 3.1.

3.3 LIMITATIONS OF THE RAYLEIGH MODEL

As was discussed above there are really two criteria which must be considered in the application of the Rayleigh approximation. The first condition is that the applied field must be nearly constant across the particle. The second condition states that the incident field should rapidly penetrate the particle, such that the internal field remains in phase with the incident field. Since $\mid m \mid \approx 1.78$ for ice, the latter condition was not too restrictive and we focussed on the first stipulation. We can express this condition in terms of the optical size (or size parameter) which is defined as $\chi = 2\pi R/\lambda$ for a sphere of radius R.

For nonspherical particles it is common to define $\chi = 2\pi R_e/\lambda$ where R_e is the radius of a sphere possessing a volume equal to the original particle. To determine the validity of the Rayleigh approximation we defined the quantity

$$\Delta F_{i,s} = 100 \cdot \left(|f_{i,s}|^2_{Ray.} - |f_{i,s}|^2_{DDA} \right) / |f_{i,s}|^2_{Ray.} \quad [\%]$$

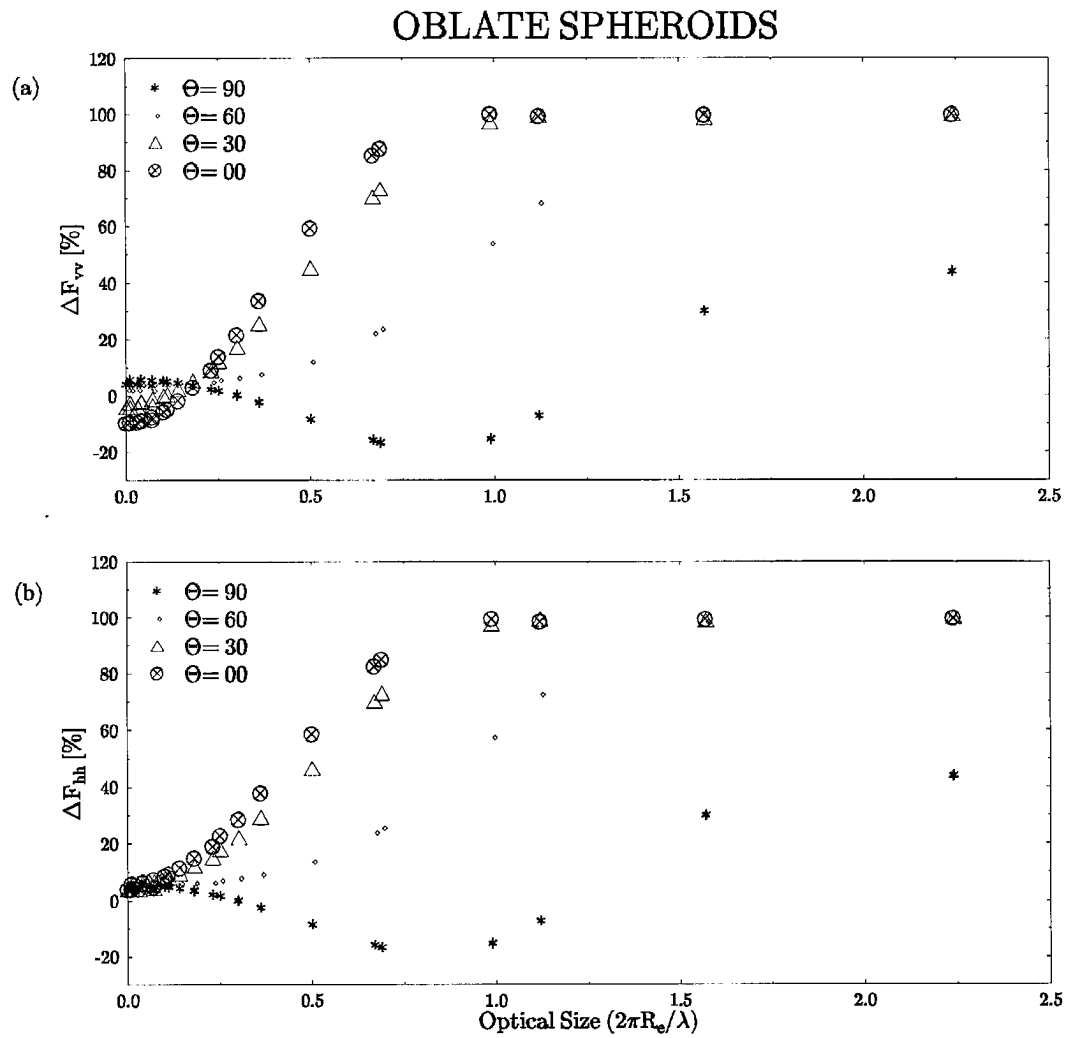

Figure 3.1: The fractional difference [%] of the backscattering amplitudes between the Rayleigh and DDA models for oblate spheroids.

where $f_{i,s}$ is an element of the backscattering amplitude matrix in Equation 2.8 with incident polarization 'i' and scattered polarization 's'. Each element of the backscattering amplitude matrix describes how a given particle scatters the incident radiation. Figure 3.1 presents the backscattering amplitude differences for oblate spheroids and vertical (ΔF_{vv}) and horizontal (ΔF_{hh}) polarizations as a function of optical size. The cross polarization terms (ΔF_{vh}) were negligible which was to be expected from oriented, plate-like ice particles. The analogous plots for prolate spheroids are presented in Figure 3.2. The radar elevation angle is denoted by θ.

Figure 3.1 will be analyzed first because the features are more clearly defined than in Figure 3.2. Comparing Figure 3.1(a) with Figure 3.1(b) it is evident that the fractional difference between the two models is virtually independent of polarization. This is good because it indicates a consistency between the two models with respect to polarization.

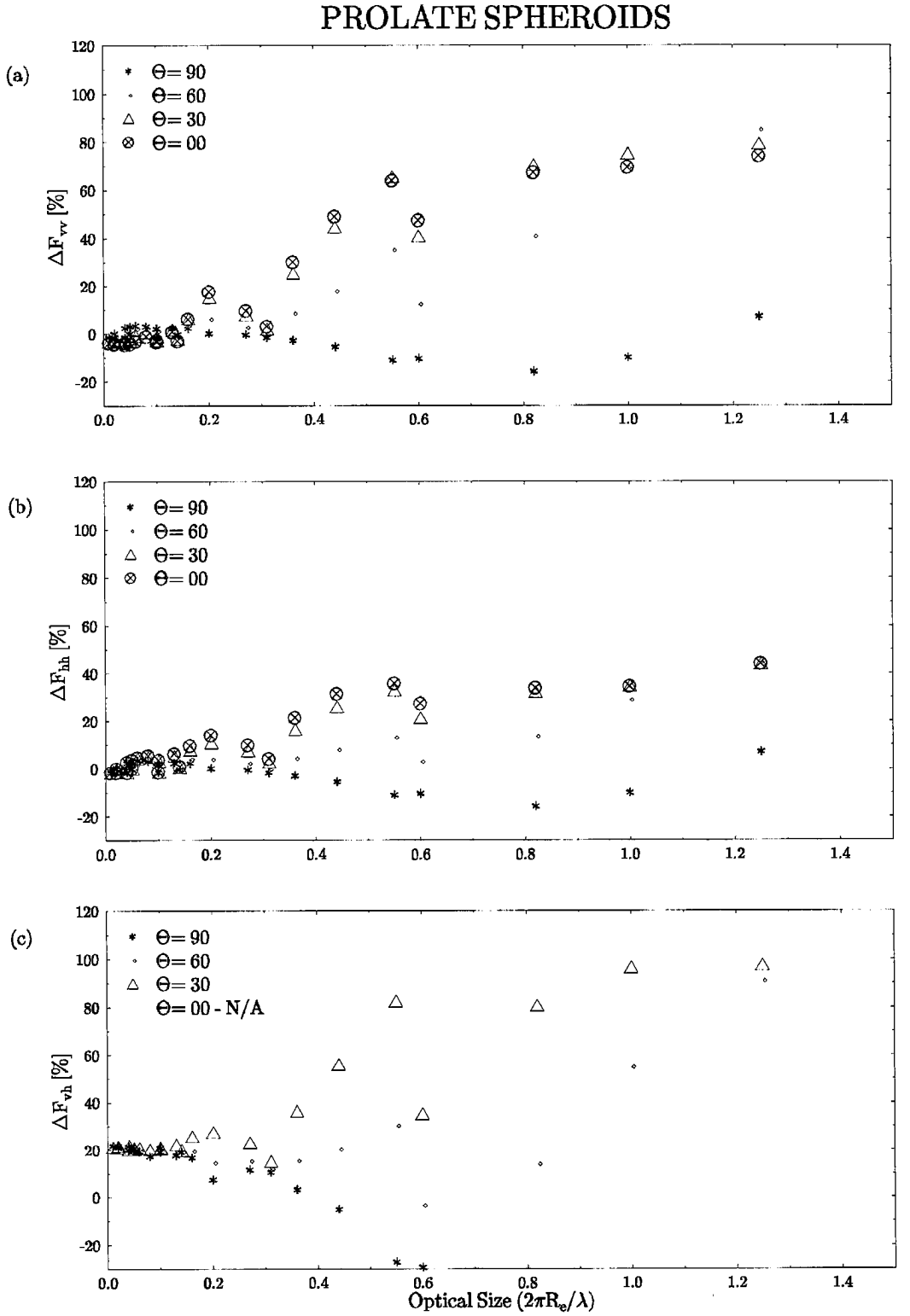

Figure 3.2: Same as Figure 3.1 except for Prolate spheroids.

The exception to this is for small θ (edge on incidence) at vertical polarization (Figure 3.1(b)). Bear in mind that these oblate spheroids were very thin. Also note the asymptotic behavior; as the optical size becomes large $|f|^2_{DDA}/|f|^2_{Ray.} \rightarrow 0$, which is indicative of the power law behavior of the backscattered energy by Rayleigh particles. It is important to observe that the differences between the two models (ΔF) becomes very large for $\chi \ll 1$ and appears to be strongly dependent upon the radar elevation. This indicates that χ, as based on the radius of an equal volume sphere, is somewhat ambiguous. We will examine this issue in the following section. The backscattering amplitude differences for prolate spheroids (Figure 3.2) are less clear than the corresponding plots for prolate spheroids largely because the optical sizes tend to be cluttered towards smaller values. There is also a general agreement between the vertical and horizontal plots for the prolate spheroids; one would expect the difference to be the same for each polarization as noted above. The asymptotic behavior is also evident although less pronounced and at lower values. There is a considerable difference in the cross term for prolate spheroids. The difference, ΔF_{vh}, is zero for edge on incidence but is quite large for other elevations.

Qualitatively we observe an abrupt change of the slope in the difference curves of Figures 3.1 and 3.2, especially for the oblate spheroid case. There is also a significant difference between elevations, with the lower radar elevations breaking down at smaller major dimensions. It is also evident that oblate spheroids are more sensitive than prolate spheroids. To be more quantitative we chose the criteria for breakdown to be $\Delta F_{i,s} = 12 - 15\%$. This value was not entirely arbitrary as it was based on the following rationale:

- For optically small particles (*i.e.* $\chi \leq 0.1$) there is approximately $\pm 10\%$ difference between the Rayleigh and DDA models.

- Spheroids modelled by the discrete dipole approximation will possess many "edge" dipoles which must have their dielectric functions reduced according to the Lorentz-Lorenz mixing rule, which introduces some error.

- The DDA is only approximate - the iterations were stopped at an accuracy of 1×10^{-4}.

We are now in a position to ascertain the point at which the Rayleigh model breaks down. The results, interpolated from the graphs in Figures 3.1 and 3.2 are summarized in Table 3.2. As was discussed in Section 2.2.3 backscattering represents the most severe test for any scattering theory. Thus we can be confident that our conclusions are valid for other scattering angles.

Oblate Spheroids				
Radar Elevation	$\lambda = 1mm$	$\lambda = 3mm$	$\lambda = 8mm$	$\lambda = 22mm$
$\theta = 00, 30$	$200\mu m$	$600\mu m$	$1400\mu m$	$> 2000\mu m$
$\theta = 60, 90$	$400\mu m$	$1200\mu m$	$> 2000\mu m$	$> 2000\mu m$
Prolate Spheroids				
$\theta = 00, 30$	$300\mu m$	$800\mu m$	$2000\mu m$	$> 2000\mu m$
$\theta = 60, 90$	$600\mu m$	$1200\mu m$	$> 2000\mu m$	$> 2000\mu m$

Table 3.2: Limits of the Rayleigh approximation based on Rayleigh-DDA model differences and a maximum allowable error of 12-15%.

3.3.1 On the Notion of Optical Size

The concept of 'size parameter' (χ, sometimes it is also called the 'size factor') is used to convey a notion of how large a particle is relative to the wavelength of some incident radiation. In a sense it is an 'optical size' which is perhaps a better term as it better represents the concept. Subsequently, this expression will be used throughout the remainder of this document.

Holt (1982) observes that the concept of optical size is somewhat ambiguous for nonspherical particles. For nonspherical particles the optical size can be defined as $\chi = 2\pi R_{eff}/\lambda$, where R_{eff} is some measure of the particles size; an effective radius. The ambiguity arises in the definition of R_{eff}. In the scattering literature, the most common definition is the radius of an equal volume sphere (call it R_e). One also finds $R_{eff} = a$ or $R_{eff} = a/2$ where a is the major dimension of the nonspherical particle. Indeed this ambiguity is born out in the graphs of the previous section. For example, note the variation with elevation angle in Figures 3.1 and 3.2 where the fractional differences in backscattered amplitude were plotted as a function of $\chi = 2\pi R_e/\lambda$. For a given optical size the fractional difference between the Rayleigh model and the DDA model is strongly dependent on the elevation angle.

We shall attempt to shed some light on this issue with the results from the previous section. In Section 3.1, note that the first condition cited for the application of the Rayleigh approximation is that $size \ll \lambda/2\pi$. Which is simply $\chi = 2\pi R_{eff}/\lambda \ll 1$. For ice spheres it has been shown that the Rayleigh approximation begins to break down at $\chi \approx 0.3$. Thus one would expect to see nonspherical Rayleigh ice particles to deviate from their equivalent DDA counterparts for optical sizes of approximately 0.3 (e.g. Matrosov, 1992). Plots were made with the same data as in the previous section, but this time four different definitions of the optical size were used: $\chi = 2\pi R_e/\lambda$ (case 1), $\chi = 2\pi a/\lambda$ (case 2), $\chi = \pi a/\lambda$ (case 3), and $\chi = \pi a/\lambda(1 + cos(\Theta))$ (case 4). The plots are presented in Figures 3.3 and 3.4 for oblate spheroids and 3.5 and 3.6 for prolate spheroids. Based on the argument just given it is evident from these figures that the definition based on the radius of equal volume spheres is most appropriate. For all elevations and both polarizations, the fractional difference (error in Rayleigh model) in case 1, begins to grow rapidly for optical sizes significantly less than 0.5. In contrast, none of the other three definitions exhibit

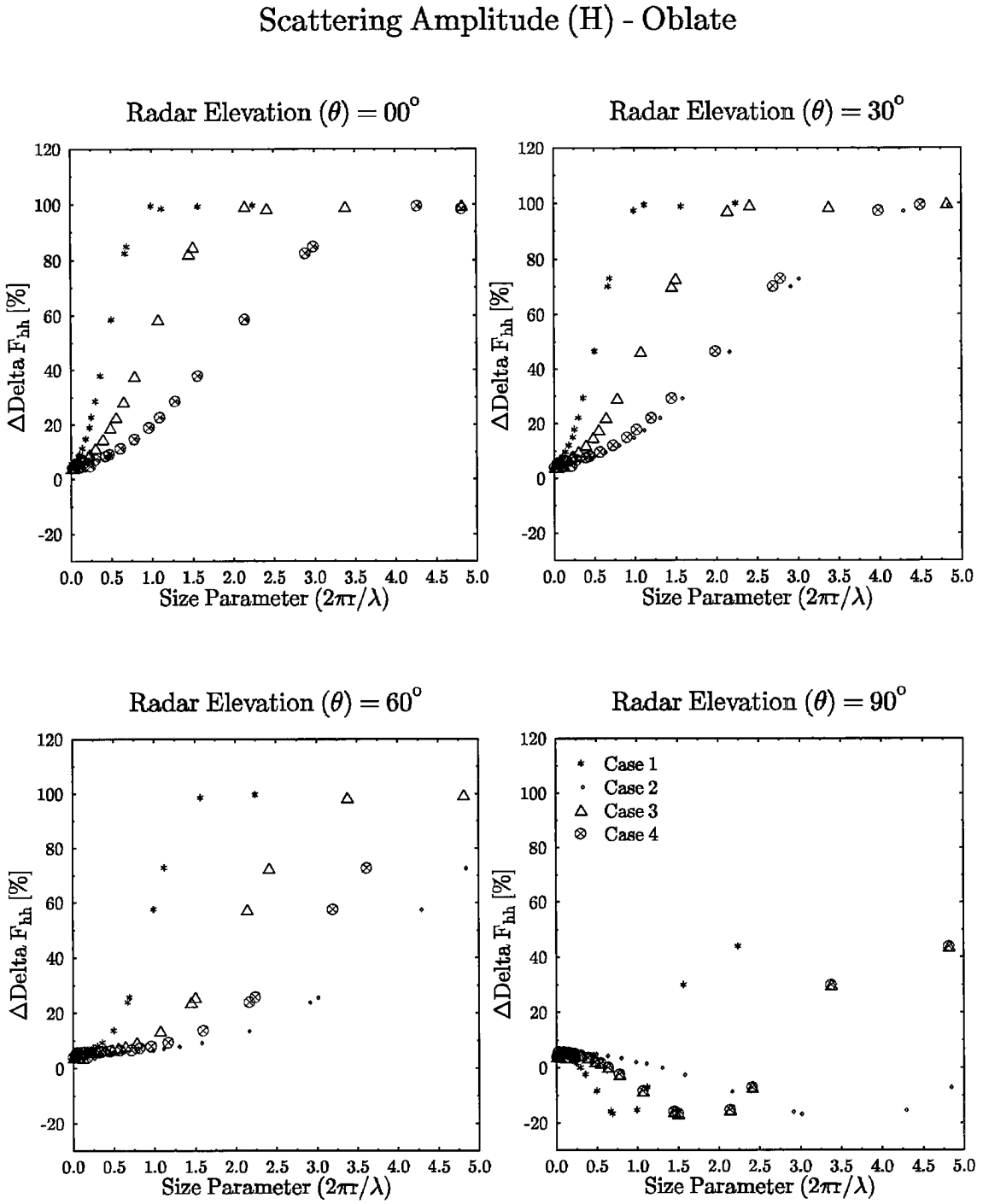

Figure 3.3: The fractional difference of the backscattering amplitudes between the Rayleigh and DDA models for oblate spheroids and for various definitions of the optical size (see text). Horizontal polarization.

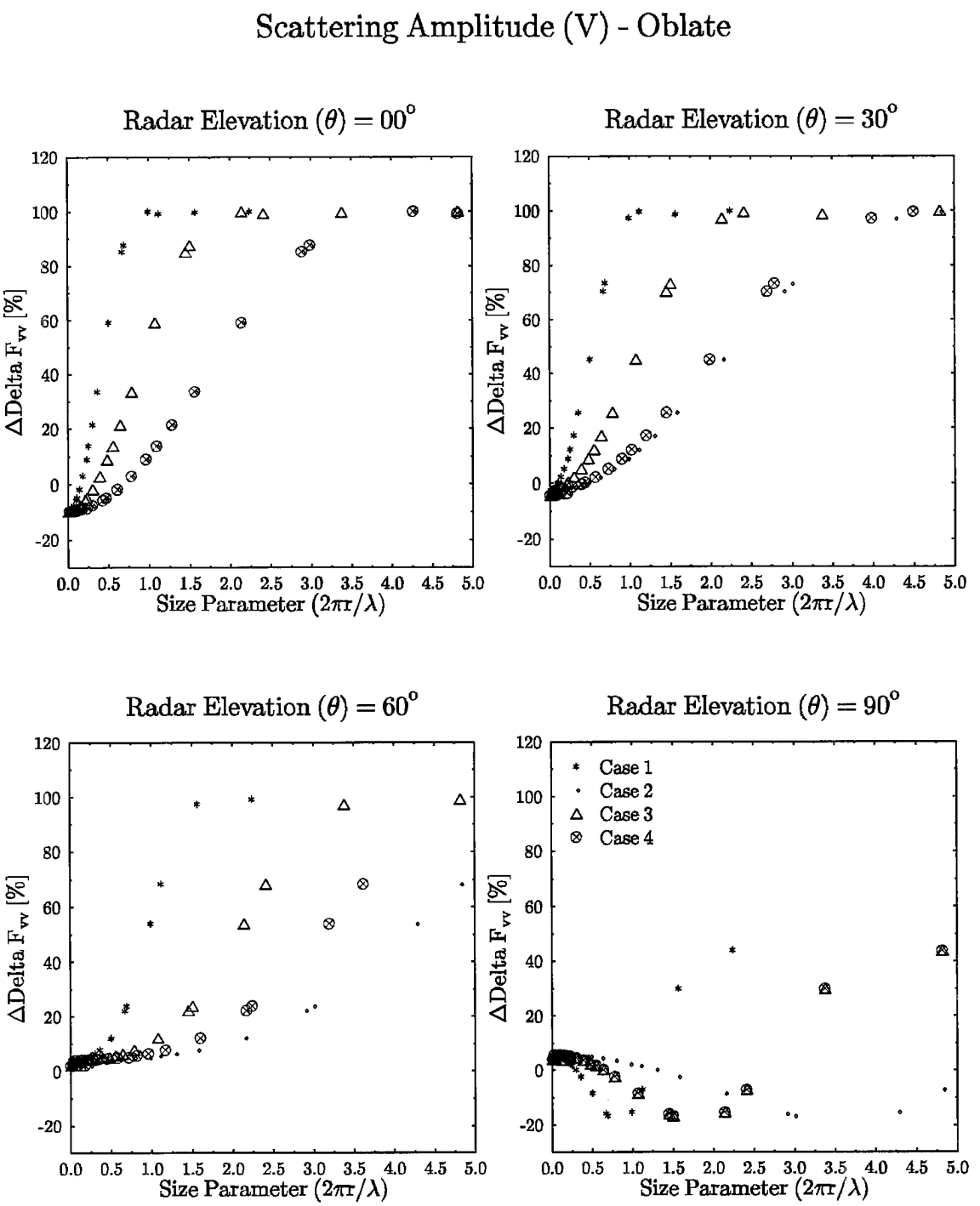

Figure 3.4: Same as Figure 3.3 except for vertical polarization.

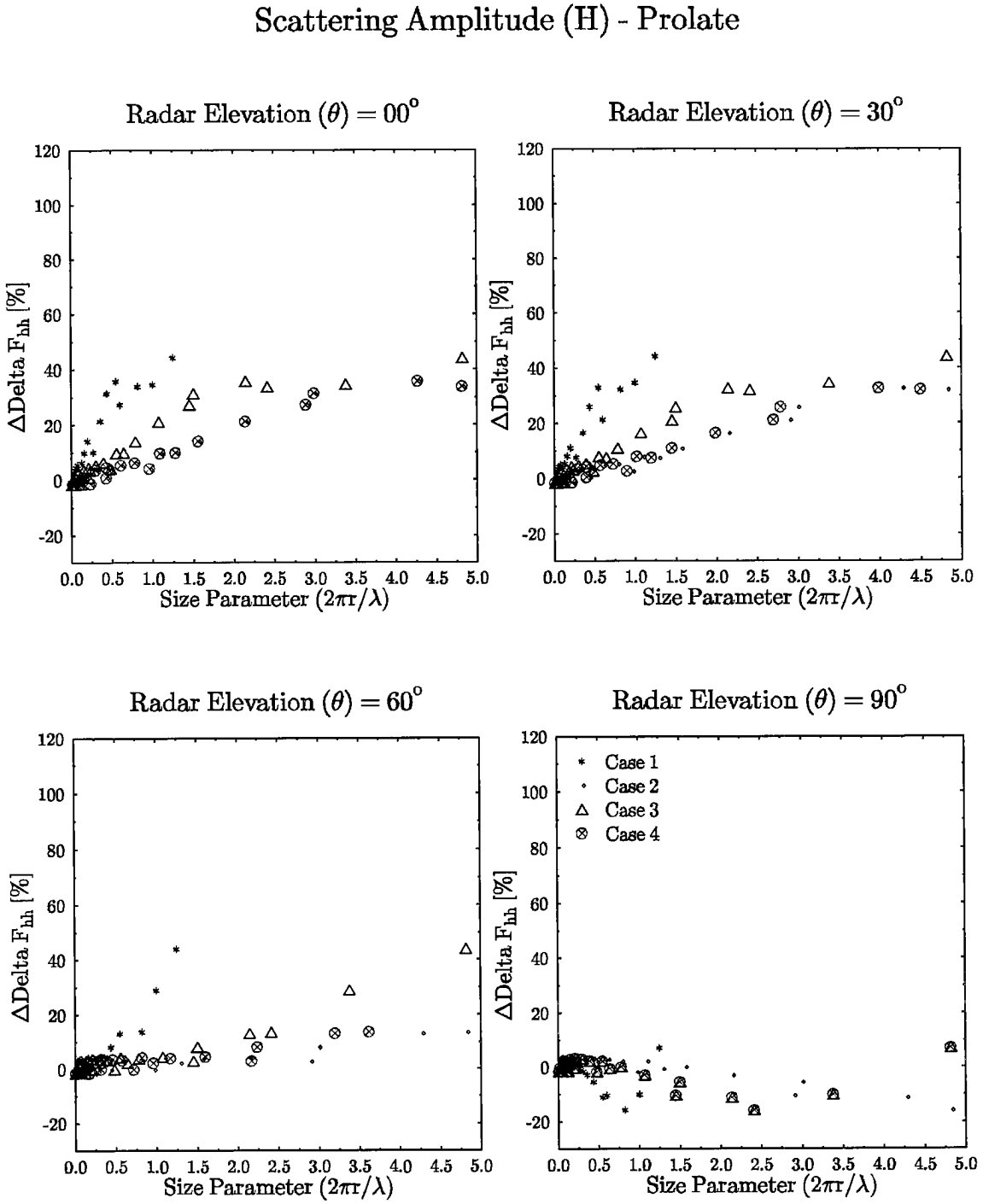

Figure 3.5: The fractional difference of the backscattering amplitudes between the Rayleigh and DDA models for prolate spheroids and for various definitions of the optical size (see text). Horizontal polarization.

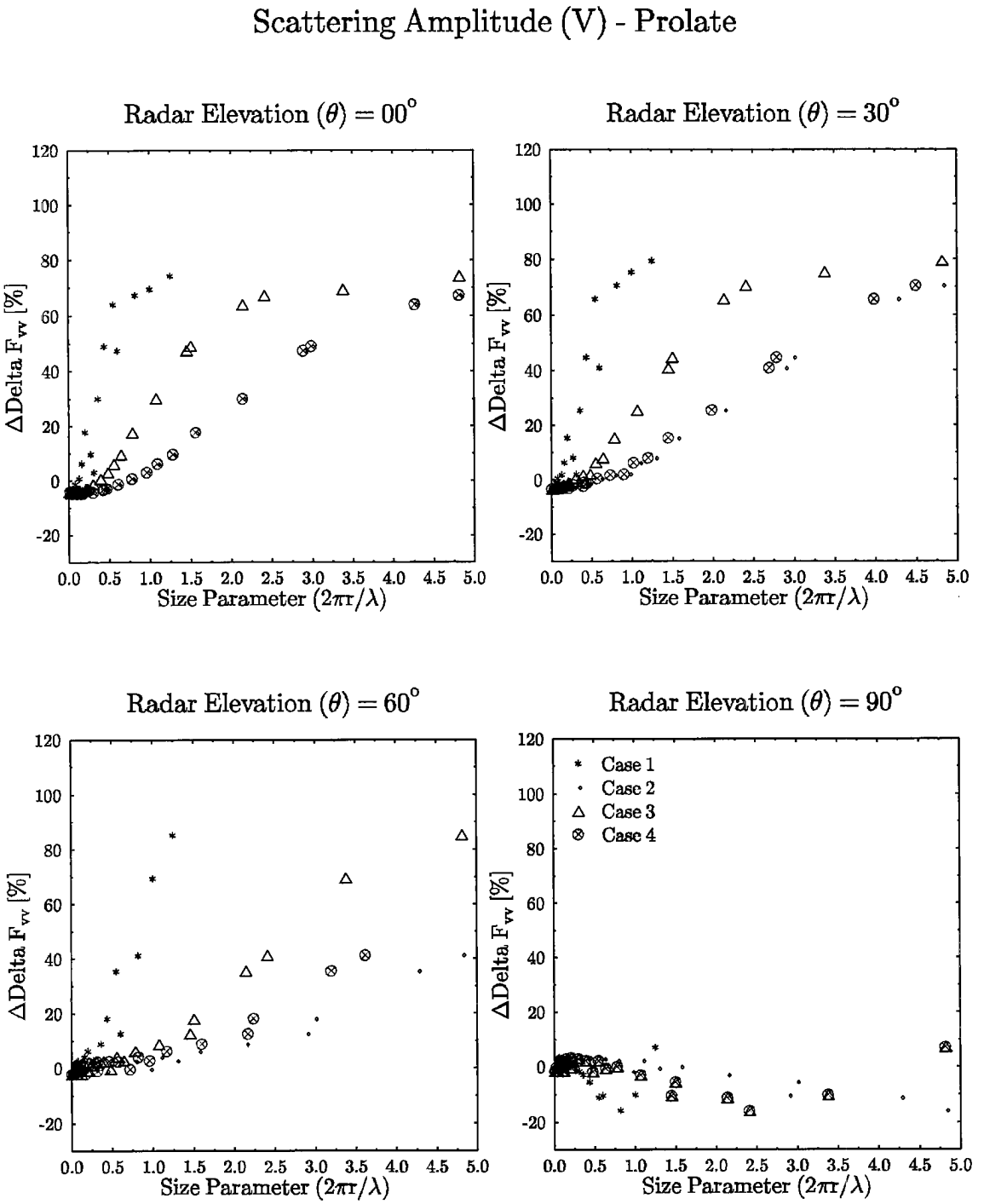

Figure 3.6: Same as Figure 3.5 except for vertical polarization.

this behavior. Attempts to account for the variability caused by the elevation dependence were unsuccessful as is exemplified by case 4.

3.4 VALIDITY OF SPHEROIDAL SHAPES

As is documented in Section 2.1, virtually all of the efforts to model scattering by nonspherical hydrometeors have employed the oblate and prolate spheroids. Although the variability in shape and size of naturally occurring hydrometeors is quite high, they generally possess a six sided structure. Excluding hail and aggregates of snowflakes, naturally occurring ice particles can be characterized as being variations of hexagonal plates and columns. Such particles are found in cirriform clouds (refer to Section 4.1). Thus it is natural to ask the question, 'How well do spheroidal particles represent actual particles with respect to the scattering of electromagnetic radiation?'.

To address this issue we will proceed in a fashion analogous to the previous section. We define the fractional difference in the backscattering amplitudes as

$$\Delta F_{i,s} = 100 \cdot \left(|f_{i,s}|^2_{Hex} - |f_{i,s}|^2_{Sph} \right) / |f_{i,s}|^2_{Hex} \quad [\%],$$

where the subscript Hex denotes hexagonal particles (plates or columns) and the subscript Sph indicates spheroidal particles of equal volume and aspect ratio (oblate or prolate). As before i, s indicate the polarization of the incident and scattered waves. The scattering properties of both the hexagonal and spheroidal particles were computed with DDA. For this analysis $\lambda = 22\ mm$ has been omitted. As before, any fractional difference less than 15% will be deemed acceptable. In each of the following figures, the fractional difference is presented as a function of the major dimension and for several elevations ($\theta = 0^o, 30^o, 60^o, 90^o$).

The results for columnar crystals are presented in Figures 3.7-3.9 (horizontal, vertical and cross polarizations respectively). For horizontal and vertical polarizations the fractional differences are mostly within the acceptable criteria with the exceptions being discussed below. The fractional differences between hexagonal columns and prolate spheroids are more sensitive at vertical polarization. On the basis of vertical polarization we observe significant differences for $a \geq 600\ \mu m$ at $\lambda = 1.4\ mm$ and for $a \geq 1000\ \mu m$ at $\lambda = 3.16\ mm$. These values are for the lower elevation angles and can be relaxed a bit for higher elevation angles. For the cross polarization case all wavelengths are very sensitive for small particles, and most sensitive to the shorter wavelengths for the larger particles, which suggests that the Linear depolarization ratio (LDR) should be very sensitive to shape for all sizes and wavelengths.

The ability of spheroids to represent hexagonal plates is presented in Figures 3.10 and 3.11. There is a very strong signature for elevation, with the lowest elevations being most sensitive to shape. For $\lambda = 1.4\ mm$ particles with major dimensions greater than

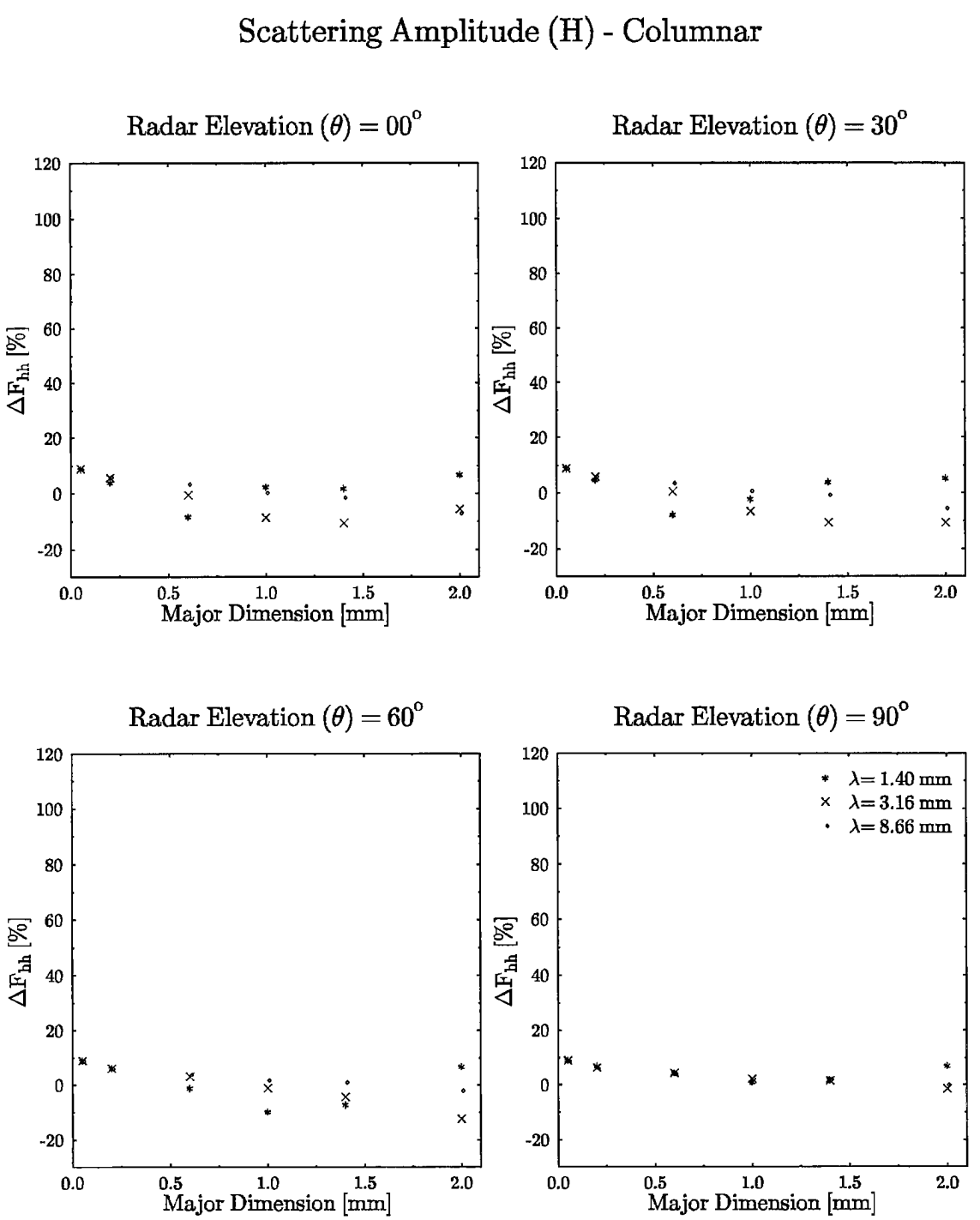

Figure 3.7: The fractional difference between hexagonal columns and prolate spheroids as computed by the DDA model. Horizontal polarization.

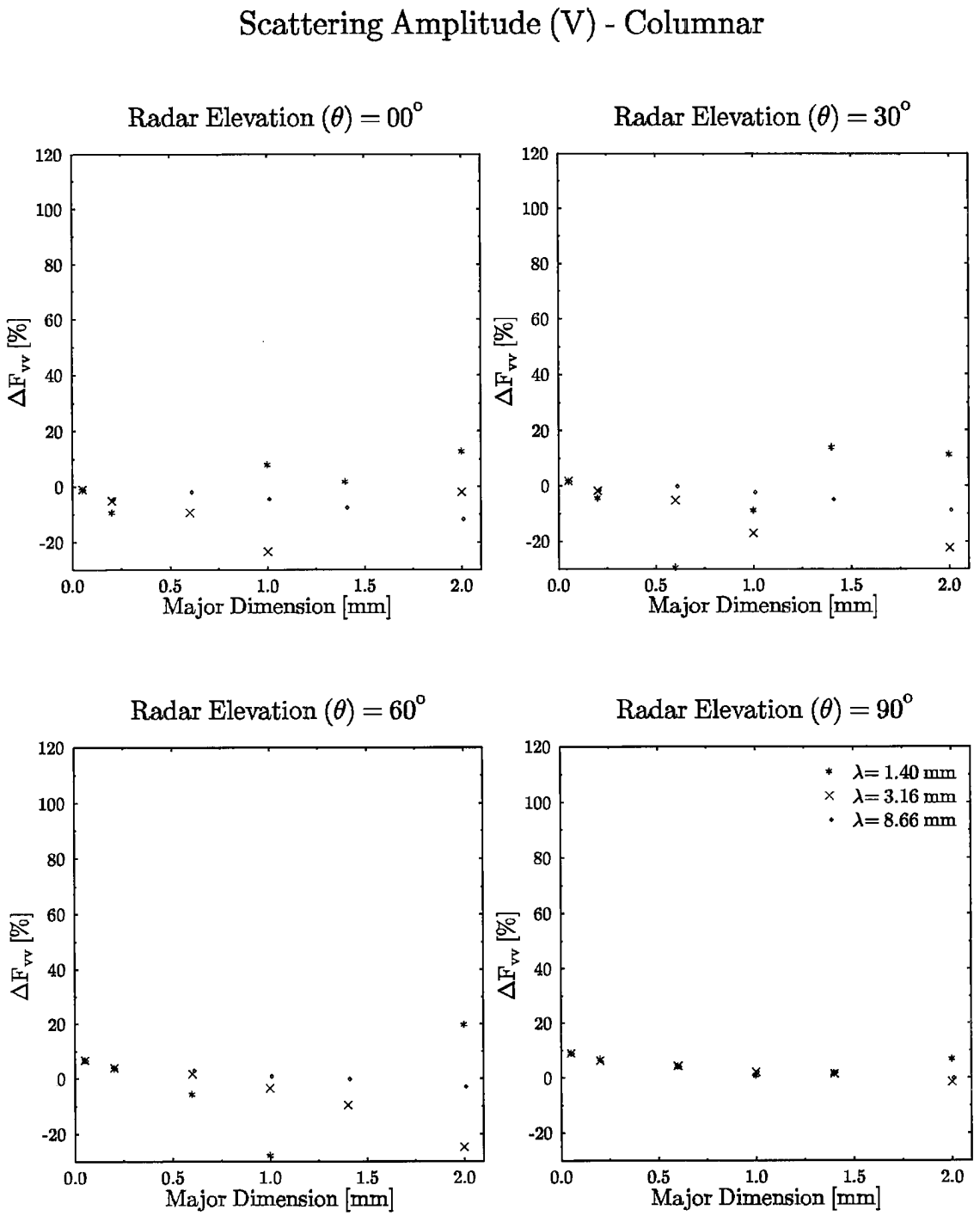

Figure 3.8: Same as Figure 3.7 except for vertical polarization.

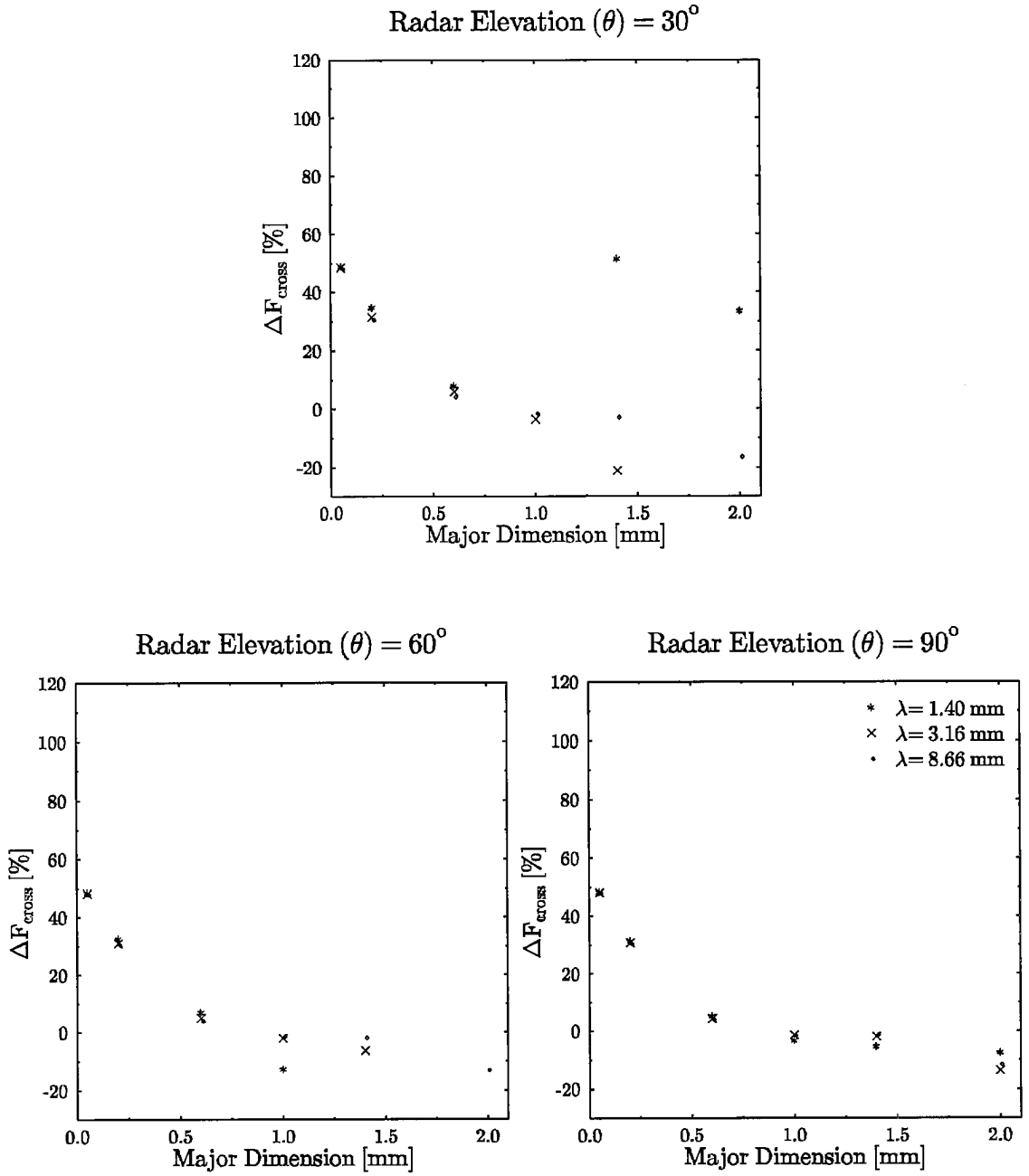

Figure 3.9: Same as Figure 3.7 except for cross polarization.

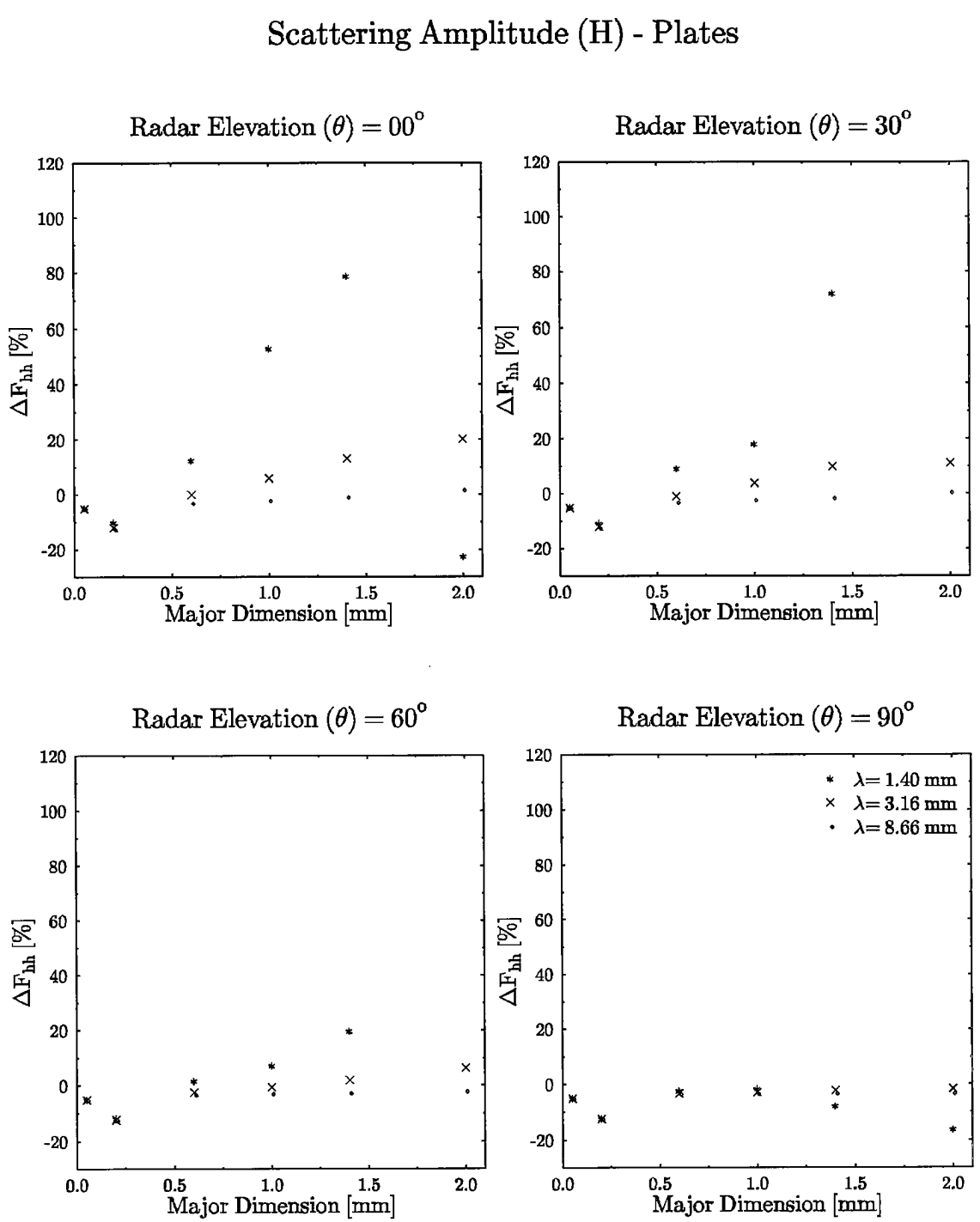

Figure 3.10: The fractional difference between hexagonal plates and oblate spheroids as computed by the DDA model. Horizontal polarization.

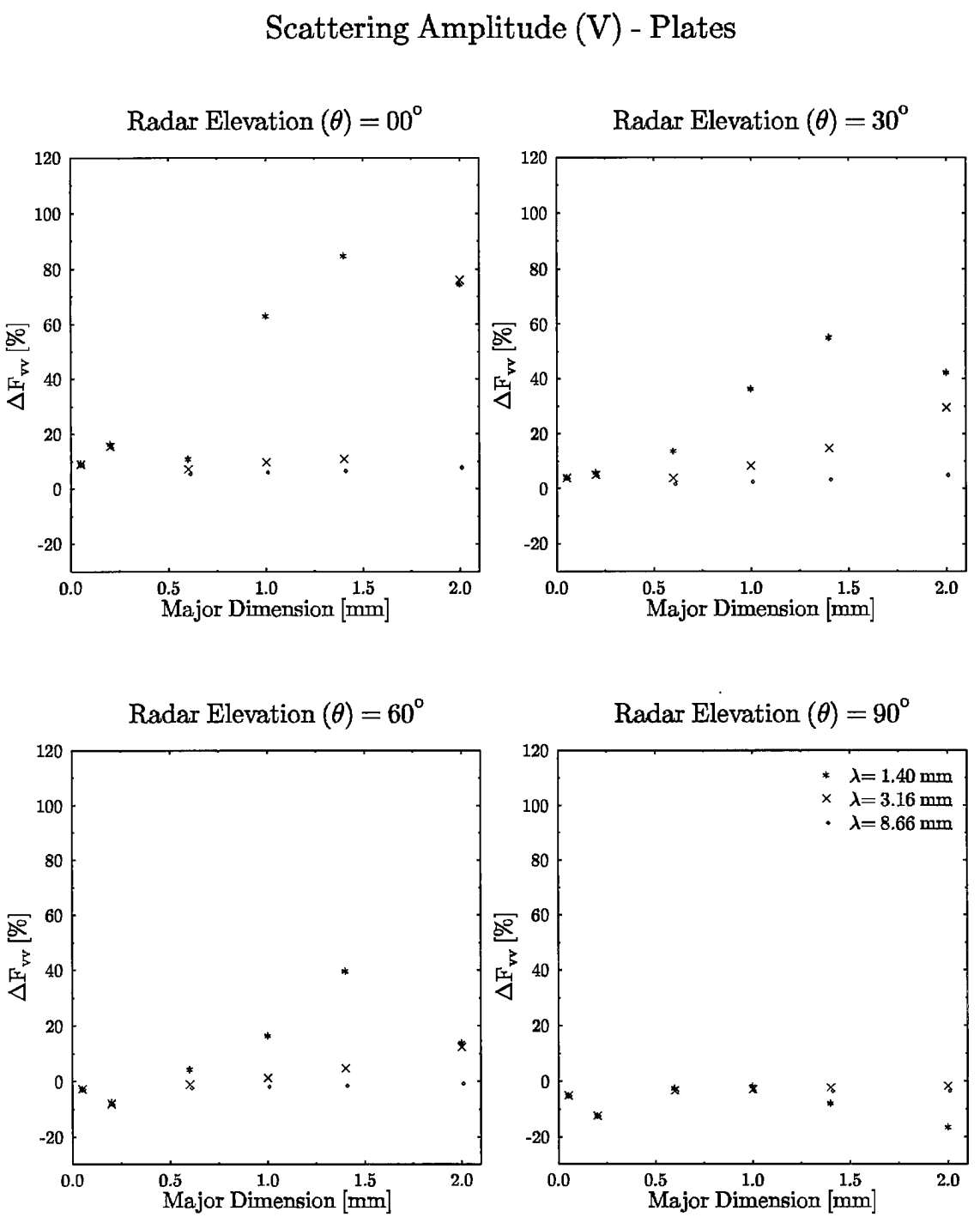

Figure 3.11: Same as figure 3.10 except for vertical polarization.

approximately 800 μm are highly sensitive to shape. At $\lambda = 3.16$ mm only particles ≥ 1500 μm become sensitive to shape.

For both oblate and prolate spheroids the results are the same for both polarizations at vertical incidence ($\theta = 90^o$) as expected. At wavelengths near or beyond 8.7 mm, the differences in shape between hexagonal and spheroidal particles are insignificant for both vertically and horizontally polarized waves.

These results are significant because it means that, with caution, spheroids can be exploited as a theory to study the interaction of millimetric ($\lambda \geq 3.16$ mm) polarized radiation by cirrus particles. Given that the uncertainties in measured (*in situ*) microphysical quantities are quite large and that the upper bound on cirrus particles can be taken to be ≈ 2 mm (see section 4.1), the application of spheroidal models to scattering by cirrus particles (e.g. Matrosov, 1991) at 3.16 mm and 8.66 mm is justifiable. We add the caveat that one must take care when applying the Rayleigh model, as the results become suspect for the larger cirrus particles.

Chapter 4

BACKSCATTERING BY ENSEMBLES OF ICE PARTICLES

The global distribution of ice mass in the form of cirrus clouds is an important component of the climate system. One means of quantifying the spatial and temporal distribution of cirriform clouds is through the ice water content (IWC). The IWC of cirriform clouds is an important parameter in both cloud models and in the modelling of the radiative transfer through such clouds. Thus, the ability to remotely measure the bulk microphysical properties of cirriform clouds is of seminal importance to our understanding of the hydrologic and radiative nature of cirrus. Cloud radars are well suited to the measurement of IWC and other properties of cirriform clouds such as shape and orientation because of their sensitivity to small particles and their potentially high resolution. This chapter will examine the connection between the IWC of cirrus and millimetric radar observables. Focus was given to the wavelengths of 3 and 8 mm because of recent and impending applications at these wavelengths. All calculations were done at the radar elevation angles of: $\Theta = 0°$, $30°$, $60°$, $90°$.

An overview of the relevant characteristics of cirrus clouds is the subject of Section 4.1. In Section 4.2, the sensitivity of radar reflectivity to the parameters of the particle size distribution is explored. Theoretical ice water content-radar reflectivity relations ($IWC - Z_e$), along with comparisons to available empirically determined relations, are focussed on in Section 4.3.

4.1 PROPERTIES OF CIRRUS CLOUDS

This section details the relevant microphysics of ice crystals found in cirrus clouds. Relevance was defined by the special needs of this study of backscattering by cirrus particles. Issues such as nucleation mechanisms and rates are not of primary of interest, whereas issues such as number concentrations and morphology are. The microphysics covered is but a subset of the vast and interesting field of study of atmospheric ice particles. For the purposes of this work microphysics was defined as those characteristics of the individual hydrometeors which were required to model their scattering properties. We were interested in ice particle habit, size, aspect ratio, orientation (hydrodynamics), size distribution, ice water content (IWC), and optical properties (the complex refractive index). Although this definition is somewhat unconventional it is appropriate for this study. We also note that the precise definition of what constitutes a cirrus cloud is still somewhat ambiguous. We have adopted the working definition:

Nonprecipitating ice clouds residing at high levels.

Where we should be careful to note that nonprecipitating means clouds which are not precipitating at the ground. It should be pointed out that this definition is subtly different than the definition proposed by the World Meteorological Organization (1969):

Layer, hook, and band or filament clouds composed principally of ice crystals.

The conditions under which most clouds exist make them difficult to measure *in situ*. This is especially true for cirrus clouds. It has been observed that the microphysical properties can vary significantly from cloud to cloud and even spatially and temporally within a single cloud. Furthermore, the optical properties of the clouds can vary dramatically for slight changes in microphysical parameters. It can be concluded that the microphysical properties of high-level ice clouds are the least known and most uncertain aspect of this study. The work must continue, however. In the following sections the properties will be described as they are best understood today.

4.1.1 The Physical Properties of Cirrus Clouds

To model scattering by ice crystals we must specify the morphology, size and aspect ratio of each particle. We must also be concerned with the effects of hydrodynamics on particle orientation and the temperature dependent complex refractive index of ice. The number concentration of ice crystals in cirriform clouds is a complex issue; special consideration is given to the specification of the particle size distribution in Section 4.1.2. Two recent reviews (Liou, 1986; Dowling and Radke, 1990) provide a well rounded picture of cirrus clouds and form the basis from which this work proceeded. Another perspective of cirrus clouds is presented in Kosarev and Mazin (1991). The reader may also wish to consult Pruppacher and Klett (1978) for a comprehensive discussion of the microphysics of ice particles. It should be stressed how difficult it to make *in situ* measurements of ice crystals. To date, methods of detecting ice crystals smaller than approximately 100 μm from fast flying aircraft are highly suspect, and the interpretation of 2-D images and images from replicator devices, with respect to shape, is difficult.

Ice crystal habit is a function of the available vapor gradient and temperature. Habits tend to be hexagonal in nature and either of plate-like or columnar varieties. These shapes have been categorized by Magono and Lee (1966) and we have adopted their nomenclature. Dowling and Radke (1990) report the following habits as being typical, columns (C1e), bullets (C1c), rosettes (C2a), and plates (P1a). They note, however, that the literature is not yet extensive enough for this list to be definitive or to offer relative abundances. Hollow columns (C1f), bundled columns (N1d), and irregular crystals have also been observed (e.g. Heymsfield and Platt, 1984; Liou, 1986).

Cirrus particle sizes are often characterized by their major dimension. Reported values of the major dimension range from 1 μm to 8000 μm, however, these values are

extreme and a more reasonable range would be 10 μm to 2000 μm. Based on mass-weighted estimates, Dowling and Radke (1990) report a typical size of 250 μm. In general the aspect ratio varies with ice crystal size. We define the aspect ratio to be the ratio of the minor dimension (b) to the major dimension (a), therefore: $0.0 < \frac{b}{a} \leq 1.0$. The relation between the major and minor dimension has been parameterized empirically by Auer and Veal (1970) (a and b in μm):

$$P1a \quad \begin{cases} b = 2.020a^{0.449} & a \leq 200\mu m \\ b = 0.1a & a > 200\mu m \end{cases} \tag{4.1}$$

$$C1e, C1f \quad \begin{cases} b = -8.479 + 1.002a - 0.00234a^2 & a \leq 200\mu m \\ b = 11.3a^{0.414} & a > 200\mu m \end{cases} \tag{4.2}$$

$$C2a \quad \{ \; b = 0.16a. \tag{4.3}$$

It should be emphasized that the relation $b = 2.020a^{0.449}$ for plates (P1a) is generally valid for all 'a'. Because the number of dipoles becomes too great for large, very flat plates, we were forced to model plates larger than 200 μm with an aspect ratio of 0.1. This is an artifact of how the dipole size was chosen. The general practice was to fix the number of dipoles across the minor dimension and allow the dipole spacing to vary which ensured consistency from particle to particle. Although spatial rosettes were not modelled, planar rosettes were in an attempt to capture some of the irregular features of rosettes. The aspect ratio of the individual spines on the planar rosettes were set to 0.16 based on numerical constraints and estimates from images of ice crystals captured on replicator slides. This aspect ratio is not entirely realistic because of the crude means of obtaining it and because it ignores variation with overall size. The photographs of the replicator slides were provided by Nancy Knight (personal communication, 1993) and were taken on flights through cirrus during the First International Satellite and Cloud Climatology Field Experiment (FIRE II) near Coffeeville Kansas. We also modeled hexagonal columns, hollow columns, and hexagonal plates. For an ensemble of hexagonal columns we expect the faces and edges to be randomly oriented. Consequently hexagonal columns were treated as cylinders with an equal volume and aspect ratio.

The IWC can be measured directly from impaction devices or inferred from measured ice crystal size distributions with assumptions relating the particle dimension to its mass. Values of IWC have been reported in the range of 0.0001 gm^{-3} to 3.0 gm^{-3}. According to Dowling and Radke (1990) a typical value might be considered to be 0.025 gm^{-3}. These properties (shape, size and IWC) are summarized in Table 4.1. The typical values are reported with an error factor of ± 2.

Through observations in clouds and laboratories, theoretical calculations, and measurements with lidars (Liou, 1986; Sassen, 1980) it has been concluded that cirrus particles tend to fall with their major dimension oriented horizontally in a quiescent environment. That is to say the major axis of the ice crystal is normal to the vertical

	HABIT:	MAJOR DIMENSION [μm]:	IWC [gm^{-3}]:
Range:	planar, columnar, spatial, irregular	(1) $20 \leq a \leq 2000$ (8000)	$0.0001 \leq IWC \leq 3.0$
Typical:	columns, bullets, rosettes, plates	250	0.025

Table 4.1: The ranges and typical values of shape, major dimension and IWC for cirrus clouds. Note: parenthetical values are extremely atypical.

component of the fall direction. This is a general characterization and in reality a three dimensional picture might include motions such as spiraling oscillations, fluttering, and rotation about an axis normal to the fall line. Air motions within the cloud, such as turbulence, may modify this behavior. There is no mechanism to produce a preferred orientation for a particular face or edge of hexagonal particles apart from electrical affects which are not of concern here. From the perspective of radar modeling, we portray cirrus particles as falling with their major dimensions oriented in a horizontal fashion with some canting. Within this preferred orientation the ice particles will be randomly oriented. Detailed calculations of the effects of distributions of canting angles on radar signals have been done by Matrosov (1991b); Vivekanandan et al. (1991). Although the effects of canting are significant on radar signals, a canting angle of zero was assumed in this work for numerical expediency.

In terms of the modeling of scattering properties of ice crystals we were interested in the complex refractive index (m), which depends upon the frequency and temperature of the ice. The complex refractive index of ice were interpolated from tables produced by Warren (1984). It should be noted that there is a large degree of uncertainty in the imaginary part due to the lack of reliable measurements. In Figure 4.1 the temperature dependence of the complex refractive index was examined at wavelengths of 1.4 mm, 3.16 mm, 8.66 mm, and 22.1 mm. It is evident from this figure that there is very little difference in the real part of the complex refractive index at these temperatures and wavelengths; to two significant figures $Re(m) = 1.78$. The imaginary component is very small at all wavelengths, never dropping below -0.01 for the cases considered here. It is evident that both the real component and the imaginary component (in the absolute sense) increases with increasing temperature. The phase velocity is proportional to real component of the complex refractive index and the imaginary part determines the absorption. From Figure 4.1 it can be concluded that absorption is very small for ice crystals at these frequencies.

The temperature within cirrus clouds can range from approximately $-20°C$ to temperatures colder than $-60°C$. Because both the real and imaginary components of the complex refractive index exhibit relatively little variation over this range of temperature, the temperature at which the refractive index is calculated is somewhat arbitrary. We computed the refractive index at $-27°C$: for $\lambda = 3.16\ mm$, $m = (1.782 - i0.0028)$ and for $\lambda = 8.66\ mm$, $m = (1.783 - i0.0014)$.

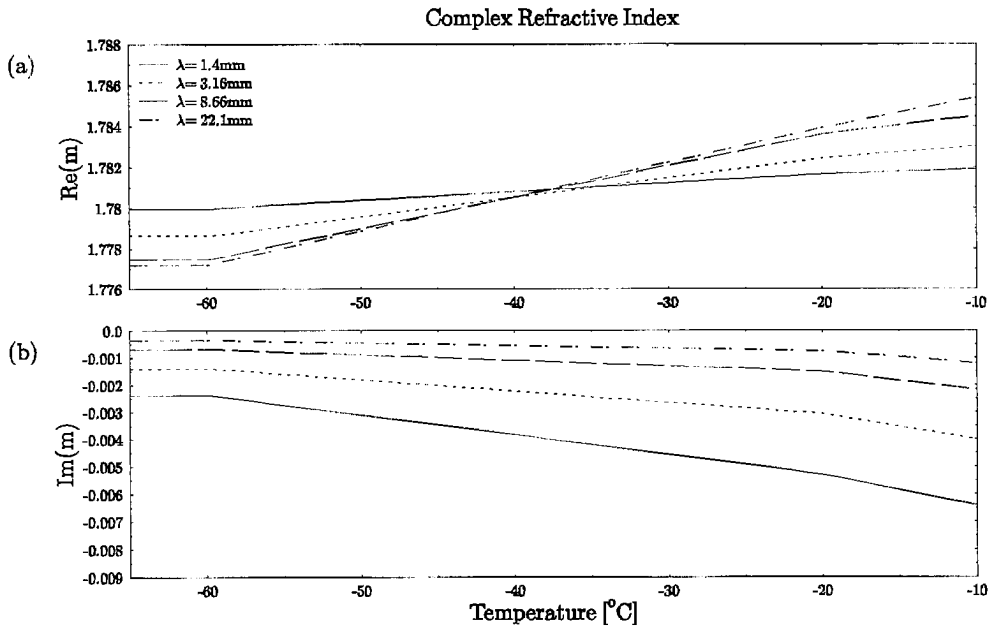

Figure 4.1: The temperature dependence of the complex refractive index ($m = n - ik$) of ice at wavelengths of 1.4 mm, 3.16 mm, 8.66 mm, and 22.1 mm.

4.1.2 The Discretized Modified Gamma Distribution

The most difficult aspect of modelling cirrus particles is to properly represent the particle size distribution. The extreme environmental conditions under which cirrus are found, coupled with their remote nature, make *in situ* measurements very difficult. Reported measurements of size distributions tend to be biased towards larger particles. This is due to our lack of ability to count the smallest crystals reliably (*i.e.* crystals with major dimensions approximately less than 100 μm). It is also difficult to measure the major dimension due to the methods employed in capturing the crystals and to the highly variable crystal morphologies.

One distribution which is commonly used to represent cirrus particle size distributions is the modified gamma distribution (e.g. Flatau et al., 1989; Dowling and Radke, 1990; Kosarev and Mazin, 1991; Matrosov et al., 1992; Vivekanandan and Adams, 1993). It is not overly complex in that it only has two free parameters and yet it is flexible enough to capture the most salient feature present in many of the observations: namely a single peak. As more is learnt about cirrus, it is possible that our depiction of cirrus ice crystal size distributions will change. For instance, bi-modal distributions may be prevalent enough to be relevant (e.g. Mitchell, 1994). We shall proceed, however, with the modified gamma distribution which gives the number concentration per unit interval by the relation

$$N(D) = aD^{\alpha}e^{-bD}, \qquad b = \frac{\alpha + 3.67}{D_m}. \tag{4.4}$$

The distribution is parameterized as a function of the major dimension of the particle (D). The two free parameters are D_m and α and it is these two parameters which control the character of the distribution. The parameter α is related to the width of the distribution whereas D_m is the dimension of the median of the third moment of the distribution. Evans (1993) has shown that the volume of nonspherical particles increases more slowly than the third power because of the changing aspect ratio. Therefore the median of the third moment of the distribution is not the median of the volume. The coefficient 'a' is discussed below.

The scattering calculations were done in logarithmic intervals at 14 points for each morphology. With 14 bins, it is difficult to obtain an accurate representation of the distribution and care must be taken in the discretization. We followed Evans (1993) in dealing with this problem. The scattering properties of an ensemble of ice crystals is given by

$$\int_0^\infty N(D)\mathbf{S}(D)dD \approx \sum_{i=1}^{n} \mathbf{S}(D_i) \int_0^\infty N(D) \left(\frac{D}{D_i}\right)^p dD = \sum\sum_{i=1}^{n} N_i \mathbf{S}(D_i). \tag{4.5}$$

The factor $(D/D_i)^p$ has been introduced to account for the fact that the relative contribution of the scattering property of a given size increases with increasing particle size. In the modified gamma distribution it follows that the N_i are given by

$$N_i = aD_i^{-p} b^{-(\alpha+p+1)} \left[\Gamma(\alpha+p+1, bD_i^u) - \Gamma(\alpha+p+1, bD_i^l)\right]. \tag{4.6}$$

The incomplete gamma function is computed via $\Gamma(a,x) = \int_0^x e^{-t} t^{a-1} dt$. Since the D_i at which the scattering calculations were done were spaced logarithmically, the lower and upper bounds of bin 'i' are given by the geometric mean about D_i

$$D_i^l = \sqrt{D_{i-1} Di} \quad and \quad D_i^u = \sqrt{D_i Di+1}.$$

The lower and upper limits of the distribution were determined according to the range given in Table 4.1,

$$D_1^l = 10\mu m \quad and \quad D_{n=14}^u = 2000\mu m.$$

The appropriate selection of the parameters α, D_m, and p are examined in Section 4.2. The coefficient 'a' was determined by a renormalization procedure and was based on the specification of the IWC. Effectively, this means that the total concentration of ice crystals is adjusted to give the desired value of the IWC.

4.2 SENSITIVITY TO DISTRIBUTION

It is the objective of this section to gain an understanding of the effects of the size distribution on the scattering properties of ice crystal ensembles. It was not the intent to simulate a particular cirrus cloud, rather, we were interested in studying the scattering

properties in a general sense. With this in mind our strategy was to define a standard distribution and then explore deviations in a reasonable range about it. The standard distribution was obtained through the specification of the free parameters in the modified gamma distribution which might be considered typical of cirrus clouds. The free parameters were the width of the distribution (α), the median of the third moment (D_m), and the power factor (p). As we shall see, the specification of at least one of these parameters is of seminal importance. After defining the standard distribution and range of each of the aforementioned parameters, we examined the effect of this range via a root mean square (RMS) analysis. It was also enlightening to examine the relative contribution of each bin in the distribution to the equivalent radar reflectivity factor.

4.2.1 Specification of the Parameters in the Modified Gamma Distribution

Kosarev and Mazin (1991) report that values for the parameter α fall in the range of $0 \rightarrow 2$ based on measurements primarily made in what was then the Soviet Union. The moderate value of $\alpha = 1$ was taken as typical, which is sometimes referred to as a first order modified gamma distribution (e.g. Matrosov et al., 1992). Since the parameter 'p' is the relative power law increase of the scattering properties, we note that for optically small particles, the scattering goes as the volume squared. For nonspherical particles, Evans (1993) has shown that the volume increases in proportion to $\sim D^{2.5}$ as was discussed in the previous section. Thus for many of the particles which we have considered $p \approx 5$. We considered the range $0 \leq p \leq 6$ in our sensitivity analysis.

The determination of D_m was somewhat more problematic. Despite its inadequacies, the parameter known as the effective radius (r_{eff}) is often used to characterize cirrus particle distributions. Although the notion of effective radius is exact for spheres, its use in the characterization of nonspherical particles is of a dubious nature. We avoided these issues and accepted values of r_{eff} reported in the literature as a first order approximation. An equivalent quantity for nonspherical particles can be considered to be $\langle V \rangle / \langle A \rangle$ which is the ratio of the volume averaged over the distribution to the projected area averaged over the distribution. For spheres $\langle V \rangle / \langle A \rangle = \frac{4}{3} r_{eff}$ and D_m can be parameterized as $D_m = (0.5112 \langle V \rangle / \langle A \rangle)^{2.0243}$.

Values of r_{eff} generally fall in the range of 10 to 150 μm although values outside of this range have been reported (for example see Paul W. Stackhouse, 1989; Stephens et al., 1993). These were then converted to values of D_m which fall into the range $50 \leq D_m \leq 3280$ μm. We added the additional constraint that $D_m < D^u_{n=14}$. That is, D_m should be smaller than the maximum value considered in our distribution (i.e. $D^u_{n=14} = 2000$ μm). If $D_m \geq D^u_{n=14}$, then we would have violated the observations which suggest that the distribution has a single peak beyond which it decays (there would be no peak at all). Consequently we chose $D_m = 800$ μm as our standard size ($R_{eff} = 40$ μm) with a range of $50 \rightarrow 1600$ μm (r_{eff} : $10 \rightarrow 60$ μm). These values of D_m are for spheres; the D_m

	Standard	Range
α	1	0 1 2
$D_m[\mu m]$	800	50 100 200 400 800 1600
p	5	0 1 2 3 4 5 6

Table 4.2: Standard values and ranges of the free parameters in the modified gamma distribution.

for nonspherical crystals can be either greater or less than these values depending on the shape (Evans, 1993). The standard values and ranges of the parameters α, D_m, and p are summarized in Table 4.2.

4.2.2 RMS Analysis

The methodology of this section was to employ RMS differences to gauge the variability of the computed radar observables caused by the ranges of parameters in Table 4.2. The results were expressed in terms of a percentage of the RMS difference over the average of the scattering property for each set of parameters. When considering one parameter, the other parameters were set to the standard values as discussed above. For example when considering the variability introduced by the range of values of the parameter 'α' ($0 \leq \alpha \leq 2$), D_m and p were held fixed at 800 μm and 5 respectively. Then the average and RMS difference of the equivalent radar reflectivity factor (mm^6m^{-3}) was computed for this range of α. We considered cylinders, hexagonal plates, and two sets of equal volume spheres. One set of spheres possessed volumes equal to the cylinders and the other had volumes equal to the plates. The radar observables computed were the horizontal and vertical effective radar reflectivities (Z_{hh} and Z_{vv}) and the main and cross, circularly polarized, effective radar reflectivities (Z_m and Z_o). The results are presented in Table 4.3 and are expressed as the fraction of the RMS difference to the range average (in %).

We considered the RMS difference for each parameter of the distribution as a function of the polarization, radar elevation angle (Θ), wavelength, and shape. It was observed that the differences amongst the various polarizations were negligible, therefore the numbers presented in the table can be considered as being representative of all of the polarizations (for most cases this is true to within 1%, in the few remaining cases it was less than 10%). The RMS difference tends to increase with decreasing Θ for cylinders, whereas the difference exhibits the opposite and slightly more significant trend for plates. The symmetry of spheres precludes any dependence on Θ. The RMS difference at the two wavelengths are comparable, the difference between them ranging from a few tenths of a percent to approximately twenty percent. It can also be seen that the differences between the various shapes are relatively small for a given parameter in the distribution.

The most significant features observed in Table 4.3 are the differences between the various parameters of the distribution. The RMS differences introduced by varying both α

		α		D_m (μm)		p	
Shape	Θ	λ : 3.16	λ : 8.66	λ : 3.16	λ : 8.66	λ : 3.16	λ : 8.66
Cylinder	90	4.4	4.5	101	100	3.1	3.0
	60	5.0	4.6	96	99	2.6	3.0
	30	5.4	4.7	88	97	2.1	2.8
	0	5.3	4.8	88	97	2.0	2.7
Hex. plate	90	6.0	5.8	105	105	5.3	5.2
	60	3.5	5.4	100	104	4.0	5.0
	30	0.9	4.7	84	103	1.9	4.7
	0	2.5	4.3	78	102	1.1	4.4
Sphere (H.P.)	90	0.1	0.7	83	86	6.7	8.6
Sphere (Cyl.)	90	0.1	1.4	84	88	5.2	8.1

Table 4.3: RMS difference analysis of the variability introduced by the range of values in the parameters α, D_m, and p of the modified gamma distribution. Expressed as a percent of the average equivalent radar reflectivity factor.

and p are on the order of 5% to 10% of the average, while the RMS differences introduced by varying D_m is in excess of 100%. Clearly D_m is the most significant parameter in the modified gamma distribution. In the remaining calculations of this chapter we were careful to consider a range of values for the parameter D_m.

4.2.3 Cumulative Analysis

We now pose the question 'Which part of the distribution contributes most to the total reflectivity?' This is an important question from the perspective of modeling and for the development of remote sensing techniques. Given the uncertainty of our *in situ* detection of the smallest crystals, it is important to ascertain how much of a contribution the smallest crystals make. This information is also useful to the selection of the appropriate scattering model in accordance with the conclusions of Chapter 3.

As was described above, the scattering properties of ensembles of particles was discretized into 14 bins. In any given bin there are two, sometimes competing, factors which make up the contribution of a given bin to the total reflectivity; the number of particles in the bin and the backscattering cross section of each particle. It was both interesting and useful to look at the contribution to the total reflectivity of an ensemble of ice crystals on a bin-by-bin basis. We examined these features for two morphologies, hexagonal plates and cylinders, because they represent two of the three general shapes found in cirrus (i.e. planar, columnar and spatial). The six particle size distributions which were used for this section are presented graphically in Figure 4.2. This figure will be of assistance in interpreting the remaining figures of this section.

In the following series of figures we offer two related views of the relative contribution of each bin to the total reflectivity: cumulative reflectivity ratios and binned fractional reflectivities. Their mathematical definition will make meaning of these two quantities

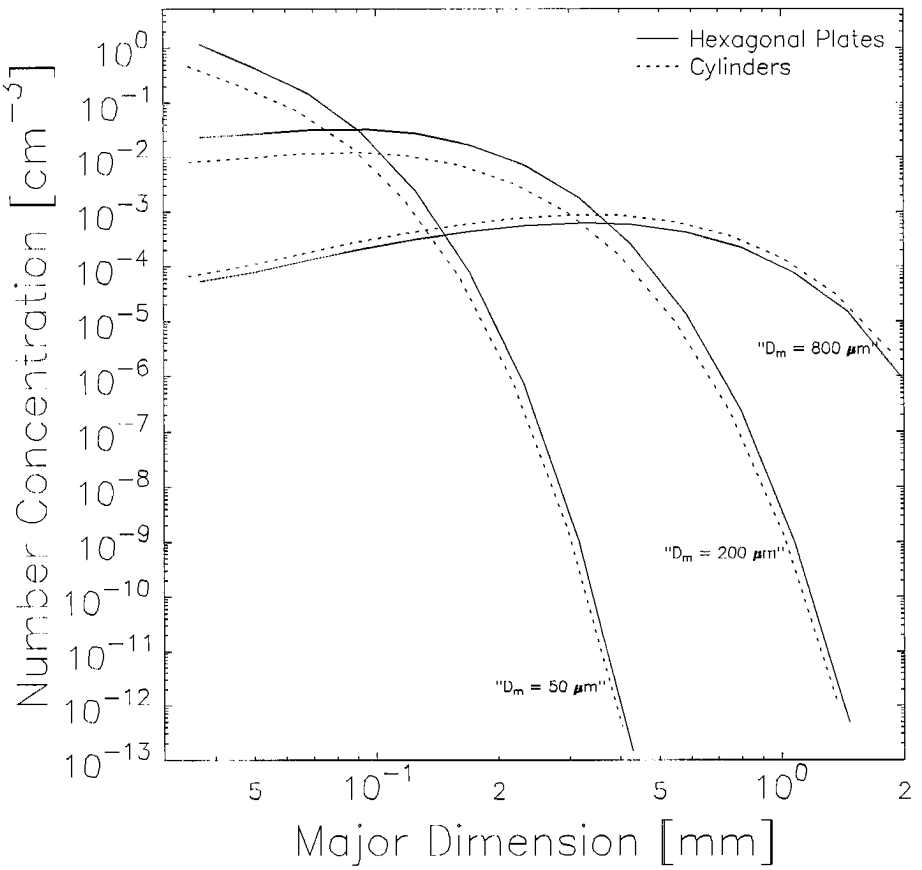

Figure 4.2: The six ice crystal size distributions used in the cumulative analysis.

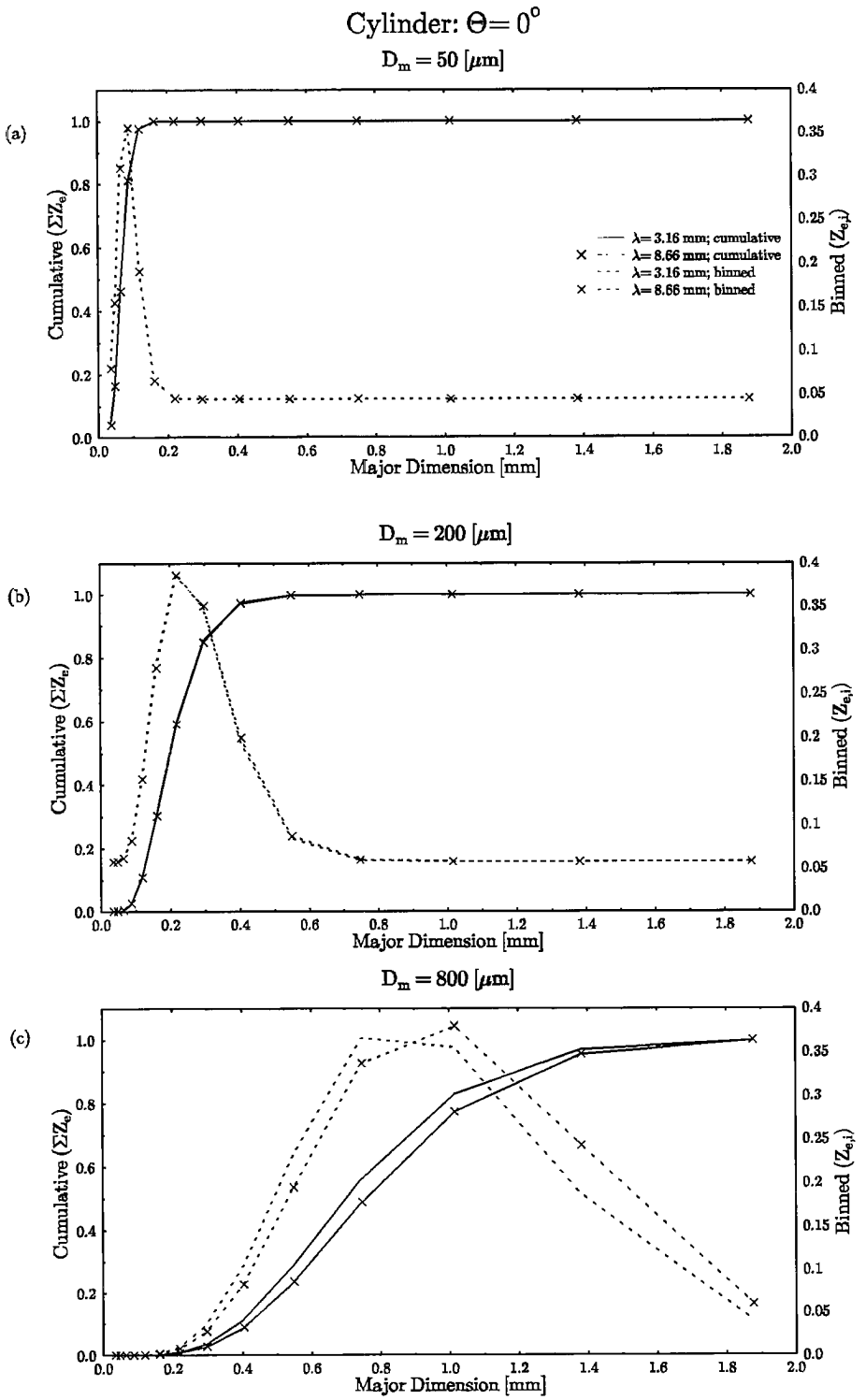

Figure 4.3: Plots illustrating the cumulative (left axis) and bin-by-bin (right hand axis) contributions of each bin to the total effective radar reflectivity for various distributions of cylinders. D_m was allowed to vary while the remaining parameters of the distribution were set to their standard values as discussed in the text. Data are presented at wavelengths of 3.16 and 8.66 mm and the radar elevation was $\Theta = 0°$. (a) $D_m = 50\mu m$, (b) $D_m = 200\mu m$, (c) $D_m = 800\mu m$.

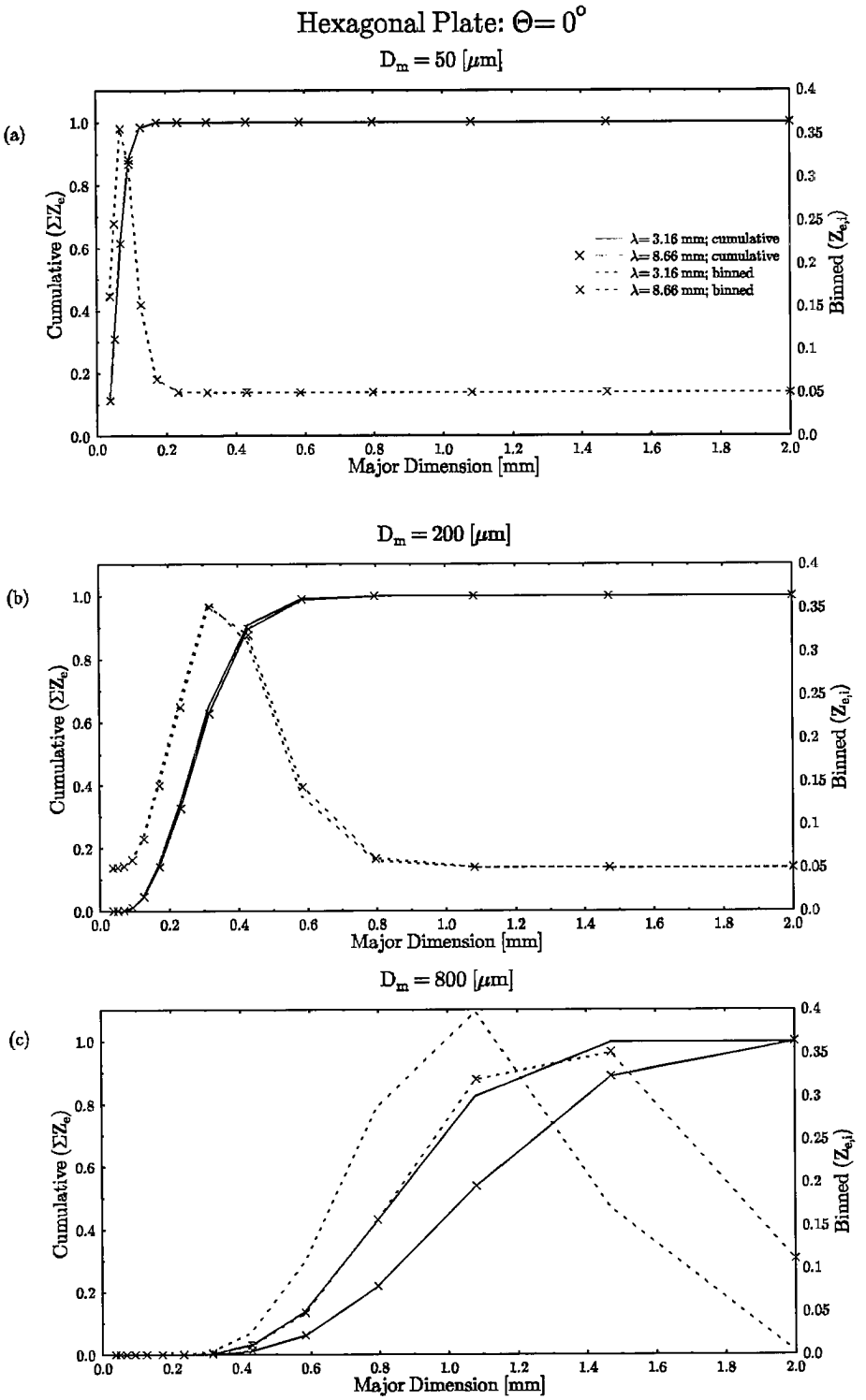

Figure 4.4: Same as figure 4.3, except for hexagonal plates.

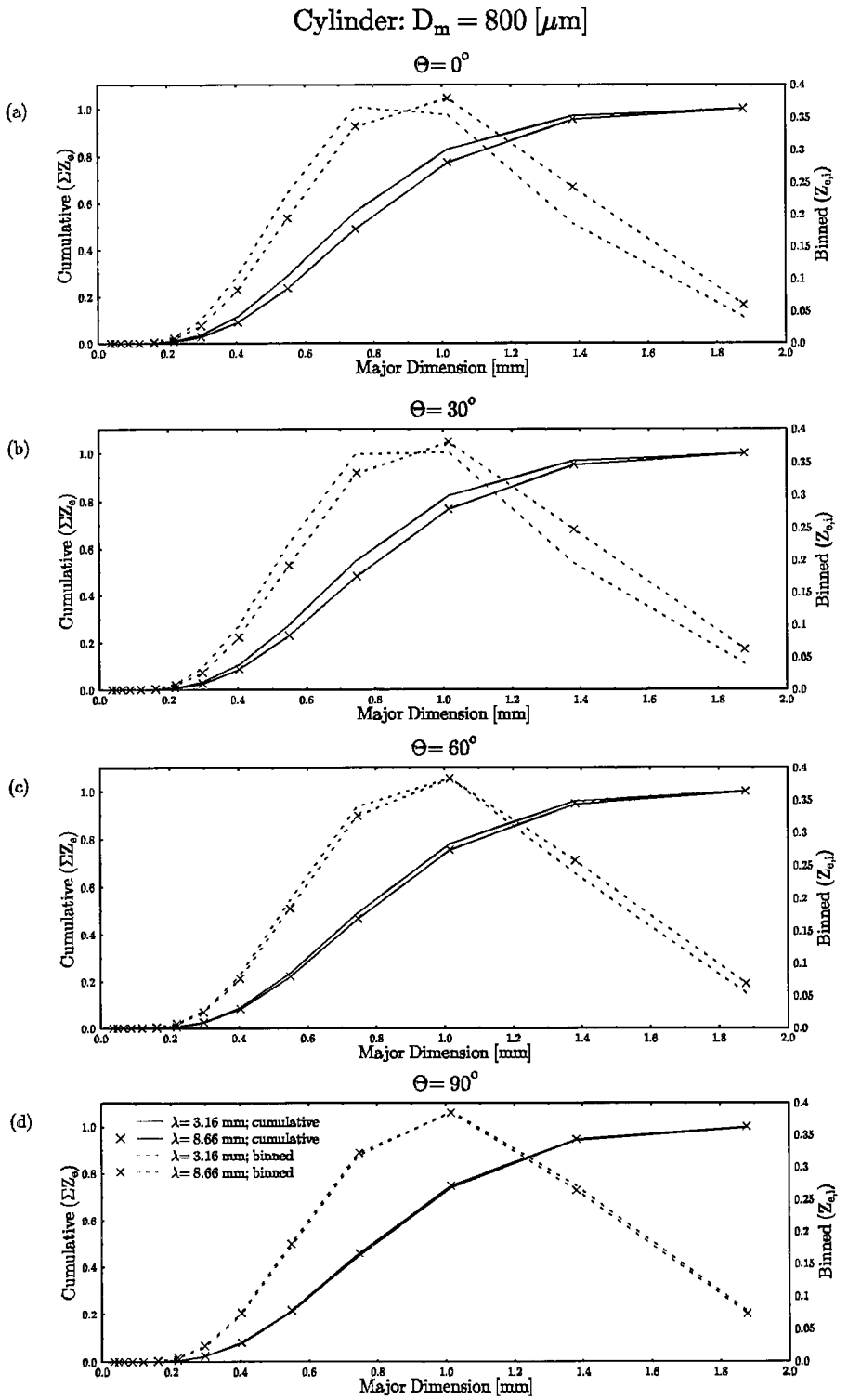

Figure 4.5: An examination of angular effects on the cumulative and binned effective radar reflectivities for cylinders distributed according to the standard parameters defined in Table 4.2. Data are presented at wavelengths of 3.16 and 8.66 mm. (a) $\Theta = 0°$, (b) $\Theta = 30°$, (c) $\Theta = 60°$, (d) $\Theta = 90°$.

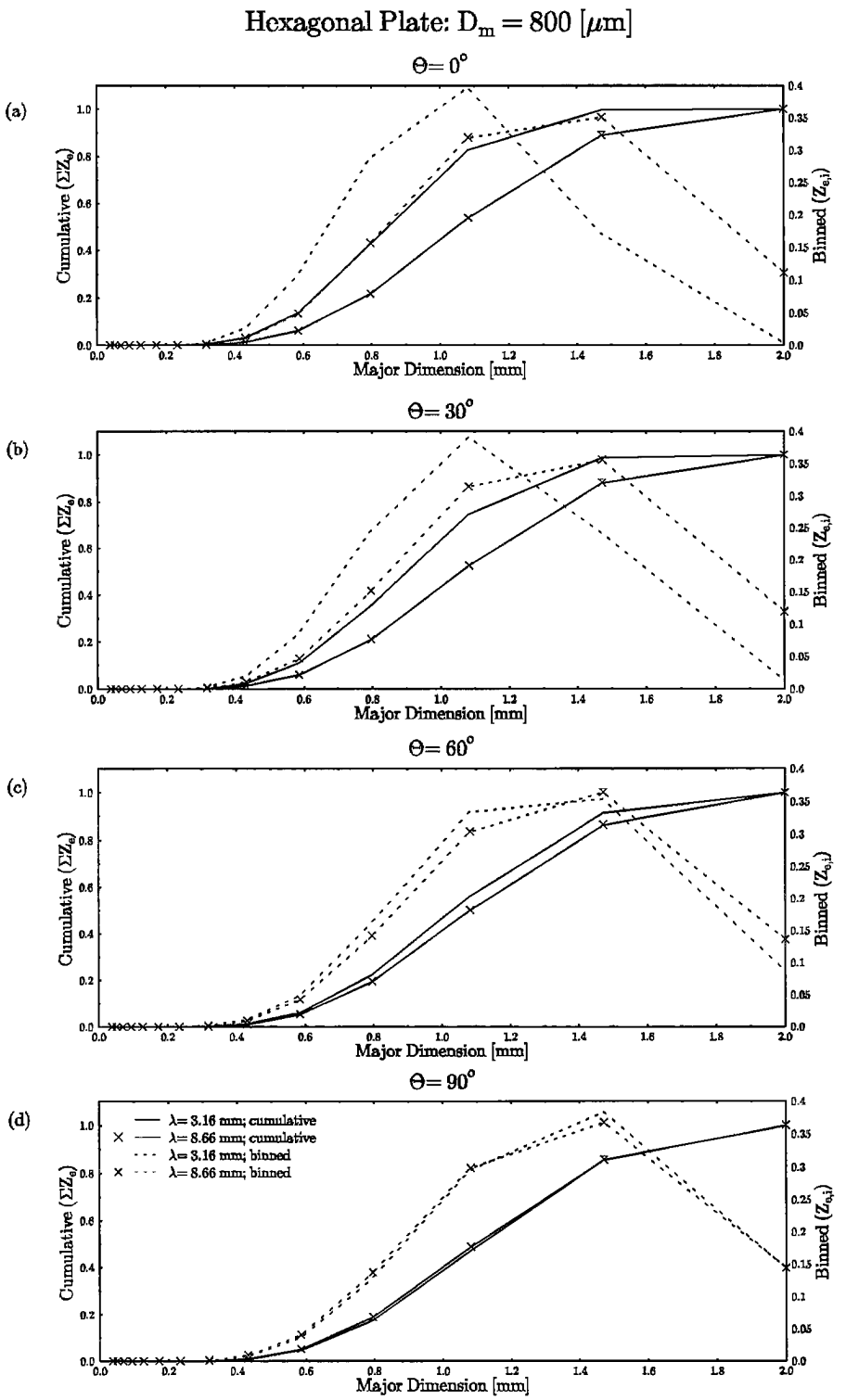

Figure 4.6: Same as figure 4.5, except for hexagonal plates.

more clear (which shall be referred to as the cumulative and binned reflectivities for simplicity):

$$\begin{aligned} \textit{Binned} \quad &: \quad \frac{N_i Z_i}{Z_{tot}} \quad 1 \leq i \leq 14, \\ \textit{Cumulative} \quad &: \quad \frac{\sum_{i=1}^{\hat{n}} N_i Z_i}{Z_{tot}} \quad 1 \leq \hat{n} \leq 14. \end{aligned}$$

Where $Z_{tot} = \sum_{i=1}^{14} N_i Z_i$. These quantities were computed for the polarized reflectivities Z_{hh}, Z_{vv}, Z_m and Z_o. The calculations demonstrated that for any particular combination of Θ, λ and D_m, the differences between the various polarizations were small from both the binned and cumulative perspectives. Therefore we only presented plots of Z_e to simplify matters.

Before characterizing the relative contributions for the various bins we made the following general observations. There were four factors to consider, the wavelength (λ), the radar elevation (Θ), D_m, and the ice crystal morphology. The other parameters of the distribution were set to their standard values. The single greatest factor was D_m, as would be anticipated of such plots. The plates were more sensitive to variations in wavelength and Θ than were the cylinders. The effects of Θ were small for $D_m = 50$ and 200 μm, but were more significant when $D_m = 800$ μm. For small particles changing the elevation did not significantly alter the contribution of a given bin but as the number of large particles increases the differences caused by changing the radar elevation becomes important. It was also evident that there was very little difference between the two wavelengths for small elevations and the lesser two values of D_m. As Θ decreases (approaching edge on incidence), however, the differences between the two curves representing each wavelength became important when $D_m = 800$ μm. We conclude that the presence of large crystals was the overriding factor in determining the bin-by-bin contribution to the total reflectivity.

In Figures 4.3 and 4.4 we present the cumulative and binned responses for $\Theta = 0°$, $\lambda =$ 3.16 and 8.66 mm, and for three values of D_m (50, 200, 800 μm). Plots at other elevations were of a similar character but differences between wavelengths were less pronounced as will be shown in the next series of figures. For particles greater than approximately 450 μm, $\lambda = 3.16$ mm was much more responsive to the smaller crystals.

Panel (a) in both Figures 4.3 and 4.4 shows that particles which have dimensions less than 100 μm (bins $1 \rightarrow 4$) account for $\sim 90\%$ of the total reflectivity. This is due to the large numbers of these crystals and the very rapid decrease in concentration with size (see Figure 4.2). For $D_m = 200$ μm (panel (b)), particles for which $D < 100$ μm account for virtually none of the total reflectivity even though there are still quite a few of them. The major contribution to the total reflectivity is now given by crystals in the range of $200 \leq D \leq 600$ μm, which is due to the rapidly growing reflectivity of the

individual particles ($\propto V^2$, for volume V). For $D_m = 800\ \mu m$, the greatest contribution is from particles in the range $600 \leq D \leq 1400\ \mu m$ even though there were particles in the 2000 μm bin. The relatively small contribution of the 14^{th} bin was due to the decaying concentration. At this value of D_m, cylinders smaller than $\sim 200\ \mu m$ and plates smaller than $\sim 300\ \mu m$ contribute virtually nothing to the total reflectivity which can be attributed to both the distribution and the reflectivity of the individual scatterers.

Figures 4.5 and 4.6 show how the two wavelength curves evolve with changing elevation. The parameter D_m was fixed at 800 μm. Both wavelengths become more sensitive to smaller crystals as $\Theta \rightarrow 0°$. The effect is much more pronounced for $\lambda = 3.16\ mm$. Because the wavelength dependencies begin to moderate and eventually disappear for $D_m < 800\ \mu m$ it may be possible to use a dual wavelength radar mounted on an aircraft to ascertain this parameter in cirrus. The presence of spatial particles may dampen this difference as is indicated by analogous calculations for equal volume spheres (not presented). Under these circumstances, there is very little difference between the two wavelengths even at $D_m = 800\ \mu m$.

From these figures we can characterize the size dependent scattering as follows. Even though the scattering cross section can become quite large, the number concentration tends to be the dominating factor. For distributions dominated by small crystals, wavelength and shape are irrelevant. As such this makes the parameter D_m the most important consideration in the modeling of radar reflectivities with the modified gamma distribution. Since it is also the least understood parameter, efforts should be made at determining its value via multi-parameter radar observations and/or other remote sensing and *in situ* methods. We have also shown in this section that the contribution to the total scattering is nearly identical at both wavelengths. Only for distributions with relatively large numbers of large ice crystals and at the lesser radar elevations did we begin to see a wavelength dependence. Under these conditions $\lambda = 3.16\ mm$ was more responsive to the smaller crystals. The overall character of the cumulative reflectivities was similar for the two morphologies, but the small cylinders have a slightly more significant effect than their planar counterparts.

Given that $D_m = 50\ \mu m$ is the lower boundary of the range of expected values, the uncertainty in the concentration of small particles is not an issue of concern for our understanding of radar measurements of cirrus. This conclusion is valid even at $\lambda = 3.16\ mm$. Under all of the circumstances considered, the polarization of the reflectivity was a small but insignificant factor. This conclusion is valid in the cumulative sense but says nothing about the differences induced on the various polarizations by variations of D_m. It remains for this issue to be addressed.

	CASE				
Shape	**1**	**2**	**3**	**4**	**5**
$C1e, C1f$	100%	0%	50%	37.5%	0%
$P1a$	0%	100%	50%	25%	0%
$C2a$	0%	0%	0%	37.5%	0%
Sphere ($C1e$)	0%	0%	0%	0%	50%
Sphere ($P1a$)	0%	0%	0%	0%	50%

Table 4.4: The five cases used in the determination of the $IWC - Ze$ relations. Note that the hexagonal columns are being modeled as a 50-50 mixture of cylinders and hollow cylinders and that the $C2a$ are planar rosettes with 3 spines.

4.3 IWC-Z_e RELATIONS

In this section we seek a relationship between the IWC and the effective radar reflectivity factor (Z_e). Our methodology was to compute Z_e as a function of the IWC for various ice crystal morphologies. For each morphological case, $Z_e(IWC)$ was computed for D_m = 50, 200, and 800 μm. The morphological cases are defined in Table 4.4. The calculations were done at $\lambda = 8.66\ mm$ and $\Theta = 90°$. The data are presented in Figure 4.7.

In practice $IWC - Z_e$ relationships are expressed in a power-law relation of the form

$$IWC = aZ_e^b. \tag{4.7}$$

In Figure 4.7 we have also plotted two curves representing the $IWC - Z_e$ power-law relations of Sassen (1987) and Liao and Sassen (1993). In a composite of several field measurements Sassen (1987) determined

$$IWC = 0.037 Z_i^{0.696}. \tag{4.8}$$

We will refer to this equation as Sassen-87. In Sassen's paper, he makes the distinction between Z_i and Z_e which are related through the dielectric properties ($|K_{i,w}|^2$) of ice and water. In this work our definition of Z_e is equivalent to Sassen's Z_i. The relation of Liao and Sassen (1993) was determined theoretically through calculations very similar to those used in this research. Their method utilized a collection of actual ice crystal size distributions from which they estimated the IWC. Their scattering calculations employed a combination of Rayleigh and conjugate gradient-FFT models and complex morphologies. Their nonlinear least squares fit yielded the relation

$$IWC = 0.0749 Z_i^{0.78}. \tag{4.9}$$

The agreement between these two equations is good considering the disparate means of determining them. The results obtained from our calculations poorly relate to the two equations just discussed. We shall now examine why.

There are two very striking features which can be seen in Figure 4.7. The first is that the slope of the points representing our calculations is drastically different than the two other relations. In fact for our calculations $b = 1.0$, exactly. This is independent of morphology and D_m. The second very striking feature is that the family of curves representing $D_m = 200\ \mu m$ and the other family of curves representing $D_m = 800\ \mu m$ tends to bracket the empirical curve of Sassen (1987). Since Sassen's empirical relation represents numerous cirrus cloud types it is reasonable to conclude that the range of values presented in Section 4.1 should be refined. It should be noted that the theoretical relation of Liao and Sassen (1993) are also bracketed by these two values of D_m. Based on these observations, we propose that $100\ \mu m \leq D_m \leq 1000\ \mu m$ constitutes a more realistic set of general limits of D_m for cirrus. This conclusion should be taken as a starting point for independent validation and additional field work and not be accepted as definitive.

Since 'a' is simply a constant multiplier which shifts the curves up and down, it can be argued that the most important parameter in the power-law relation is the exponent 'b'. From the figure it is evident that both the ice crystal shape and D_m effect 'a'. What determines the parameter 'b' is less obvious. As it was in the slope that our results were in the greatest error, it behooved us to seek an explanation. We hypothesized that there was a functional relationship between the the parameter D_m and the IWC. To test this hypothesis we proposed the relation

$$D_m = 0.669 IWC^{0.162}. \tag{4.10}$$

This relation was obtained by noting that the lower limit of the Sassen-87 curve falls approximately in the $D_m = 150\ \mu m$ regime, and the upper limit of the Sassen-87 curve falls within the $D_m = 800\ \mu m$ regime. Using case 4, the most diverse mixture of morphologies which were considered, we recomputed the reflectivity data where D_m was parameterized as we have just indicated. The results are presented in Figure 4.8 along with the empirical Sassen (1987) relation and the theoretical relation given by Liao and Sassen (1993). For comparison, the nonlinear least squares fit of our data is given by ($R^2 = 100.00\%$)

$$IWC = 0.032 Z_e^{0.703}. \tag{4.11}$$

Although these results are quite intriguing, care must be take not to read too much into them. The fundamental weakness lies in the fact the theoretical calculations have little basis in observation. There was no *a priori* motive for parameterizing the $D_m - IWC$ relation in this particular way, and in effect the answer was obtained by 'tuning' the results. What is needed is an independent method of linking the D_m to the IWC as is suggested by these results. Such a method may prove feasible through multi-parameter radar measurements or by utilizing other remote sensing techniques which rely on a fundamentally different interaction of radiation with cirrus particles. As one example of such

a possibility consider the work of Matrosov et al. (1992), in which they combined an infrared radiometer and an 8 mm radar to retrieve cirrus cloud parameters. Nevertheless, equations 4.10 and 4.11 curve can serve as a crude means of estimating D_m from reflectivity measurements.

Because the physical process of nucleation places an inherent limit on the total number of ice crystals under a given set of conditions, it is reasonable to expect some sort of functional dependence between the IWC and D_m. Variations in nucleation rate and mechanism can work to increase the total number of ice crystals at the expense of crystal size, or conversely, can limit the total number in favor of larger crystals (see DeMott et al., 1994). For example, crystals can begin to grow rapidly, consuming the available moisture, thereby limiting the total number of crystals and causing a greater number of large crystals. Therefore a parameterization such as (4.10) is not entirely unfounded. This argument does not suggest that 4.10) is correct, merely possible, and on a case-by-case basis significant deviations are expected.

An identical procedure was carried out for $\lambda = 3.16\ mm$ yielding the nonlinear least squares power-law fit ($R^2 = 100.00\%$)

$$IWC = 0.030 Z_e^{0.696}. \tag{4.12}$$

The data are presented in Figure 4.9. There is virtually no difference between the 8 mm and 3 mm results which indicate that reflectivities obtained from radars of either wavelength can be used to retrieve the IWC and D_m with the same equations. This conclusion is in agreement with the results of the previous section. The results of the previous section, however, suggest that the difference should be evident for radar elevation angles other than 90°.

A morphological dependence of the $IWC - Z_e$ is quite evident in Figure 4.7. We note that spheres (case 5) over-estimate the more realistic collection of $C1e$, $C1f$, $P1a$ and $C2a$ (case 4) by 2 to 15 dB depending upon the IWC and D_m. To estimate the effect of this variability on the derived coefficients of the power-law $IWC - Z_e$ relation, we computed the nonlinear least square power-law fit for case 4 and case 5 combined. The error was significant at $R^2 = 60.4\%$.

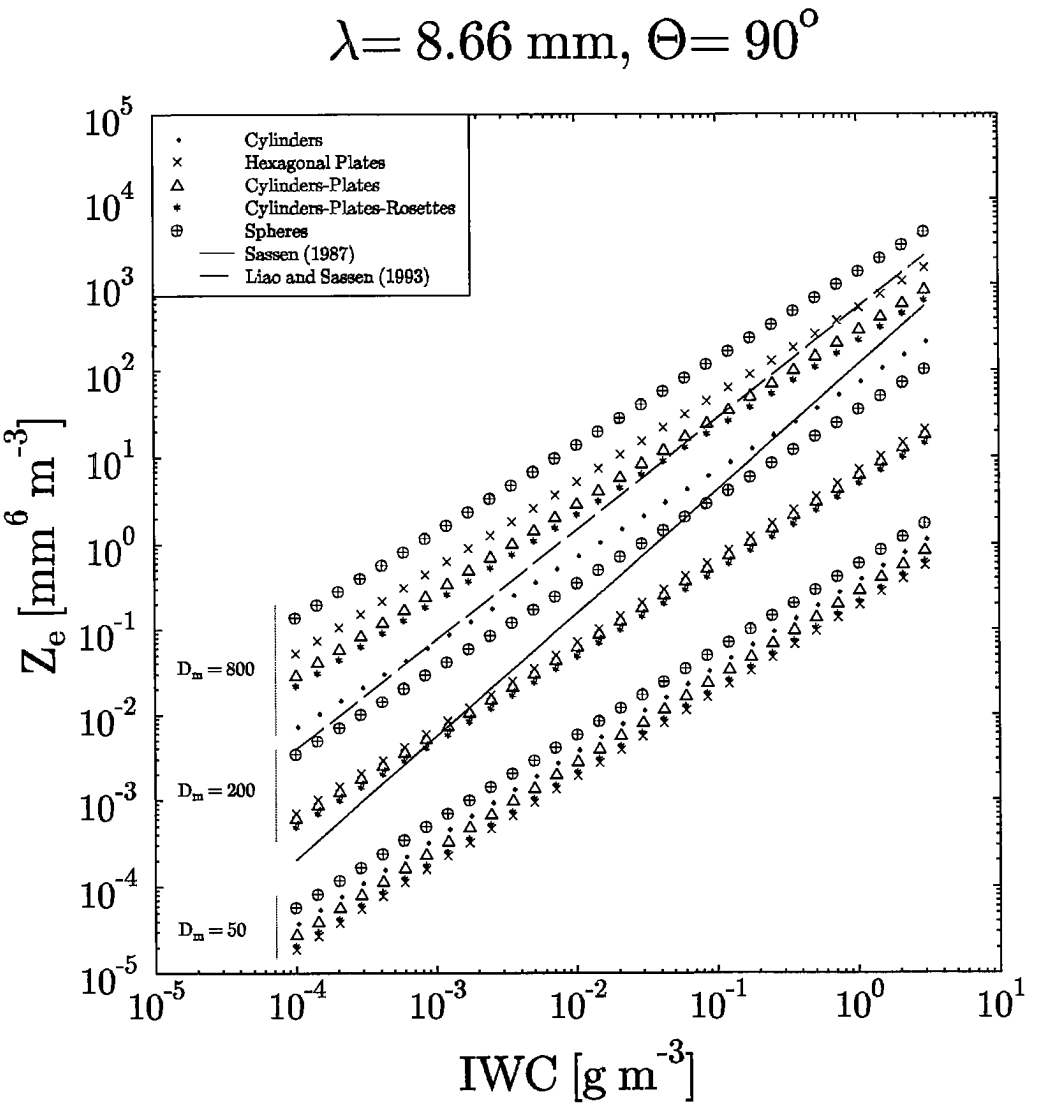

Figure 4.7: Plots of equivalent radar reflectivity factor as a function of the IWC for various combinations of shape and D_m at $\lambda = 8.66\ mm$. The empirical relation of Sassen(1987) and the theoretical relation of Liao and Sassen (1993) are presented for comparison.

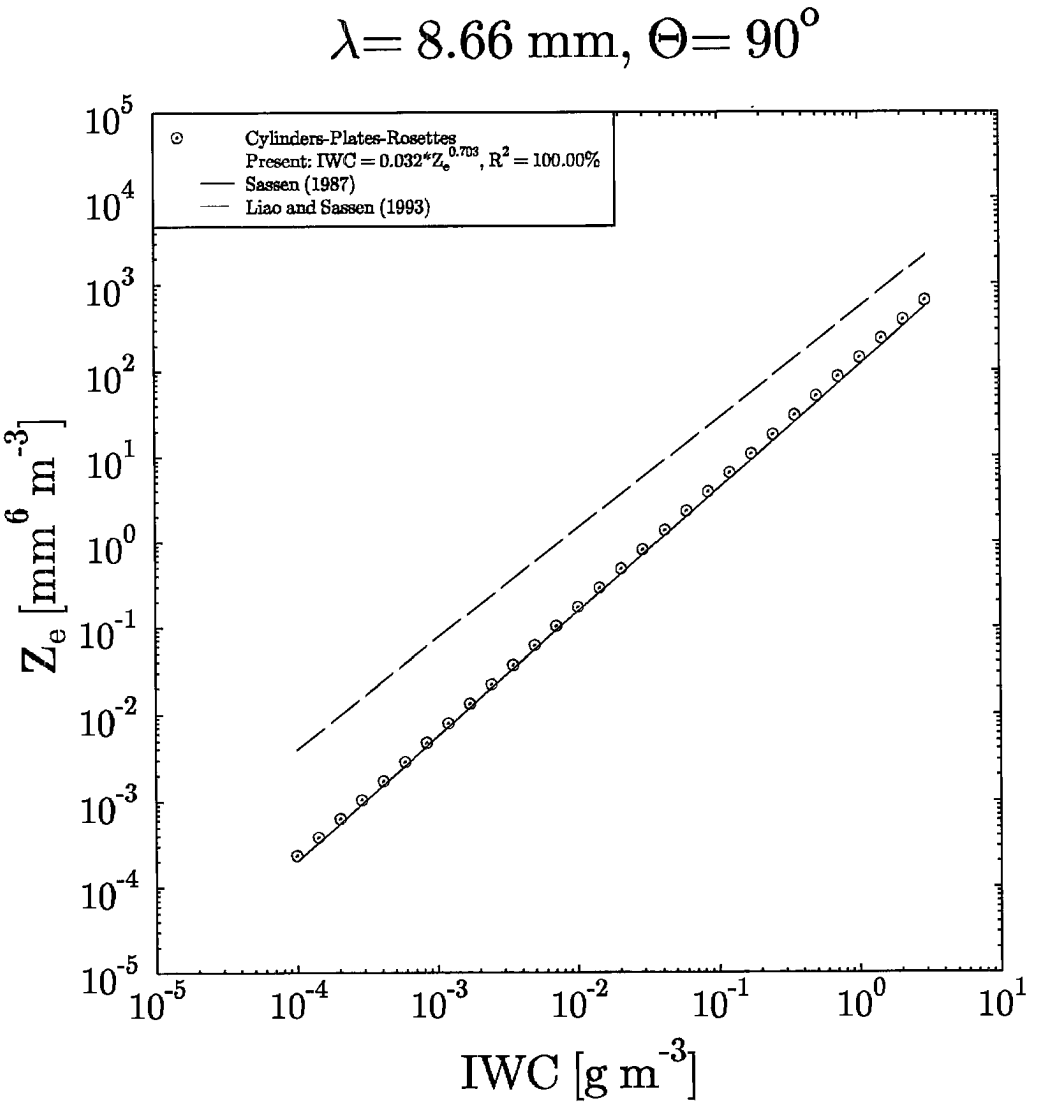

Figure 4.8: $IWC - Z_e$ determined from present work and compared with previous relations, where D_m has been parameterized according to (4.10).

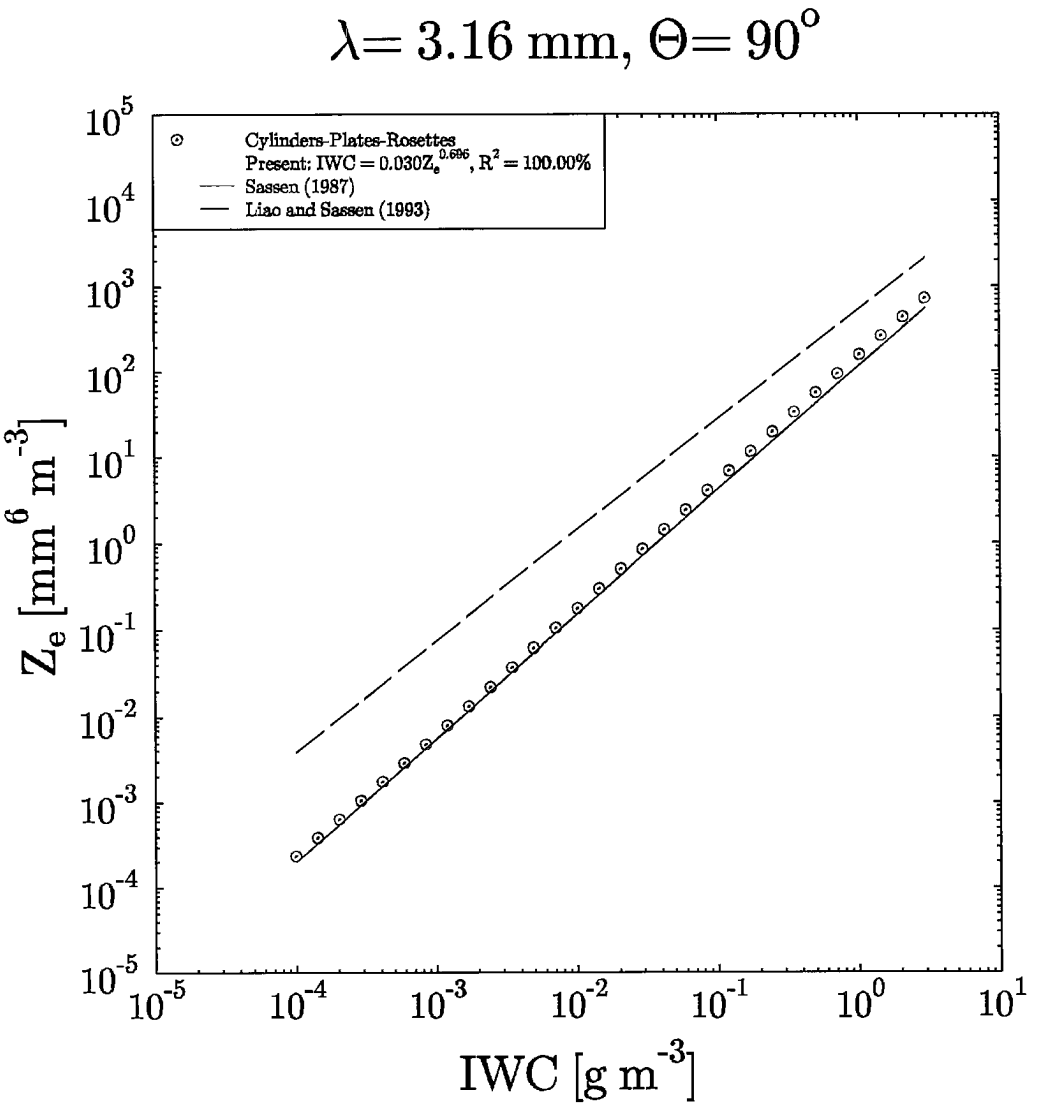

Figure 4.9: Same as Figure 4.8, except $\lambda = 3.16$.

Chapter 5

SUMMARY & CONCLUSIONS

The proper role of modeling is to both elucidate and guide our physical picture to a more profound understanding of nature. In practice modeling is based on observations of natural phenomena, which is then input into our models. This is then one limiting factor of modeling; how good is our present view of the facts. The quality of our models is a second limiting factor. The answer is a reflection of both our understanding of the phenomena and our technological prowess.

The work presented in this study examined issues about how we model the phenomena of backscattering by ice crystals found in cirrus clouds. Our model, the discrete dipole approximation (DDA) has been validated against exact theories, is founded on sound physical principles which have withstood the test of time, and can readily be improved. Presently there is no end in sight for Dyson's technological revolution and in improved numerics. Thus, at this point it may be concluded that the fundamental weakness is in our microphysical understanding of cirrus clouds. In the following sections we summarize what was learned about our ability to model scattering by nonspherical cirrus ice particles at millimeter wavelengths, and where this work will lead to further this understanding.

5.1 WHAT WAS LEARNED

The discrete dipole approximation is an ideal vehicle for exploring some of the complex issues regarding backscattering at millimeter wavelengths. A simple version of the discrete dipole approximation was developed and used to provide insight into the theory and to explore issues such as sensitivity to scattering in the backward direction. Complex behavior was exhibited for the most simple case of only two dipoles.

The DDA was used to determine the minimum number of azimuthal angles which needed to be averaged to simulate a randomly oriented particle. The required number strongly depends on the radar elevation angle, particle morphology, and optical size. There was a weaker dependence on the polarization. It was shown that averaging over 3 to 5 azimuthal angles was required to simulate randomly oriented particles depending on the degree of symmetry (less symmetry implies more angles).

A Rayleigh model was also developed to explore the limitations of the Rayleigh approximation in conjunction with DDA. From the analysis of scattering by single particles,

it has been learned that the assumptions of the Rayleigh theory are most sensitive at the lowest radar elevation angles. The same conclusion applies to the use of spheroidal shapes to represent particles with more complex shapes. Since most applications of radar to cirrus involve high elevation angles, this is not too restrictive. As millimetric radars are mounted on airplanes (e.g. Pazmany et al., 1993), however, such issues become important. The validity of the Rayleigh theory was demonstrated to be sound for modeling cirrus particles at wavelengths of 8 mm and beyond, except for small elevations and large ice crystals ($D \geq\sim 1400\ \mu m$). For wavelengths under 8 mm the Rayleigh approximation broke down well within the range of expected cirrus particle dimensions. The ability of spheroids to represent backscattering by more realistic shapes is sound for cirrus particles at wavelengths of 3.16 and 8.66 mm.

Utilizing semi-realistic shapes, we used the DDA to model scattering by ensembles of ice crystals. Our current understanding of cirrus clouds indicate the presence of ice crystals possessing complex morphologies with sizes which range from 10 μm to 2000 μm. Their distribution is described well by the modified gamma distribution. Our calculations have indicated that the most important and least understood aspect is the value of the median diameter of the third moment of the distribution (D_m).

For most of the ice crystal distributions considered, ice crystals with major dimensions less then 100 μm contribute virtually nothing to the total scattering. We do not need to worry about our difficulty in counting particles smaller than 100 μm from this perspective. The distribution tends to be the dominant factor in our scattering calculations. This underscores the need to accurately determine the value of D_m. Polarization dependence is small and the differences at the two wavelengths considered is miniscule for all but $D_m = 800\ \mu m$ and at the lesser angles.

Calculations of reflectivity as a function of IWC indicate that it may be possible to estimate D_m, and a crude retrieval was developed based on a comparison with empirically determined relations. These calculations suggest a refined set of limits for the parameter D_m. Although the agreement is outstanding and highly suggestive, these results should be viewed as tentative in light of further work, especially additional observations.

5.2 SUGGESTIONS FOR FURTHER RESEARCH

There are several directions in which this work should proceed. The first direction is along the lines of validation. Two recent field experiments offer the opportunity to test some of our theoretical results. The first data set was obtained during the First International Satellite Cloud and Climatology Experiment, Phase II (FIRE II) held over the continental United States. This is a rich data set which includes measurements with various radiometric instruments including 3 and 8 mm radars. There were also numerous *in situ* microphysical measurements made. The second data set was obtained at the University of Wyoming's Elk Mountain Observatory in 1992. A 3 mm radar was collocated

with a wind tunnel outfitted with microphysical instruments, allowing them to both microphysically sample and interrogate with the radar, the same volume of an orographic ice cloud.

Another area in which we should proceed is improved modeling. Most importantly we suggest the addition of spatial rosettes, and further consideration of the issue of target orientation. The latter should be attempted after careful consideration of the literature (see Section 2.1), as this is a numerically intensive procedure. In this respect improvements in the DDA model itself may be of assistance. Implementing an improved version of the FFT (non-power of two) would reduce memory requirements and improve the speed. We have not yet fully addressed all of the issues of polarization. It may be possible to use polarization to provide the second piece of information required to unambiguously determine D_m and IWC. This work has emphasized the sensitivity of the backscattered signal by ensembles of ice crystals to the nature of the particle size spectra. Recent measurements (e.g. Arnott et al., 1993) suggest that bi-modal distributions may be an accurate representation of cirrus ice particle spectra. Thus, further investigation into the effects of the particle size distributions on simulated radar returns are necessary. We must consider the effects which bi-modal distributions would have on computed effective radar reflectivity factors.

We should also note that it has been proposed to place a 3 mm radar on a satellite (Graeme Stephens, personal communication 1993). Thus, there are issues such as attenuation through high ice clouds which should be addressed. The data obtained from these calculations could be processed into propagation observables such as attenuation, differential phase shift and differential attenuation with little numerical effort; the data already exists in the form of forward-scattering Mueller matrices.

Finally we should explore the relation between a radar view of cirrus and the picture which is seen by other instruments. This would be achieved through radiative transfer modeling and may provide some insight into the relation of radar observables and optical properties of interest to radiative transfer modeling.

Bibliography

Arnott, W. P., Y. Dong, J. Hallet, and M. R. Poellot, 1993: Role of small ice crystals in radiative properties of cirrus: A case study, fire ii, 22 nov 1991. *Submitted to J. Geophys. Res.*

Atlas, D., M. Kerker, and W. Hitschfeld, 1953: Scattering and attenuation by nonspherical atmospheric particles. *J. Atmos. Terr. Phys.*, **3**, 108–119.

Auer, A. H. and D. L. Veal, 1970: The dimension of ice crystals in natural clouds. *J. Atmos. Sci.*, **27**, 919–926.

Aydin, K. and C. Tang, 1993: Millimeter wave polarimetric scattering from ice crystals. In *26th International Conference on radar meteorology*, American Meteorological Society, Boston, MA, 123-125.

Barber, P. and C. Yeh, 1975: Scattering of electromagnetic waves by arbitrarily shaped dielectric bodies. *Appl. Opt.*, **14**, 2864–2872.

Bohren, C. F. and D. R. Huffman, 1983: *Absorption and Scattering of Light by Small Particles.* Wiley-Interscience, New York.

Bohren, C. F. and S. B. Singham, 1991: Backscattering by nonspherical particles: a review of methods and suggested new approaches. *J. Geophys. Res.*, **96**, 5269–5277.

Bringi, V. N. and A. Hendry, 1990: Technology of polarization diversity radars for meteorology. In *Radar in Meteorology: Battan Memorial and 40TH Anniversary radar meteorology Conference*, Atlas, D., editor. American Meteorological Society, Boston, MA.

Danielsen, E. F., 1993: In situ evidence of rapid, vertical, irreversible transport of lower tropospheric air into the lower tropical stratosphere by convective cloud turrets and by larger-scale upwelling in tropical cyclones. *J. Geophys. Res.*, **98**, 8665–8681.

DeMott, P. J., M. P. Meyers, and W. R. Cotton, 1994: Parameterization and impact of ice initiation processes relevant to numerical model simulations of cirrus clouds. *J. Atmos. Sci.*, **51**, 77–90.

Dowling, D. R. and L. F. Radke, 1990: A summary of the physical properties of cirrus clouds. *J. Appl. Meteor.*, **29**, 970–978.

Draine, B. T., 1988: The discrete-dipole approximation and its application to interstellar graphite grains. *Astrophys. J.*, **333**, 848–872.

Dungey, C. E. and C. F. Bohren, 1993: Backscattering by nonspherical hydrometeors as calculated by the coupled dipole method: an application in radar meteorology. *J. Atmos. Oceanic Technol.*, **10**, 526–532.

Dyson, F., 1993: George Green and physics. *Physics World*, **6**, 33–38.

Evans, K. F., 1993: *Microwave remote sensing algorithms for cirrus clouds and precipitation.* PhD thesis, Colorado State University, Fort Collins, CO.

Evans, K. F. and J. Vivekanandan, 1990: Multiparameter radar and microwave radiative transfer modeling of nonspherical atmospheric ice particles. *IEEE Trans. On Geosci. Rem. Sens.*, **28**, 423–437.

Flatau, P. J., G. L. Stephens, and B. T. Draine, 1990: Light scattering by rectangular solids in the discrete-dipole approximation: a new algorithm exploiting the block-toeplitz structure. *J. Opt. Soc. Am. A*, **7**, 593–600.

Flatau, P. J., G. J. Tripoli, J. Verlinde, and W. R. Cotton, 1989: The CSU-RAMS cloud microphysics module: general theory and code documentation. Technical Report 451, Colorado State University.

Fuller, K. A., 1993: Scattering and absorption by inhomogeneous spheres and sphere aggregates. In *Laser applications in combustion and combustion diagnostics: Proceedings of SPIE Conference 1862*, 249-257.

Goedecke, G. H. and S. G. O'Brien, 1988: Scattering by irregular inhomogeneous particles via the digitized green's function algorithm. *Appl. Opt.*, **27**, 2431–2438.

Heymsfield, A. J. and C. M. R. Platt, 1984: A parameterization of the particle size spectrum of ice clouds in terms of the ambient temperature and the ice water content. *J. Atmos. Sci.*, **41**, 846–855.

Holt, A. R., 1980: The Fredholm integral equation method and comparison with T-matrix approach. In *Acoustic, electromagnetic, and elastic wave scattering: focus on the T-matrix approach*, Varadan, V. K. and Varadan, V. V., editors. Permagon Press, New York, 255-268.

Holt, A. R., 1982: The scattering of electromagnetic waves by single hydrometeors. *Radio Sci.*, **17**, 929–945.

Holt, A. R., N. K. Unzungolu, and B. G. Evans, 1978: An integral equation solution to the scattering of electromagnetic radiation by dielectric spheroids and ellipsoids. *IEEE Trans. Antennas Propag.*, **AP-26(5)**, 706–712.

Kosarev, A. L. and I. P. Mazin, 1991: An empirical model of the physical structure of upper-layer clouds. *Atmos. Res.*, **26**, 213–228.

Kropfli, R. A., B. W. Bartram, and S. Y. Matrosov, 1990: The upgraded wpl dual-polarization 8-mm wavelength doppler radar for microphysical and climate research. In *Proceedings of the Conference on Cloud Physics*, American Meteorological Society, Boston, MA, 341-345.

Lhermitte, R., 1987: A 94-GHz Doppler radar for cloud observations. *J. Atmos. Oceanic Technol.*, **4**, 36–48.

Lhermitte, R., 1988: Cloud and precipitation remote sensing at 94-GHz. *IEEE Trans. On Geosci. Rem. Sens.*, **26**, 207–216.

Liao, L. and K. Sassen, 1993: Investigation of relationships between K_a-band radar reflectivity and ice and liquid water contents. *Atmos. Res.* In press.

Lindzen, R. S., 1990a: Response. *Bull. Amer. Met. Soc.*, **71**, 1465–1467.

Lindzen, R. S., 1990b: Some coolness concerning global warming. *Bull. Amer. Met. Soc.*, **71**, 288–299.

Liou, K.-N., 1986: Influence of cirrus clouds on weather and climate processes: a global perspective. *Month. Weather Rev.*, **114**, 1167–1199.

Magono, C. and C. W. Lee, 1966: Meteorological classification of natural snow crystals. *J. Fac. Sci. Hokkaido Univ., Japan*, **2**, 321–335. Series VII.

Manabe, S. and R. T. Wetherald, 1967: Thermal equilibrium of the atmosphere with a given distribution of relative humidity. *J. Atmos. Sci.*, **24**, 241–259.

Matrosov, S. Y., 1991a: Prospects for the measurement of ice cloud particle shape and orientation with elliptically polarized radar signals. *Radio Sci.*, **26**, 847–856.

Matrosov, S. Y., 1991b: Theoretical study of radar polarization parameters obtained from cirrus clouds. *J. Atmos. Sci.*, **48**, 1062–1070.

Matrosov, S. Y., 1992: Radar reflectivity in snowfall. *IEEE Trans. Geosci. Rem. Sens.*, **30**, 454–461.

Matrosov, S. Y., T. Uttal, J. B. Snider, and R. A. Kropfli, 1992: Estimation of ice cloud parameters from ground-based infrared radiometer and radar measurements. *J. Geophys. Res.*, **97**, 11567–11574.

McIntosh, R. E., A. Pazmany, S. Sekelsky, and J. Mead, 1991: Development of a cloud profiling radar system. In *Proceedings of the second atmospheric radiation measurement (ARM) science team meeting*, United States Department of Energy, 135.

Mead, J. B., R. E. McIntosh, D. Vandemark, and C. T. Swift, 1989: Remote sensing of clouds and fog with a 1.4-mm radar. *J. Atmos. Oceanic Technol.*, **6**, 1090–1097.

Meneghini, R. and T. Kozu, 1990: *Spaceborn Weather Radar.* Artech House, Boston, MA.

Mitchell, D. L., 1994: A model predicting the evolution of ice particle size spectra and radiative properties of cirrus clouds. part I: Microphysics. *To appear in J. Atmos. Sci.*

Mon, J. P., 1982: Backward and forward scattering of microwaves by ice particles: a review. *Radio Sci.*, **17**, 953–971.

Morrison, J. A. and M. J. Cross, 1979: Scattering of a plane electromagnetic wave by axisymmetric raindrops. *Bell System Tech. J.*, **53**, 955–1019.

O'Brien, S. G. and G. H. Goedecke, 1988: Scattering of millimeter waves by snow crystals and equivalent homogeneous symmetric particles. *Appl. Opt.*, **27**, 2439–2444.

Oguchi, T., 1973: Attenuation and phase rotation of radio waves due to rain: calculations at 19.3 and 34.8 ghz. *Radio Sci.*, **8**, 31–38.

Oguchi, T., 1975: Rain depolarization studies at centimeter and millimeter wavelengths: theory and measurement. *J. Radio Res. Lab.*, **22**, 165–211.

Oguchi, T. and Y. Hosoya, 1974: Scattering properties of oblate raindrops and cross polarization of radio waves due to and phase rotation of radio waves due to rain part II: calculations at microwave and millimeter wave regions. *J. Radio Res. Lab.*, **21**, 191–259.

Organization, W. M., 1969: International cloud atlas. Technical report, World Meteorological Organization.

Paul W. Stackhouse, J., 1989: A theoretical and observational comparison of cirrus cloud radiative properties. Master's thesis, Colorado State University, Fort Collins, CO.

Pazmany, A., J. B. Mead, R. E. McIntosh, M. Hervig, R. Kelly, and G. Vali, 1993: 95 ghz polarimetric radar measurements of orographic cap clouds from the Elk Mountain Wyoming Observatory. *Submitted to J. Atmos. Oceanic Technol.*

Peters, R. M., B. A. Albrecht, M. A. Miller, and J. T. Treaster, 1992: Automated cloud profiling with a 94 GHz radar. In *Proceedings of the 11th International Conference on Clouds and Precipitation*, American Meteorological Society, Boston, MA, 1033-1036.

Pruppacher, H. R. and J. D. Klett, 1978: *Microphysics of Clouds and Precipitation.* Reidel Publishing Co., Dordrecht, Holland.

Purcell, E. M. and C. R. Pennypacker, 1973: Scattering and absorption of light by nonspherical dielectric grains. *Astrophys. J.*, **186**, 705–714.

Rayleigh, L., 1871: On the light from the sky, its polarization and color. *Philos. Mag.*, **22**, 165–211. Reprinted in *Scientific Papers by Lord Rayleigh*, Vol. I: 1869-1881, No. 8, Dover, New York, 1964.

Richardson, L. F., 1922: *Weather Prediction by Numerical Process.* Cambridge University Press, London and New York.

Sassen, K., 1980: Remote sensing of planer ice crystal fall attitudes. *J. Meteor. Soc. Japan*, **58**, 422–429.

Sassen, K., 1987: Ice cloud content from radar reflectivity. *J. Clim. Appl. Meteor.*, **26**, 1050–1053.

Seliga, T. A. and V. N. Bringi, 1976: Potential use of radar reflectivity measurements at orthogonal polarizations for measuring precipitation. *J. Appl. Meteor.*, **15**, 69–76.

Seliga, T. A. and V. N. Bringi, 1978: Differential reflectivity and differential phase shift: applications in radar meteorology. *Rad. Sci.*, **13**, 271–275.

Shepard, J. W., A. R. Holt, and B. G. Evans, 1981: The effects of shape on electromagnetic scattering by ice crystals. *IEE Conf. Pub.*, **195**, 96–100.

Stephens, G. L., 1994: *Remote Sensing of the lower atmosphere: an Introduction.* Oxford University Press, New York.

Stephens, G. L., S. K. Cox, P. Stackhouse, J. Davis, and A. Class, 1993: Fire in the classroom. *Bull. Amer. Meteor. Soc.*, **74**, 2375–2383.

Stephens, G. L. and T. J. Greenwald, 1991: The earth's radiation budget and its relation to atmospheric hydrology 1. observations of the clear sky greenhouse effect. *J. Geophys. Res.*, **96**, 15325–15340.

Sun, D.-Z. and R. S. Lindzen, 1993: On the distribution of tropical water vapor. *Submitted to J. Atmos. Sci.*

Ulaby, F. T. and C. Elachi, 1990: *Radar Polarimetry for Geoscience Applications.* Artech House, Norwood, MA.

Umashankar, K. and A. Taflove, 1982: A novel method to analyze electromagnetic scattering of complex objects. *IEEE Trans. Electromag. Compat.*, **EMC-24**, 397–405.

Van de Hulst, H. C., 1981: *Light Scattering by Small Particles.* Dover, New York.

van Zyl, J. J., 1989: Unsupervised classification of scattering behavior using radar polarimetry data. *IEEE Trans. Geosci. Rem. Sens.*, **27**, 36–45.

Vivekanandan, J. and W. M. Adams, 1993: Theoretical investigation of multiparameter radar scattering characteristics of ice crystals. In *26th International Conference on radar meteorology*, American Meteorological Society, Boston, MA, 109-111.

Vivekanandan, J., W. M. Adams, and V. N. Bringi, 1991: Rigorous approach to polarimetric radar modeling of hydrometeor orientation distributions. *J. Appl. Meteor.*, **30**, 1053–1063.

Wang, P. K., 1987: Two dimensional shape and size characterization of polygonally symmetric shapes. *J. Colloid. Interface Sci.*, **117**, 271–281.

Warren, S. G., 1984: Optical constants of ice from the ultraviolet to the microwave. *Appl. Opt.*, **23**, 1206–1225.

Waterman, P. C., 1965: Matrix formulation of electromagnetic scattering. *Proc. IEEE*, **53**, 805–812.

Waterman, P. C., 1969: Scattering by dielectric obstacles. *Alta Freq.*, **38**, 348S–352S.

Yeh, C., R. Woo, A. Ishimaru, and J. Armstrong, 1982: Scattering by ice needles and plates at 30 ghz. *Radio Sci.*, **17**, 1503–1510.

Appendix A

RADAR POLARIZATION PARAMETERS

This appendix seeks to illustrate how radar observables are related to the elements of the Mueller matrix. In doing so it will shed some light on the what the radar observables physically mean; that is how to interpret them. There are many different radar parameters which can be derived depending on the polarization basis used and the application, either bistatic or monostatic. We were not concerned with bistatic implications despite their import. As an example we note that the telecommunications industry is concerned with the effect of clouds on the propagation of microwave radiation along earth to satellite paths. In such propagation studies it is useful to compute parameters such as differential attenuation and differential phase shift from the extinction matrix. However we were interested in the use of polarization diversity radars to obtain information about cirrus clouds in the traditional monostatic fashion, and limited ourselves to parameters derived from backscattered radiation. Because the scattering models output the extinction matrix as well as the forward and backward scattering matrices, this information is available for future analysis.

The most general state of polarization basis of a radar can be described in terms of an ellipse (e.g. Bringi and Hendry, 1990). Matrosov (1991a) theoretically examines the applicability of elliptical polarization in anticipation of measurements at 35 GHz. In this work we computed parameters based on the special cases of linear and circular polarization bases. The details of how to obtain the elements of the Mueller matrix from the scattering models were given in section 2.2.2. In the following two sections we will reiterate the meaning of the scattering amplitude and Mueller matrices and then give explicit formulae for the radar observables which are used in this report.

A.1 THEORY

From a physical standpoint, the scattering amplitude matrix describes how a given particle with a specified orientation relative to an impinging electromagnetic plane wave will directionally alter the field (temporal dependence is assumed). That is, it relates the scattered electromagnetic field to the incident electromagnetic field (cf. equation 2.8)

$$\begin{bmatrix} \mathbf{E}_{v,s} \\ \mathbf{E}_{h,s} \end{bmatrix} = \frac{\exp(-ikr)}{ikr} \begin{pmatrix} \mathbf{F}_{vv} & \mathbf{F}_{vh} \\ \mathbf{F}_{hv} & \mathbf{F}_{hh} \end{pmatrix} \begin{bmatrix} \mathbf{E}_{v,i} \\ \mathbf{E}_{h,i} \end{bmatrix}. \tag{A.1}$$

The subscripts (h and v) indicate the polarization of the incident and scattered polarizations in that order. Thus $\mathbf{F}_{vh}$ relates the component of the horizontally polarized scattered field to the vertically polarized incident field.

In practice we do not usually measure the electromagnetic fields. What is measured are intensities. The preferred way in which the intensity of polarized radiation is expressed is in terms of the stokes vector (with elements I, Q, U, V) and the Mueller matrix **S**. The elements of **S** are expressed in terms of $|\mathbf{F}|^2$ according to equation 2.10.

A.2 FROM MUELLER ELEMENTS TO RADAR OBSERVABLES

Radar observables are quantities such as linear reflectivities (horizontal, Z_{hh}; vertical, Z_{vv}; differential, Z_{DR}), circular reflectivities (main channel, Z_m; orthogonal channel Z_o), and depolarization ratios (linear, LDR; and circular, CDR). These radar observables can be expressed in terms of the elements of the Mueller matrix, which have been incoherently averaged over the ensemble of ice crystals as indicated in equation 2.10. The relations for radar observables will be defined with consideration being given to the physical meaning. Please observe that the use of the word orientation should be interpreted as meaning the orientation of the particles with respect to elevation angle of the incident radiation.

We will first define the parameters which, in and of themselves, yield no information about particle shape or orientation although they are inherently sensitive to both shape and orientation. The primary and direct response of these parameters is to size and concentration of the ice crystals. In the literature the following parameters are generally called effective (or equivalent) radar reflectivity factors and are denoted by Z_e. For a linear polarization basis we have

$$Z_{hh} = c(S_{11} - S_{S12} - S_{21} + S_{22}), \tag{A.2}$$

$$Z_{vv} = c(S_{11} + S_{S12} + S_{21} + S_{22}). \tag{A.3}$$

As before, the subscripts indicate the polarization of the incident and scattered radiation which can be either horizontally (h) or vertically (v) polarized. The unpolarized, radar reflectivity factor is given by $Z_e = \frac{1}{2}(Z_{hh} + Z_{vv})$. For a circular polarization basis

$$Z_m = c(S_{11} - S_{44}), \tag{A.4}$$

$$Z_o = c(S_{11} + S_{44}). \tag{A.5}$$

Here the subscripts denote the main (m) and orthogonal (o) channels. The main channel is defined to be the channel of the transmitted wave. For reasons discussed below, it is generally true that $Z_o \geq Z_m$. The constant c is given by

$$c = 10^9 4\pi(\lambda^4/2|K_i|^2\pi^5).$$

This constant is different than the constant which appears in the traditional definition of equivalent radar reflectivity by the factor 4π, and was expressed in this unreduced form to emphasize this. The $4\pi/2$ is an artifact of the Mueller matrix representation of particle scattering. The factor 10^9 converts to units of mm^6/m^3 assuming that all units have been given in mm (particle size, number concentration and wavelength).

To use polarization to understand the joint effects of particle shape and orientation we must consider the relationship between the various components of each polarization basis. This is achieved by taking ratios of the various polarizations. In principle any parameter sensitive to shape will also be sensitive to orientation. In this work the crystals were assumed to be lying perfectly horizontal (i.e. the major dimension). Consequently we need not concern ourselves with orientation. This is not the case in reality and careful consideration of the effects of orientation must be given.

To understand the mechanism of depolarization for the linear polarization basis we shall enlist the aid of a Rayleigh spheroid with major and minor axes a and b, respectively. What is true for spheroids can be generalized to any arbitrary shapes. We observe that a vertically or horizontally polarized incident wave can be projected onto these axes. For a spheroid with an arbitrary orientation some of the energy of the incident wave will be projected onto an axis with a component which is orthogonal to the incident wave. This energy will then be scattered back to the source as cross-polarized radiation. Thus we say that some of the wave has been depolarized and we quantify the amount of depolarization via the linear depolarization ratio. For spheroids the vertically polarized incident wave will 'see' a different amount of the particle than will the horizontally polarized radiation. The consequence of this is that the vertical co-polarized radiation will be different than the horizontal co-polarized radiation. This difference, which depends upon the ratio of the minor to the major axis, is measured through the differential reflectivity. For a sphere under any condition or plate at broadside incidence we would expect the cross terms to be zero (i.e. hv and vh) and the perpendicular terms to be equal (i.e. hh and vv). Under other circumstances these terms will deviate yielding interesting values of ZDR and LDR. For linear polarization

$$Z_{DR} = (S_{11} - S_{S12} - S_{21} + S_{22})/(S_{11} + S_{S12} + S_{21} + S_{22}), \tag{A.6}$$

$$LDR = (S_{11} - S_{S12} + S_{21} - S_{22})/(S_{11} - S_{S12} - S_{21} + S_{22}). \tag{A.7}$$

An alternative definition of the linear depolarization ratio has been proposed by Bob Kelly (personal communication, 1993):

$$LDR' = \frac{((S_{11} + S_{S12} - S_{21} - S_{22}) + (S_{11} - S_{S12} + S_{21} - S_{22}))}{((S_{11} - S_{S12} - S_{21} + S_{22}) + (S_{11} + S_{S12} + S_{21} + S_{22}))} \tag{A.8}$$

It is hoped that this parameter will be more sensitive particle shape than the more traditional definition given above. The prime is used to delineate these two definitions.

We now turn to circular depolarization. For a perfect sphere, we expect $Z_m = 0$ and all of the returned signal to be in Z_o which can be understood as follows (for the sake of argument we have assumed left hand circular (LHC) polarization as opposed to right hand circular (RHC), without any loss of generality): A particle excited by a LHC polarized wave will scatter radiation with the same polarization. The source of the wave can now be considered to be the particle, however, and a wave propagating back to the source of the original wave will appear to have RHC polarization from the point of view of an observer at that location. For aspherical particles this is no longer true, some of the energy is returned as RHC and some as LHC; consequently $Z_m > 0$. Thus for the circular circular polarization basis:

$$CDR = (S_{11} + S_{44})/(S_{11} - S_{44}) \tag{A.9}$$

Units for the shape dependent parameters are expressed as dB.